

**THEORETICAL AND EXPERIMENTAL INVESTIGATION
OF INTELLIGENT NON-LINEAR CONTROLS FOR
MAGNETORHEOLOGICAL ELASTOMER BASED
VIBRATION SYSTEMS**

Thesis

Submitted in partial fulfilment of the requirements for the Degree of

DOCTOR OF PHILOSOPHY

by

SUSHEEL KUMAR



**DEPARTMENT OF MECHANICAL ENGINEERING
NATIONAL INSTITUTE OF TECHNOLOGY KARNATAKA
SURATHKAL, MANGALORE – 575025**

JULY, 2021

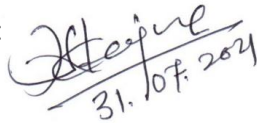
DECLARATION

I hereby declare that the Research synopsis entitled “**THEORETICAL AND EXPERIMENTAL INVESTIGATION OF INTELLIGENT NON-LINEAR CONTROLS FOR MAGNETORHEOLOGICAL ELASTOMER BASED VIBRATION SYSTEMS**” which is being submitted to the **National Institute of Technology Karnataka, Surathkal** in partial fulfillment of the requirements for the award of the Degree of **Doctor of Philosophy in Mechanical Engineering** is a *bonafide report of the research work carried out by me*. The material contained in this Research synopsis has not been submitted to any other Universities or Institutes for the award of any degree.

Register Number: **145057ME14F15**

Name of the Research Scholar: **SUSHEEL KUMAR**

Signature of the Research Scholar:



31.07.2021

Department of Mechanical Engineering

Place: NITK, Surathkal

Date: 31-07-2021

CERTIFICATE

This is to certify that the Research synopsis entitled “**THEORETICAL AND EXPERIMENTAL INVESTIGATION OF INTELLIGENT NON-LINEAR CONTROLS FOR MAGNETORHEOLOGICAL ELASTOMER BASED VIBRATION SYSTEMS**” submitted by **Mr. SUSHEEL KUMAR (Register Number: 145057ME14F15)** as the record of the research work carried out by him, *is accepted as the Research synopsis submission* in partial fulfilment of the requirements for the award of the Degree of **Doctor of Philosophy**.

Research Guides

Prof. S M MURIGENDRAPPA
Professor

Prof. K V GANGADHARAN
Professor

Department of Mechanical Engineering
NITK, Surathkal

Chairman-DRPC

Date:

Dedicated to

my grandparents

Smt. Muktabai and Late Sri. Bheemrao Gajare

and

parents Smt. Panchsheela and Sri. Naganathrao Gajare

Acknowledgements

It gives me immense happiness to express my heartfelt gratitude to my research supervisors **Prof. S M Murigendrappa** and **Prof. K. V. Gangadharan**, Department of Mechanical Engineering, National Institute of Technology Karnataka, Surathkal, Mangalore, for their valuable guidance and encouragement throughout my research work. Working under them has taught me how to do good research, be kindful and be humble toward others. Without their suggestions, support and freedom, the proposed goal would not have been achieved.

I sincerely thank the RPAC members, **Dr. Srikanth Bontha**, Department of Mechanical Engineering and **Prof. Harsha Vardhan**, Department of Mining Engineering, for providing valuable suggestions and support extended to me on all occasions.

I would like to express my gratitude to **Prof. S M Kulkarni**, Head, Dept. of Mechanical Engineering, as well as the **previous Heads** of the dept. for providing me the required facilities

I would like to thank my friend and batchmate, **Dr. Praveen Shenoy K**, for his valuable time for technical discussions, encouragement and confidence and proofreading of my journals and thesis. I would like to thank my friends seniors **Dr. M P Arun**, **Dr. Mallikarjun Balichakra**, **Dr. G Bal Narsimha**, **Mr. Ravikumar**, **Dr. Umanath Poojary**, **Dr. Arun Parameswara**, **Dr. Vijay M** and **Dr. Harsha Hegde** for their timely technical inputs. I wish to thank all the **Centre for System Design (CSD) members** for their constant help and encouragement during research work. I also want to thank my friends, **Mr. Rohit Rajpal**, **Mr. Kiran Katari**, **M. Kiran Anginthaya**, **Mr. Anarghya Murthy** from the Department of Mechanical Engineering.

I would like to thank family members, brothers **Sariputra**, **Avinash** and **Balbheem** and sister-in-law **Sonali** and nephew **Samyak**. I would like to thank my wife **Visakha** and son **Ariyo** for their presence during the downhearted time in research.

(SUSHEEL KUMAR)

Abstract

Magnetorheological elastomer (MRE) based semi-active isolators and absorbers are prominently used to reduce undesirable vibration for a wide range of operating frequencies. The real-time implementation of these systems requires the controllers to vary the electric current of the electromagnet. Previous researchers have focused on the model-based and fuzzy controllers to control input current. However, due to the viscoelastic behavior of MRE, it exhibits nonlinearities and time-varying properties. This behavior makes the real-time implementation of the MRE-based vibration isolator and absorber less effective with existing controllers. The present work concentrates on the theoretical and experimental investigation of the intelligent adaptive nonlinear controls on the MRE-based vibration isolation and adaptive tuned vibration absorber (ATVA).

For the implementation of the controllers, a thorough knowledge of the field-dependent properties of MRE is studied using an in-house custom-made dynamic characterization setup. The dynamic characterization of the MRE is carried out for variable input frequency, displacement and magnetic field. Further, the Bouc-Wen model is employed to comprehend constitutive the relationship between the individual parameters. The characterized MRE is used in the MRE vibration isolator. The properties of the MRE vibration isolator are extracted from shift frequency data. Furthermore, the performance of the MRE vibration isolation is investigated for the model-based PID and LQR controllers.

MRE exhibits nonlinearity and time-varying properties that limit the application of linear controllers. To overcome the limitations of the linear controllers, the nonlinear and intelligent controls based on neural networks and fuzzy systems are designed. The designed boundary sliding mode control (BSMC) and neural network-based adaptive observer neural network fuzzy sliding mode control (NNAONFSMC) are implemented on the MRE vibration isolation system. The Lyapunov theorem assesses the asymptotical stability of the designed observer and controls. The controllers' effect is compared without and with parameter uncertainties of MRE vibration isolation at the single frequency excitation. Further, The NNAONFSMC has been analyzed for variable excitation frequency, and the maximum percentage reduction of the measured

acceleration is 34%. From these outcomes, it is evident that the NNAONFSMC is more effective with time-varying parameter uncertainties of MRE than the BSMC at single and variable frequency excitation.

Furthermore, the performance of model-free adaptive fuzzy sliding mode control for the magnetorheological elastomer-based adaptive tuned vibration absorber (MRE ATVA) has been investigated. MRE ATVA is fabricated with anisotropic MRE. Sliding mode and adaptive fuzzy sliding mode controls have been developed. The boundary layer is applied to the sliding surface to reduce the chattering effect in the sliding mode control. In the adaptive fuzzy sliding mode control, two fuzzy systems approximate the equivalent control and switching control. The Lyapunov theorem evaluates the asymptotical stability of the developed adaptive control based on fuzzy systems. The performance is compared for both the controls subjected to single-frequency excitation. Further, the adaptive fuzzy sliding mode control has been investigated for variable frequency excitation. The maximum reduction of transmissibility of primary mass is 38.14%. Based on the results, the model-free adaptive fuzzy sliding mode control is more effective in tuning the natural frequency of MRE ATVA by 0.5 s with parameter uncertainties and under variable frequency excitation compared to the boundary layer sliding mode control.

Keywords: *Magnetorheological elastomer, Vibration isolation, Vibration absorber, sliding mode control, Model-free, Neural network, Fuzzy system, Adaptive control*

Table of Contents

1. Introduction	1
1.1 Introduction to Vibration Control	1
1.2 Magnetorheological Materials.....	2
1.3 Magnetorheological Elastomer	2
1.1 Applications of Magnetorheological Elastomer.....	4
1.2 Outline of the Thesis	5
2. Literature Survey	6
2.1 Introduction	6
2.2 Dynamic Characterization and Modeling of the Magnetorheological Elastomer.....	6
2.3 Magnetorheological Elastomer Vibration Isolation with Controller Strategies	9
2.4 Magnetorheological Elastomer Vibration Absorber with Controller Strategies	11
2.5 Closure	13
2.6 Motivation	13
2.7 Research Objectives	13
3. Dynamic Characterization and Modelling of Magnetorheological Elastomer 	15
3.1 Introduction	15
3.2 Preparation of Magnetorheological Elastomer.....	15
3.3 Experimental Setup of Dynamic Characterization of the MRE.....	17
3.4 Stiffness and Damping of MRE	19
3.4.1 Dynamic Characterization under Variable Current	19
3.4.2 Dynamic Characterization under Variable Displacement.....	22

3.4.3	Dynamic Characterization under Variable Frequency.....	26
3.5	Modeling of MRE	29
3.5.1	Bouc-Wen Model.....	29
3.5.2	Field-Dependent Parameters of the Bouc-Wen Model.....	31
3.6	Closure	34
4.	Performance of Model-based Linear Controllers on Magnetorheological Elastomer Vibration Isolation	35
4.1	Introduction	35
4.2	Vibration Isolation.....	35
4.3	Magnetorheological Elastomer Vibration Isolation	38
4.3.1	Fabrication of MRE Vibration Isolator.....	38
4.3.2	The Frequency Shift of MRE Vibration Isolator	38
4.4	System Dynamics of MRE Vibration Isolation.....	40
4.4.1	Vibration Isolation with Control Input	40
4.4.2	State-Space Equation of MRE Vibration Isolation	41
4.5	Linear Controllers	42
4.5.1	Proportional Integral Derivative Controller.....	42
4.5.2	Linear Quadratic Regulator Controller	43
4.5.3	Model-based PID and LQR Controllers	44
4.6	Simulation Analysis	45
4.7	Results and Discussion.....	46
4.7.1	Single-Frequency Excitation with Model-based PID Controller.....	46
4.7.2	Single-Frequency Excitation with Model-based LQR Controller	49
4.8	Experimental Setup for the Real-Time Controller of MRE Vibration Isolation.....	52
4.9	Results and Discussion.....	53

4.9.1	The Experiment of Single-Frequency Excitation with PID Controller	.53
4.9.2	The Experiment of Single-Frequency Excitation with LQR Controller	58
4.10	Closure	62
5.	Intelligent Non-Linear Controls for the Magnetorheological Elastomer	
Vibration Isolation		63
5.1	Introduction	63
5.2	Nonlinear Systems and Controls	63
5.3	Fuzzy Systems	64
5.3.1	Basic Concept	64
5.3.2	Fuzzy System and their Properties	68
5.3.3	Adaptive Fuzzy System (AFS)	69
5.4	Neural Network	70
5.4.1	Radial Basic Function Neural Network	72
5.5	Design of Nonlinear Robust and Intelligent Adaptive Control Strategies	73
5.5.1	Sliding Mode Control (SMC)	73
5.5.2	Adaptive Observer-based Intelligent Nonlinear Control	76
5.6	Simulation Analysis of Proposed Controllers	85
5.6.1	Results and Discussion	88
5.7	Experimental Analysis	92
5.7.1	Results and Analysis	95
5.8	Closure	99
6.	Model-Free Adaptive Fuzzy Sliding Mode Control for Magnetorheological Elastomer-based Adaptive Tuned Vibration Absorber	101
6.1	Introduction	101
6.2	Dynamic Vibration Absorber (DVA)	101
6.2.1	Transmissibility Dynamic Vibration Absorber	102

6.3	Magnetorheological Elastomer-based Adaptive Tuned Vibration Absorber (MRE ATVA)	104
6.3.1	Preparation of Magnetorheological Elastomer	104
6.3.2	Fabrication of MRE ATVA	104
6.3.3	Frequency Shift of MRE ATVA.....	105
6.4	System Dynamics of MRE ATVA.....	108
6.4.1	MRE ATVA as Two Degrees of Freedom System.....	108
6.4.2	State-Space Equation of MRE ATVA	109
6.5	Design of Controllers	109
6.5.1	Boundary Layer Sliding Mode Control.	109
6.5.2	Fuzzy Logic System.....	111
6.6	Simulation Analysis	115
6.6.1	Position Tracking of MRE ATVA	116
6.6.2	Simulation of Single Frequency Excitation	118
6.6.3	Simulation of Variable Frequency Excitation.....	121
6.7	Experimental Analysis	122
6.7.1	Experiment of Single Frequency Excitation	123
6.7.2	Experiment of Variable Frequency Excitation	129
6.8	Closure	130
7.	Summary, Conclusions and Scopes of Future Work.....	131
7.1	Summary	131
7.2	Conclusions	132
7.3	Scopes of Future Work.....	133
	References.....	134

List of Figures

Figure 1.1 Vibration control methods a) passive, b) active and c) semi-active (Parameswaran et al. 2015).....	2
Figure 1.2 Magnetorheological Elastomer a) without Magnetic field and b) after the magnetic field's influence.	3
Figure 1.3 Schematic of the magnetorheological elastomer seat isolator (Du et al. 2011).	4
Figure 1.4 Controllable valve using soft MR elastomers as actuators (Böse et al. 2012).	4
Figure 3.1 Preparation of isotropic and anisotropic MRE (Visakh et al., 2013).	16
Figure 3.2 SEM image of MRE a) isotropic and b) anisotropic.	16
Figure 3.3 Schematic of the experimental setup of dynamic characterization of MRE.	17
Figure 3.4 Photograph of the experimental setup of dynamic characterization of MRE. (a) Electrodynamic shaker, (b) Accelerometer, (c) Electromagnet, (d) Force transducer, (e) MRE, (f) NI-9234, (g) Function generator, (h) DC power supply, (i) Power amplifier and (j) LabVIEW.	18
Figure 3.5 Close view of the MRE assembly.	18
Figure 3.6 Hysteresis loops of the MRE for variable current at a constant frequency of 15Hz and displacement of a) 0.2mm, b) 0.3mm, c) 0.5mm, and d) 0.6mm.	20
Figure 3.7 Hysteresis loops of the MRE for variable current at a constant frequency of 30Hz and displacement of a) 0.2mm, b) 0.3mm, c) 0.5mm, and d) 0.6mm.	21
Figure 3.9 Hysteresis loops of the MRE for variable current at a constant frequency of 60Hz and displacement of a) 0.2mm, b) 0.3mm, c) 0.5mm, and d) 0.6mm.	22
Figure 3.10 Hysteresis loops of the MRE for variable displacement at a constant frequency of 15Hz and current of a) 0A, b) 1A, c) 2A, and d) 3A.	23
Figure 3.11 Hysteresis loops of the MRE for variable displacement at a constant frequency of 30Hz and current of a) 0A, b) 1A, c) 2A, and d) 3A.	24
Figure 3.12 Hysteresis loops of the MRE for variable displacement at a constant frequency of 45Hz and current of a) 0A, b) 1A, c) 2A, and d) 3A.	25
Figure 3.13 Hysteresis loops of the MRE for variable displacement at a constant frequency of 60Hz and current of a) 0A, b) 1A, c) 2A, and d) 3A.	25

Figure 3.14 Hysteresis loops of the MRE for the variable frequency at a constant displacement of 0.2mm and current of a) 0A, b) 1A, c) 2A, and d) 3A.	26
Figure 3.15 Hysteresis loops of the MRE for the variable frequency at a constant displacement of 0.3mm and current of a) 0A, b) 1A, c) 2A, and d) 3A.	27
Figure 3.16 Hysteresis loops of the MRE for the variable frequency at a constant displacement of 0.5mm and current of a) 0A, b) 1A, c) 2A, and d) 3A.	28
Figure 3.17. Hysteresis loops of the MRE for the variable frequency at a constant displacement 0.6mm and current of a) 0A, b) 1A, c) 2A, and d) 3A.....	28
Figure 3.18 Schematic of Bouc-Wen model (Yang et al. 2013).....	29
Figure 3.19 Plots of the force response of experimental and model-predicted.	30
Figure 3.20 Experimental and predicted hysteresis loops: (a) variable frequency, (b) variable displacement and (c) variable current.	31
Figure 3.21 Plots of the Bouc-Wen model parameters; (a) A vs. I , (b) α vs. I , (c) c_0 vs. I and (d) k_0 vs. I	33
Figure 4.1 Mathematical model of vibration isolation.....	35
Figure 4.2 Plots of frequency ratio vs. transmissibility ratio.	37
Figure 4.3 MRE vibration isolator: (a) schematic and (b) photograph.....	38
Figure 4.4 Schematic of MRE vibration isolation. Figure 4.5 Plots of (a) Transmissibility vs. frequency and (b) phase angle vs. frequency.....	39
Figure 4.6 Schematic of MRE vibration isolation with control input.....	40
Figure 4.7 Schematic of PID controller.	43
Figure 4.8 Schematic of LQR controller with the observer.	44
Figure 4.9. Schematic model-based controllers with MRE vibration isolation.	45
Figure 4.10 Simulink program of model-based PID controller.	46
Figure 4.11 Simulated responses at 34Hz: (a) acceleration and (b) force.	47
Figure 4.12 Simulated responses at 36Hz: (a) acceleration and (b) force.	47
Figure 4.13 Simulated responses at 38Hz: (a) acceleration and (b) force.	48
Figure 4.14 Simulated responses at 40Hz: (a) acceleration and (b) force.	48
Figure 4.15 Simulink program of model-based LQR controller.....	49
Figure 4.16 Simulated responses at 34Hz: (a) acceleration and (b) force.	50
Figure 4.17 Simulated responses at 36 Hz: (a) acceleration and (b) force.	50
Figure 4.18 Simulated responses at 38Hz: (a) acceleration and (b) force.	51

Figure 4.19 Simulated responses at 40 Hz: (a) acceleration and (b) force.	51
Figure 4.20 Schematic of the experimental set-up of the Real-time controller.	52
Figure 4.21 Photograph of the experimental setup of the Real-time controller.....	53
Figure 4.22.LabVIEW program of PID controller.	55
Figure 4.23 Measured responses at 34Hz: (a) acceleration and (b) control current. ...	56
Figure 4.24 Measured responses at 36Hz: (a) acceleration and (b) control current. ...	56
Figure 4.25 Measured responses at 38Hz: (a) acceleration and (b) control current. ...	57
Figure 4.26 Measured responses at 40Hz: (a) acceleration and (b) control current. ...	57
Figure 4.27 LabVIEW program of LQR controller.	59
Figure 4.28 Measured responses at 34Hz: (a) acceleration and (b) control current. ...	60
Figure 4.29 Measured responses at 36Hz: (a) acceleration and (b) control current. ...	60
Figure 4.30 Measured responses at 38Hz: (a) acceleration and (b) control current. ..	61
Figure 4.31 Measured responses at 40Hz: (a) acceleration and (b) control current. ...	61
Figure 5.1 Plots of the standard membership functions.....	65
Figure 5.2 Fuzzy system.	68
Figure 5.3 Centre average method.	69
Figure 5.4 Interconnection of biological neural nets (Tayyab. 2014).....	71
Figure 5.5 Schematic of the analogy of a biological neural network (Graupe 2013)..	71
Figure 5.6 Radial basis functions neural network.....	72
Figure 5.7 Plot of radial basic function.....	73
Figure 5.8 Schematic of MRE vibration isolation.	74
Figure 5.9 Schematic of boundary layer sliding mode control.....	75
Figure 5.10 Schematic of neural network adaptive observer-based neural network fuzzy sliding mode control.....	82
Figure 5.11 Simulink program of BSMC for MRE vibration isolation.	85
Figure 5.12 Simulink program of NNAONFSMC for MRE vibration isolation.	86
Figure 5.13 Simulated time-responses of excitation frequency at 34 Hz: (a) acceleration and (b) force.....	89
Figure 5.14 Simulated time-responses of excitation frequency at 36 Hz: (a) acceleration and (b) force.....	89
Figure 5.15 Simulated time-responses of excitation frequency at 38 Hz: (a) acceleration and (b) force.....	90

Figure 5.16 Simulated time-responses of excitation frequency at 40 Hz: (a) acceleration and (b) force.....	90
Figure 5.17 Simulated responses at variable frequency excitation: (a) acceleration and (b) force.....	92
Figure 5.18 LabVIEW program of BSMC for MRE vibration isolation.....	93
Figure 5.19 LabVIEW program of NNAONFSMC for MRE vibration isolation.....	94
Figure 5.20 Measured time responses at 34 Hz: (a) acceleration and (b) control current.....	96
Figure 5.21 Measured time responses at 36 Hz: (a) acceleration and (b) control current.....	96
Figure 5.22 Measured time responses at 38 Hz: (a) acceleration and (b) control current.....	97
Figure 5.23 Measured time responses at 40 Hz: (a) acceleration and (b) control current.....	97
Figure 5.24. Measured responses under variable frequency excitation: (a) acceleration and (b) control current.....	99
Figure 6.1. Schematic of dynamic vibration absorber.....	102
Figure 6.2 Plot: Frequency ratio vs. transmissibility ratio of the primary system.....	103
Figure 6.3 MRE ATVA: (a) schematic and (b) photograph.....	105
Figure 6.4 Plots of frequency shift of MRE ATVA: (a) transmissibility vs. frequency and (b) damping factor vs. frequency.....	105
Figure 6.5 Schematic of the combined system (primary mass and MRE ATVA).....	107
Figure 6.6 Plot of transmissibility vs. frequency: (a) primary mass and (b) MRE ATVA.....	107
Figure 6.7 Schematic of MRE ATVA with control input.....	108
Figure 6.8 Schematic of boundary layer sliding mode control.....	110
Figure 6.9 Schematic of adaptive fuzzy sliding mode control.....	113
Figure 6.10 Simulink program of BSMC for MRE ATVA.....	115
Figure 6.11 Simulink program of AFSC for MRE ATVA.....	115
Figure 6.12 Time response of boundary sliding mode control: (a) position tracking without disturbance and (b) position tracking with disturbance.....	116

Figure 6.13 Time response of boundary sliding mode control: (a) force and (b) tracking error.	117
Figure 6.14 Time response of (a) position tracking of adaptive fuzzy sliding mode control with disturbance, (b) force with disturbance and (c) tracking error with disturbance.	117
Figure 6.15 Simulated responses at 50 Hz: (a) acceleration of primary mass and (b) force.	119
Figure 6.16 Simulated responses at 52 Hz: (a) acceleration of primary mass and (b) force.	119
Figure 6.17 Simulated responses at 54 Hz: (a) acceleration of primary mass and (b) force.	120
Figure 6.18 Simulated responses at 56 Hz: (a) acceleration of primary mass and (b) force.	120
Figure 6.19 Simulated responses at variable frequency excitation: (a) acceleration of primary mass and (b) force.	122
Figure 6.20 Schematic of setup of Real-time controller.	123
Figure 6.21 Photograph of the experimental setup of Real-time controller.	123
Figure 6.22 LabVIEW program of BSMC for MRE ATVA.	125
Figure 6.23 LabVIEW program of AFSMC for MRE ATVA.	126
Figure 6.24 Measured responses at 52 Hz: (a) acceleration of primary mass and (b) control voltage.	127
Figure 6.25 Measured responses at 54 Hz: (a) acceleration of primary mass and (b) control voltage.	127
Figure 6.26 Measured responses at 56 Hz frequency: (a) acceleration of primary mass and (b) control voltage.	128
Figure 6.27 Measured responses under variable frequency excitation: (a) acceleration of primary mass, (b) control voltage and (c) FFT.	130

List of Tables

Table 3.1 Optimal parameters under variable current.	32
Table 3.2 Optimal field-dependent parameters.....	34
Table 4.1 Measured dynamic properties of the MRE vibration isolator under the variable current	40
Table 4.2 Simulated results of MRE vibration isolation with model-based PID controller.....	49
Table 4.3 Results of MRE vibration isolation with model-based LQR controller under different excitation frequencies.....	52
Table 4.4 Experimental results of MRE vibration isolation with PID control.	58
Table 4.5 Results of MRE vibration isolation under different excitation frequencies.	62
Table 5.1 Optimal gains of boundary sliding mode control (BSMC).....	86
Table 5.2 Parameters of RBF and Gaussian membership function of the neural network and fuzzy system.....	87
Table 5.3 The adaptive gain and weight of the NNAO and NNAONFSMC.	87
Table 5.4 Simulated results of MRE vibration isolation under different excitation frequencies without parameter uncertainties.	91
Table 5.5 Simulated results of MRE vibration isolation under different excitation frequencies with parameter uncertainties.....	91
Table 5.6 Experimental results of MRE vibration isolation under different frequencies without parameter uncertainties.....	98
Table 5.7 Experimental results of MRE vibration isolation under different frequencies with parameter uncertainties.	98
Table 6.1 Dynamic properties of MRE ATVA for variable magnetic field.	106
Table 6.2 Simulation results of the acceleration of primary mass under different frequencies and controls.	121
Table 6.3 Simulation results of transmissibility of primary mass under variable frequency excitation with AFSC.....	122
Table 6.4 The experimental result of the acceleration of primary mass under different frequencies and controls.	128

Table 6.5. Experimental results of transmissibility of primary mass under variable frequency excitation with AFSC.....	129
--	-----

Acronyms and Abbreviations

MRE : Magnetorheological Elastomer

MRF : Magnetorheological Fluid

CIP : Carbonyl Iron Particles

AWG : American Wire Gauge

RTV : Room Temperature Vulcanized

SEM : Scanning Electron Microscope

SDoF : Single Degree of Freedom

DC : Direct Current

DVA : Dynamic Vibration Analyser

T.R : Transmissibility Ratio

ATVA : Adaptive Tuneable Vibration Absorber

PID : Proportional Integral Derivative

LQR : Linear Quadratic Regulator

SMC : Sliding mode control

BSMC : Boundary sliding mode control

MIMO : Multi-Input and Multi-Output

NN : Neural Network

RBNN : Radial Basis Function Neural Network

NNAO : Neural network-based adaptive observer

FLS : Fuzzy logic System

MF : Membership function

AFS : Adaptive Fuzzy System

AFSC : Adaptive fuzzy sliding mode control

NNAONFSMC: Neural network-based adaptive observer neural network fuzzy

sliding mode control

List of Nomenclatures

Symbol	Explanations
F	The mathematical force of the Bouc-Wen model
k_o	Stiffness co-efficient of Bouc-Wen model
c_o	Damping coefficient of Bouc-Wen model
α	Stiffness ratio of post-to- pre yielding
z	Evolutionary variable
I	Input current
m	Mass of the payload
k	Stiffness of the isolator
c	Damping coefficient of the isolator
m_b	Mass of the base
k_b	Stiffness of the base
x	Displacement of the mass
x_b	Displacement of the base
ω_n	Natural frequency
ξ	Damping ratio
r	Frequency ratio
f_0	Input force to the vibration isolation
$u(t)$	Control input
e	Signal error
x_d	Desired displacement
K_p	The proportional gain of PID controller
K_I	Integral gain PID controller
K_D	Derivative gains PID controller
K	Feedback gain-matrix of LQR controller
L	Gain matrix of the linear observer
v	Voltage input
v_{max}	Maximum voltage

H	Heaviside function
F_D	Desired optimal control force
λ	Positive constant
η	Positive constant
Φ	The thickness of the boundary layer
κ_0	Positive constant
$\mu_A(x)$	Membership function.
W	Weight matrix
ϵ	Approximation error
$\sigma(x)$	RBF activation functions
c_i	Center of the i^{th} neuron.
b_i	Width of the i^{th} neuron.
W^*	Optimal weight matrix Neural network
m_a	Mass of the MRE ATVA
k_a	Stiffness of the MRE ATVA
c_a	Damping coefficient of the MRE ATVA
m_p	Mass of the Primary system
k_p	Stiffness of the Primary system
c_p	Damping coefficient of the Primary system
x_a	Displacement of the MRE ATVA
x_p	Displacement of the Primary system
φ^*	Optimal output membership function vector of Fuzzy system
V	Lyapunov stability function
V_C	Control stability function
V_O	Observer stability function
β	Adaptive gains of neural-network
γ	Adaptive gains fuzzy logic

1. Introduction

1.1 Introduction to Vibration Control

Unwanted vibration leads the machine components, civil structures and aerospace vehicles to failure (Deng and Gong 2007), emphasizing the importance of mitigating the vibration. Of the available methods, Vibration isolators and absorbers are the effective forms of vibration control. These systems are further classified as passive, active vibration and semi-active systems (Liao et al. 2011), as shown in Figure 1.1 (Parameswaran et al. 2015). They are used in a wide range of civil structures, automobile, aerospace structures and industries. The passive system consists of a mass, a spring and a damper. This system makes it more stable to mitigate unwanted vibration. However, the passive system is only effective over a very narrow frequency range, and as the excitation frequency changes, the vibration reduction effect decreases or even collapses because of mistuning (Xu et al. 2010). In an active vibration system, attenuation of vibration is carried out by applying active force with an active element attached. Actuators for active vibration include piezoelectric actuators, electric motors and voice coil motors (Liao et al. 2011). However, several disadvantages are associated with the active vibration system, of which high energy consumption and a large activation force are predominant. To compensate for these attributes of the passive systems, the semi-active systems are used. The semi-active vibration system changes its material properties and can be used in real-time applications for a wide frequency range. Further, The semi-active system consumes less energy than the active vibration system due to not having an active force element (Liao et al., 2014). The semi-active system is achieved using smart materials such as shape memory alloys (SMA) (Tai and Ahn 2011), magnetorheological fluid (Khan et al. 2016)(Gu and Oyadiji 2008) and magnetorheological elastomer (Sinko et al. 2013)(Komatsuzaki et al. 2016)(Yang et al. 2014)(Lerner and Cunefare 2008).

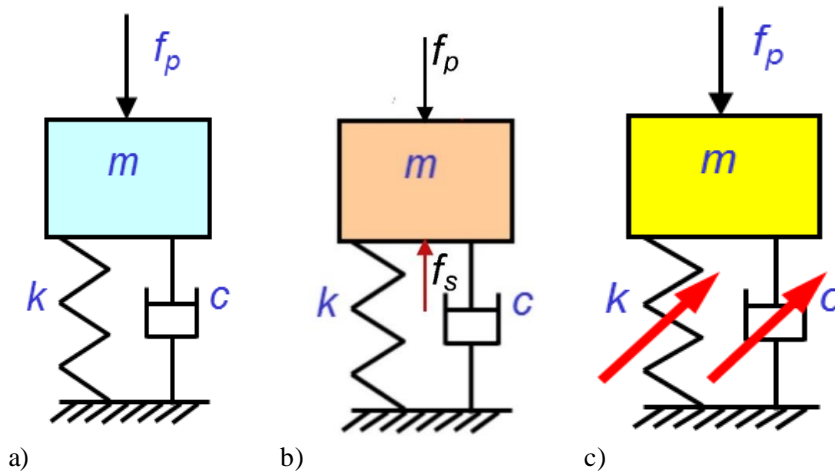


Figure 1.1 Vibration control methods a) passive, b) active and c) semi-active (Parameswaran et al. 2015).

1.2 Magnetorheological Materials

Magnetorheological materials are smart materials that exhibit field-dependent properties. The properties of MR materials change as the magnetic field varies, which is called the MR effect, discovered in 1948 by Rabinow (Li et al. 2014a). MR materials have been classified as MR fluids, MR foams and MR elastomers. The MR materials consist of the abase matrix in which magnetically polarizable filler particles are imbedded or suspended depending upon the matrix. Among the available MR materials, MR fluids (MRFs) have been used in many applications, such as the automotive industry and earth quake-resistance structures for vibration control. It has magnetically polarizable particles suspended in viscous fluids. However, they have some disadvantages, such as environmental contamination, deposition and sealing problems and (Deng and Gong 2008), limiting the application of MRF. The solid analogy of MRF is known as MRE, which avoids the disadvantages associated with MRF (Dong et al. 2009).

1.3 Magnetorheological Elastomer

Magnetorheological elastomer (MRE) is a composite material composed of magnetically polarizable particles (Lokander and Stenberg 2003) dispersed in a polymer matrix material. It changes its dynamic properties by the influence of the magnetic field. The commonly used matrix is silicone or natural rubber. The filler

materials are usually ferromagnetic particles, such as iron. In the presence of a magnetic field, the carbonyl iron particles align themselves in the direction of the applied field. This results in the formation of magnetic dipoles between adjacent carbonyl iron particles, which induces compressive forces on the interlaying matrix, increasing the stiffness of MRE (Poojary and Gangadharan 2017) (Shenoy et al. 2020) as shown in Figure 1.2. Based on how particles are spread, the MRE is categorized as anisotropic elastomers. In the anisotropic MR Elastomer, the particles are strictly orientated in the direction of the magnetic field, whereas in the isotropic elastomers, the particles are randomly distributed (Kaleta et al., 2011). Due to its ability to change the stiffness and faster response time, The MRE is used to design smart vibration isolators and absorbers (Li et al. 2014b).

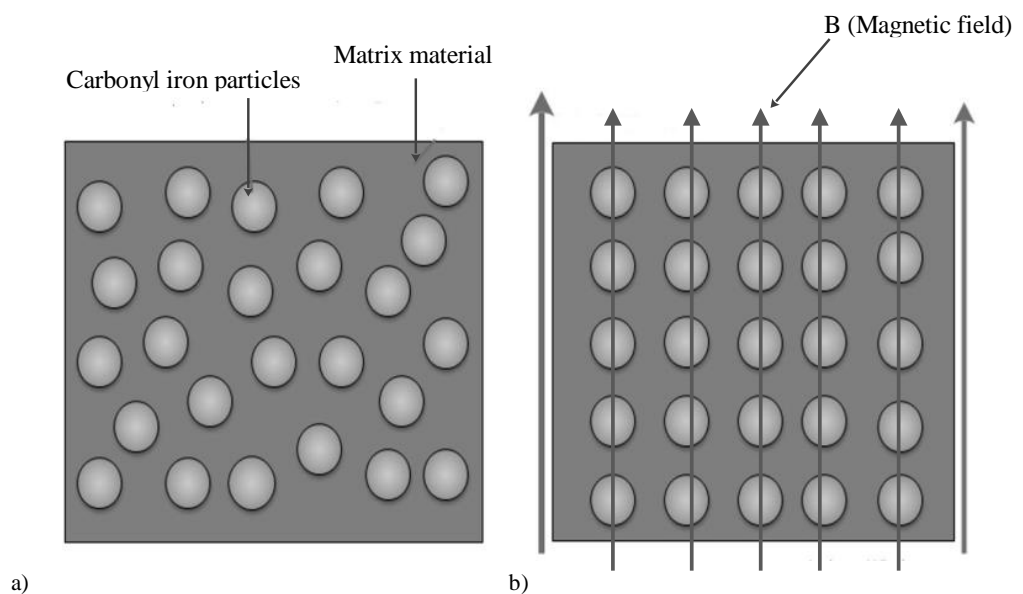


Figure 1.2 Magnetorheological Elastomer a) without Magnetic field and b) after the magnetic field's influence.

MRE behaves nonlinearly with operating parameters and exhibits parameter uncertainties over a period of time. This behavior of MRE restricts its application in a real-time application using linear controllers for MRE vibration isolator and absorber (Choi et al. 2016). This research work focused on the analysis of different controller strategies for MRE vibration isolator and absorber.

1.1 Applications of Magnetorheological Elastomer

The Field-dependent properties of MRE make it a very effective material in vibration control and actuation of control valves and the applications of MRE are demonstrated in Figures 1.3 and 1.4. Figure 1.3 depicts the MRE vibration isolator used for vibration control of the vehicle seat developed by (Du et al. 2011). Figure 1.4 illustrates the controllable valve based on MRE used in air flow control (Böse et al., 2012).

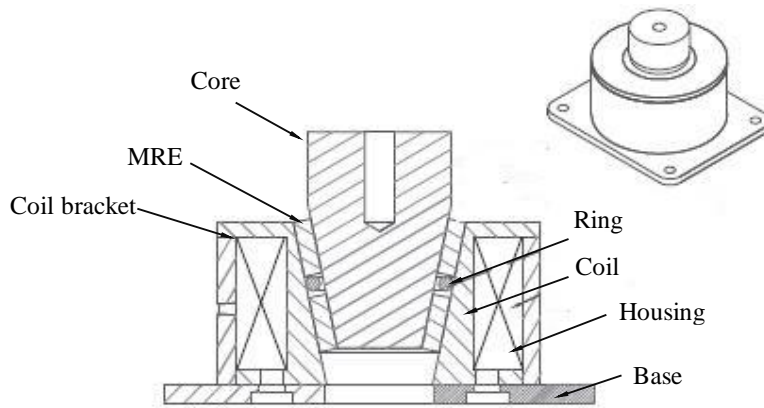


Figure 1.3 Schematic of the magnetorheological elastomer seat isolator (Du et al. 2011).

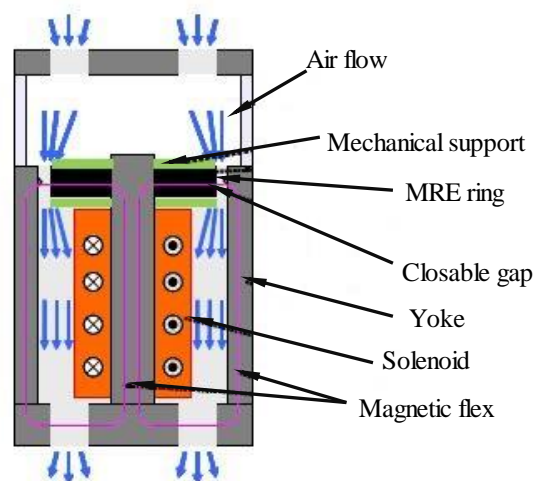


Figure 1.4 Controllable valve using soft MR elastomers as actuators (Böse et al. 2012).

1.2 Outline of the Thesis

The thesis contains six chapters. Introduction on the vibration control methods and the semi-active systems with Magnetorheological Elastomer (MRE) has been discussed in Chapter 1.

A comprehensive literature on dynamic characterization and modeling of MRE has been reviewed in Chapter 2. Further, the performance of different control strategies on the MRE vibration isolator and absorber are also discussed. It also lays down the foundation for the research gap present in the MRE vibration isolator and absorber with the different control strategies.

Chapter 3 presents the dynamic characterization of MRE under variable magnetic fields, displacements and frequencies. Further, Bouc-Wen modeling is carried out for the characterized MRE for the model-based controllers.

Performance of the MRE vibration isolation with model-based PID and LQR controllers has been presented in Chapter 4.

Chapter 5 deals with the design and analysis of intelligent (neural network and fuzzy system) control based on the neural network adaptive observer for MRE vibration isolation.

Investigation on the performance of MRE Adaptive Tunable Vibration Absorber (ATVA) using model-free adaptive fuzzy sliding mode control has been reported in Chapter 6.

Chapter 7 reports the summary, conclusions and future works of MRE-based vibration systems.

2. Literature Survey

2.1 Introduction

This chapter is concerned with a literature review on the dynamic characterization, modeling of Magnetorheological elastomer (MRE), and controller strategies for MRE vibration isolators and absorbers. The real-time application of MRE smart systems (vibration isolators and absorbers) in the field vibration control depends on the dynamic properties of MRE and controller strategies. The dynamic properties of MRE define the range of operating frequency and displacement. Further, control strategies dictate the performance of the semi-active system under the nonlinearity and time-varying properties of MRE. It is a composite material of rubber and iron particles, and the field-induced properties of MRE vary as it is prepared. The dynamic properties depend on the type of rubber, size of iron particles, isotropic or anisotropic MRE and operating loads. The MRE viscoelastic material poses nonlinearity and time-varying properties. The controller strategies can be developed to handle the nonlinearity and uncertainties of the MRE smart system. Further, based on the literature, identification of the research problem and objectives of research work are presented.

2.2 Dynamic Characterization and Modeling of the Magnetorheological Elastomer

The dynamic properties of MRE depend on combinations of the preparation and the operating parameters: frequency, amplitudes and magnetic field. Lokander and Stenberg (2003) reported that an increase in the range of the shear modulus of MRE with large irregular iron particles. Further, they observed that the matrix material did not influence the shear modulus. However, the increase in the modulus can be achieved by plasticizer and has to be used in low amplitude applications, and increase in damping due to change in magnetic fields is very small any practical use. Shen et al. (2004) developed the novel approach to the fabrication of polyurethane and natural rubber MREs. They reported that the modulus of polyurethane MR elastomers increases by 28% under the influence of magnetic field. Blom and Kari (2005) studied the dynamic behavior of magneto-sensitive (MS) rubbers in the audible frequency range. Fletcher–

Gent effect model is used to understand the shear modulus of MS rubbers. Silicone and natural rubbers are used with a volume of 33% iron particles.

The result shows that both kinds of rubber are strongly dependent on the amplitude and display a broad range of shear modulus. The effects of the content of iron particle, magnetic field and temperature were studied on the storage modulus and loss factor of MRE in shear mode by Chen et al. (2007). It is reported that the storage modulus and loss factor increase with an increase in the magnetic field. The dynamic characterization of MRE under compression-shear type combined loading is performed by Jung et al. (2009). MRE samples were fabricated with 30% content iron particle by volume and reported that MRE effect increase as magnetic field increase. Further, the elastic modulus of the pre-compressed MREs increase as compared with that of MRE without pre-compression. The mechanical properties of isotropic and anisotropic MRE are investigated by Kaleta et al. (2011) and reported that the variation in magneto-mechanical properties is articulated by changing the slope of the hysteresis loop.

Boczkowska et al.(2012) prepared a RTV anisotropic soft polyurethane MRE with 11.5% carbonyl iron by volume. The particle chains were inclined at an angle 0, 30, 45 and 90 degrees to the direction magnetic field and the size of carbonyl iron particles are 1-2 μm , 6-9 μm and 70 μm . It is reported from the results that the effect of the MRE increases with an increase in magnetic field and frequency. Further, 6-9 μm particle size exhibits the maximum MRE effect at an angle of 30 degrees. Johnson et al. (2012) investigated the dynamic properties of thick MREs by varying both percentages of iron particles and thickness and reported that the thickness of MRE has a significant effect on the dynamic properties of MRE with zero magnetic fields. In the influence of the magnetic field, the thickness doesn't show any effect on storage modulus. The magnetic-field-induced normal force of anisotropic and isotropic MRE is examined by Liao et al. (2012a) under compression mode. The magnetic-field-induced normal force is higher in anisotropic MRE than in isotropic MRE. The increase in temperature leads to variation in magnetic-field-induced normal force.

The dynamic properties of the anisotropic and isotropic MRE are performed by Li and Sun (2013) under compressive and shear loading. The properties of the MREs depend on the strain amplitude and magnetic field. Further, the anisotropic MRE exhibits a higher MR effect compared to isotropic MRE. The dynamic characterization and modeling of MRE are studied by Yang et al.(2013) for seismic isolation. The Bouc-Wen model is employed to simulate the dynamic characteristic of the MRE vibration isolator. The predicted and measured hysteresis loops are compared for their accuracy. The investigation concludes that error between the predicted and measured hysteresis reduces by adequately adjusting the parameters of the Bouc-Wen model. Ying et al.(2013) developed the nonlinear model for the smart magnetorheological visco-elastomer (MRVE). The nonlinear hysteresis loops of MRVE are compared with the newly developed model for the variable magnetic field. The proposed model can be used for the control applications of MRVE based smart devices.

Hegde et al. (2014) studied the effect of particle sizes on the properties of the MRE. The different size particles are used to prepare MRE samples at a volume fraction of 25%, and reported that the smaller particles exhibit a higher MR effect. The MRE variable stiffness and damping isolator (VSDI) for the base isolation is developed by Behrooz et al. (2014a). The performance of VSDI is studied in double lap shear mode, and the Bouc-Wen model is employed to the hysteresis loops of characterized MRE VSDI. It is suggested that the Bouc-Wen model can be used for the simulation of model-based controllers. Hegde et al. (2015) studied the dynamic properties of natural rubber-based isotropic thick MREs. They reported that the particle concentration of 25% by volume is optimum, and the MRE effect increase with the increase in the magnetic field.

Further, softer matrix materials exhibit a higher MRE effect compared to the harder matrix material. Kim et al. (2015) studied the performance of anisotropic MRE under the variation of input current. The electromagnetic finite element method (FEMM) and the magnetic flux generator (MFG) is employed for the optimization of magnetic flux density generated by the magnetic flux generator (MFG). It is reported that the desired

input current is achieved from the study conducted for the higher shear modulus of MRE. Yu et al. (2015) developed the nonparametric model of the MRE base isolator using the neural network which was improved by the ant colony algorithm. The ant colony algorithm is employed to obtain the optimal weights of the hysteresis loops of MRE base isolator. The proposed model is very effective in prediction of the model of MRE.

2.3 Magnetorheological Elastomer Vibration Isolation with Controller Strategies

The field-dependent properties of MRE are essential for semi-active vibration control of the vibration isolation. This makes it a very effective method of vibration control for machine components and civil structures. Most research works published on the dynamic performance of MRE isolation with control strategies are grouped in this section. The MRE-based Tunable vibration absorber (TVA) is developed for the cryogenic cooler by Kim et al. (2011). The operating frequency of the cooler is 50Hz. The developed TVA is highly effective than passive absorber in the variable frequency excitation for the vibration reduction of a cryogenic cooler. The performance of the semi-active controller on a real-time MRE-based vibration isolator was studied by Opie and Yim (2011). The variation of storage modulus and the damping factor is recorded by varying the magnetic field. It evident presented from the result that the MRE-based vibration isolator with a semi-active controller reduces the amplitude of payload by 16-30% compared to the passive system.

Liao et al. (2012b) investigated the performance of the tunable stiffness and damping vibration isolator based on MRE. The stiffness is controlled by changing the magnetic field, and the voice coil motor is used to vary the damping of the isolator. With the ON-OFF controller, the amplitude of resonance reduces by 61.5%, and the maximum amplitude reduction of the payload is 50 %, respectively. Jung et al. (2011) studied the dynamic properties of the MRE base isolation system for the scaled model of building structure. The controller is developed for random excitation. It reported that the proposed MRE base isolation with a fuzzy controller is more effective than conventional base isolation in vibration reduction. The dynamic performance of a MRE

base isolator for a seat suspension has been investigated by Li et al. (2012). No resonance-based controller is used to change the stiffness of MRE to avoid resonance. That reduction in vibration amplitude is high in semi-active-based MRE compared to passive isolation systems. Eem et al. (2013) investigated the dynamic performance of the MRE base isolator for seismic excitations. The base isolation is subjected to random excitation, and the natural frequency of the isolator shifts leftward with the influence of the magnetic field. This showcases the effectiveness of the MRE base isolator.

Fu et al. (2013) developed a novel MRE-based buffer to reduce the impact during the drop crash. The human simulated intelligent control and intelligent control strategy are employed to vary the field-dependent stiffness of the MRE. The developed MRE-based buffer with controller reduces the acceleration of impact effectively. The model-based Lyapunov control theory is used for three-story MRE smart vibration isolation by Behrooz et al. (2014b). The performance of the proposed controller is compared with the ON-OFF controller. The results concluded that both controllers have some issues with real-time implementation. Lyapunov controller requires an accurate model, and the ON-OFF control exhibits oscillation response. Li and Li (2015) optimized the distribution of magnetic fields using numerical analysis for a multilayer MRE vibration isolation. The analysis shows that the developed magnetic circuit has uniform magnetic field distribution and the amplitude of the magnetic field decreases with an increase in deformation MRE vibration isolator.

Xing et al. (2015) investigated the transmissibility of a multilayer magnetorheological elastomer bearing prototype for bridge superstructures. The experimental results show that the system's frequency can be tuned from 10 to 20 Hz, and the displacement transmissibility value reduces 20.67%. The MRE vibration isolator for the for-precision vibration system having high-frequency vibration and uncertainties is developed by Fu et al. (2016). The frequency shift of the MRE vibration isolator is 107.3Hz to 187.3Hz. The model-free fuzzy controller is designed to control the input current. Even with parameter uncertainties of MRE, the reduction of transmissibility of 54.4 % is reported with the proposed controller. The MRE-based vibration isolator for the two-story building structure is developed by Nguyen et al. (2018). The six parameters model is introduced to estimate the dynamic properties of the MRE. The shifting frequency of

2.5Hz is achieved for the applied current. A fuzzy controller is employed to regulate the current input. The maximum reduction relative displacement between the base plate and third mass with the fuzzy controller is 30%. The fuzzy controller is highly effective in the vibration reduction of a two-story building. Tao et al. (2019) developed the MRE isolation system for the strap-down inertial measurement unit and analyzed its performance with the on-off and phase-based controller. The phase-based controller efficiently reduced the acceleration of vibration by 17.67%. Phase-based control strategy precisely tunes the natural frequency of MRE absorber with excitation frequency but takes a long time of 4 s. Gu et al. (2019) studied the semi-active MRE base isolation performance for a three-story building structure with different controller strategies. The neural network-based fuzzy controller was proposed to handle the inherent nonlinearity and uncertainties of MRE. The proposed controller is optimized by a non-dominated sorting genetic algorithm type II. The proposed control is compared with the Bang-Bang controller and reported that the proposed controller more effective in vibration reduction even with the nonlinearity of MRE. Jin et al. (2020) studied the semi-active suspension with variable stiffness and variable damping (VSVD) for high-speed railway vehicles. The short-time Fourier transform (STFT) and sky-hook based control strategies are employed and it is reported that the VSVD semi-active suspension effectively reduces the vibration compared to passive, pure variable stiffness and pure variable damping.

2.4 Magnetorheological Elastomer Vibration Absorber with Controller Strategies

Traditional vibration absorbers are auxiliary devices that reduce the vibration of machine components and structures. Vibration reduction in systems is achieved by coinciding the system's operating frequency with the natural frequency of the absorber. However, if the natural frequency of the absorber doesn't coincide with the operating frequency, the effect of vibration reduction also reduces. This is effectively addressed with the MRE-based vibration absorber, which uses the field-induced properties of MRE to change the natural frequency of the vibration absorber. Several researchers have studied the MRE-based vibration absorber with different controller strategies. Deng and Gong (2008) studied the shift-frequency capability of the MRE adaptive

tuned vibration absorber (ATVA) in double in shear mode. The shear modulus increase as magnetic field intensity increases. The natural frequency of the MREAVTA increase from 27.5Hz to 40Hz. It is evident from the results that the vibration reduction ability of the proposed MRE ATVA is higher compared to the traditional vibration absorber. The field-dependent properties of MRE vibration absorber in shear mode with PZT based squeeze-strain are investigated by Ni et al. (2009). The ON-OFF controller activates PZT and a tuning control strategy is employed to vary stiffness MRE to suppress the vibration of the primary system. The proposed PZT-based MRE vibration absorber exhibits higher effectiveness in reducing vibration compared to conventional MRE vibration absorbers.

Xu et al. (2010) developed the active-compensated MRE-based adaptive tuned vibration absorber (ATVA). A voice coil motor controls the active force to the MRETVTA. The active force effectively reduces the damping of the MRETVTA compared to without active compensated MRE ATVA, which leads to the higher amplitude reduction of the primary system. An active-adaptive tuned vibration absorber based on MRE (MREAATVA) is developed by Liao et al. (2011). The natural frequency of the MRE AATVA shift from 11 Hz to 18 Hz at an input current of 0.7 A. The damping ratio was reduced to 0.08 from 0.19 by the activation force. This shows the effectiveness of the MREAATVA in vibration control of primary structure compared to MRETVTA.

Liao et al. (2014) designed a phase-based stiffness tuning controller for the MRE vibration absorber (MREDVA). The proposed control algorithm doesn't require an accurate relation between the natural frequency of the DVA and current. With nonlinearity and parameter uncertainties of the MRE. The proposed controller tune the natural frequency MRETVTA with the excitation frequency accurately in less than 4 sec. The laminated multi-layer MRE vibration absorber for the low frequency and large amplitude applications by Sun et al. (2015). The lowest natural frequency of 3.2 Hz is achieved for the current 4A and stroke length of 13.6mm. It is evident that the laminated multilayer MRE vibration absorber is more efficient in vibration mitigation than the passive vibration absorber.

2.5 Closure

The literature review concludes that MRE is an effective smart material for vibration control in isolators and absorbers. In the presence of a magnetic field, it changes its stiffness and damping properties. Several parameters such as matrix materials, size and shape of the iron particles, operational modes, configuration of magnetic circuit and control strategies influence the performance of MR elastomer-based smart devices. However, among all these parameters, the application of control strategies for smart devices is less explored.

2.6 Motivation

The real-time implementation of the MRE vibration isolator and absorber requires a controller to vary the electric current of the electromagnet. The controllers are classified as linear, nonlinear and adaptive according to their working principles. As a viscoelastic composite material, MRE behaves nonlinearly at higher displacement and poses time-varying properties. This behavior of MRE restricts the use of linear controllers for the MRE vibration isolator and absorber. Therefore, it is required to design nonlinear robust and intelligent adaptive controls that are more suitable for dynamic systems with nonlinearity and time-varying properties. The present research work focuses on the development of nonlinear robust and intelligent adaptive control strategies for MRE vibration isolator and absorber.

2.7 Research Objectives

The objectives of the proposed work are as follows

- To perform field-dependent dynamic characterization of MRE under variable frequencies and displacement for double lap shear loading conditions.
- To estimate the phenomenological model's parameters under the influence of the variable magnetic field, frequencies, and displacement.
- To investigate the performance of MRE vibration isolation with the model-based controllers.
- To design an intelligent control based on the neural network adaptive observer for MRE vibration isolation.

- To investigate the performance of MRE Adaptive Tunable Vibration Absorber (MRE ATVA) using model-free adaptive fuzzy sliding mode control.

3. Dynamic Characterization and Modelling of Magnetorheological Elastomer

3.1 Introduction

The present chapter discusses the dynamic behavior of Magnetorheological elastomer (MRE) under variable magnetic field, operating frequency and displacement. The dynamic characterization of anisotropic MRE is performed as per the dynamic blocked transfer stiffness method (Poojary et al. 2016). The hysteresis loops are extracted to explain the viscoelastic properties of MRE. The outline of the present section is below

1. Preparation of RTV silicone rubber-based isotropic and anisotropic MRE samples and conducting the Scanning Electron Microscope (SEM) to observe the particle distribution.
2. Development of experimental setup as per dynamic blocked stiffness approach for dynamic characterization of MRE.
3. Analyzing the viscoelastic properties of MRE from hysteresis loops for variable frequency, magnetic field and displacement.
4. Bouc-Wen modeling of MRE.

3.2 Preparation of Magnetorheological Elastomer

MRE constitutes Room Temperature Vulcanization (RTV) silicone rubber (Performance Polymers, MoldSil 102LL with CAT 9) as the matrix and carbonyl iron particles (BASF, Type CN, Average diameter-5 μ m) as its filler material. 73% and 27% volume fraction of the RTV silicone rubber and carbonyl iron particles have been considered. The MRE samples are prepared with thorough mixing of RTV silicone rubber and carbonyl iron particles. Silicone oil of 10 % weight of the matrix is added to reduce the no-field stiffness of the MRE. The prepared MRE mixture is poured into a mold of 25 \times 25 \times 3 mm and degassed in a vacuum chamber to remove air bubbles. Further, the samples are cured at room temperature without and with a magnetic field of 0.7 T for 24 hours to obtain the isotropic and anisotropic MREs shown in Figure 3.1 (Visakh et al., 2013).

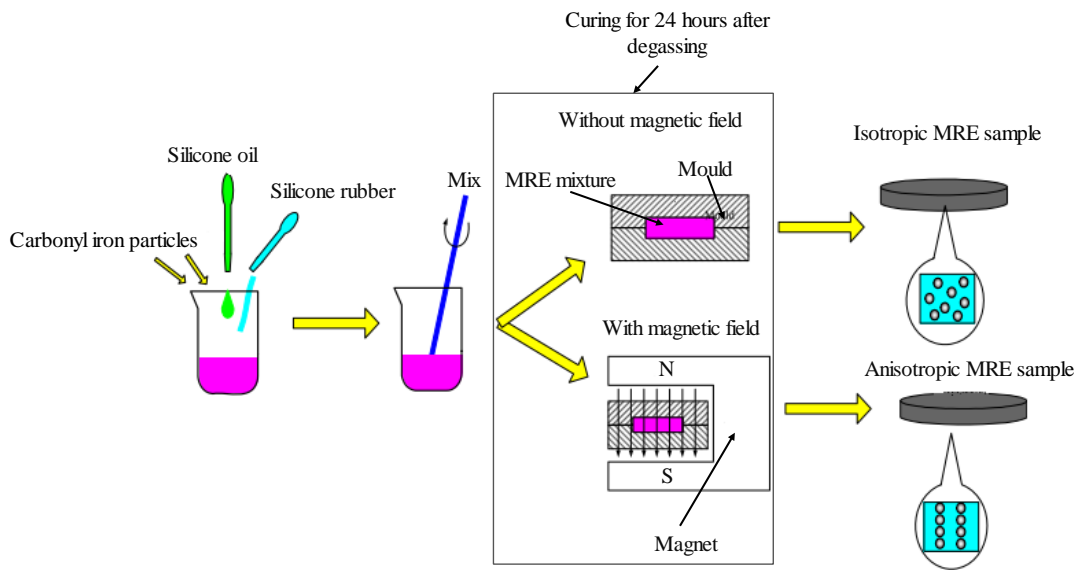


Figure 3.1 Preparation of isotropic and anisotropic MRE (Visakh et al., 2013).

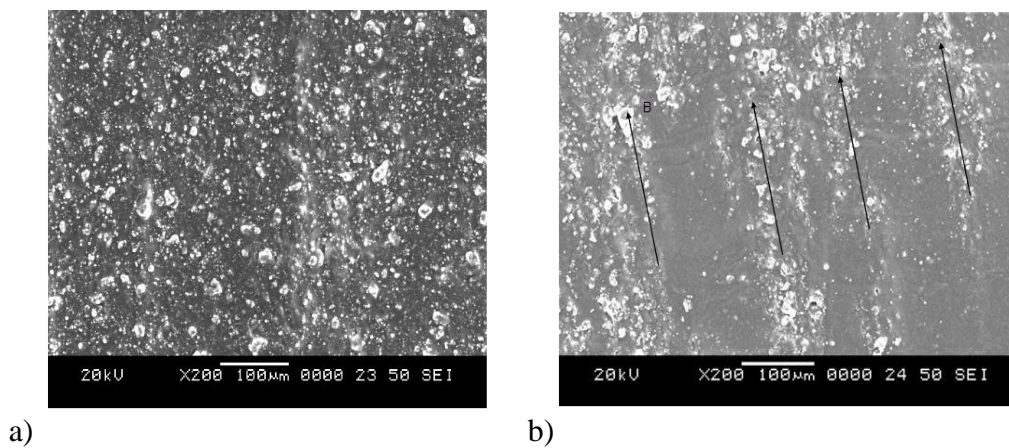


Figure 3.2 SEM image of MRE a) isotropic and b) anisotropic.

The particle distribution of isotropic and anisotropic MRE samples is shown in Figure 3.2. The particles are randomly distributed in isotropic MRE, and in the case of anisotropic MRE, the particles are aligned in the direction of the magnetic field. The literature review concludes that anisotropic MRE exhibits higher dynamic properties than isotropic. Therefore, all the upcoming investigations are carried out with anisotropic MRE.

3.3 Experimental Setup of Dynamic Characterization of the MRE

Figure 3.3, Figure 3.4 and Figure 3.5 show schematic, photograph and close view photograph of the experimental setup of dynamic characterization of MRE in double lap shear. The prepared anisotropic MRE samples are placed in between two 3D printed fixture. One end of the fixture is coupled to the shaker (Make: YMC) via a stinger, and another end is rigidly blocked through a force transducer is subjected to harmonic excitation by a function generator (Make: Agilent; Type 33220A) via a power amplifier. Accelerometer (Make: Kistler; Type K-shear) and force transducer (Make: Kistler) are mounted on the input and output side of the fixture to measure the respective signals (force and displacement). The signals are acquired with the data acquisition module NI-9234 (National Instruments), and a DC power supply is used to induce a magnetic field in the electromagnet.

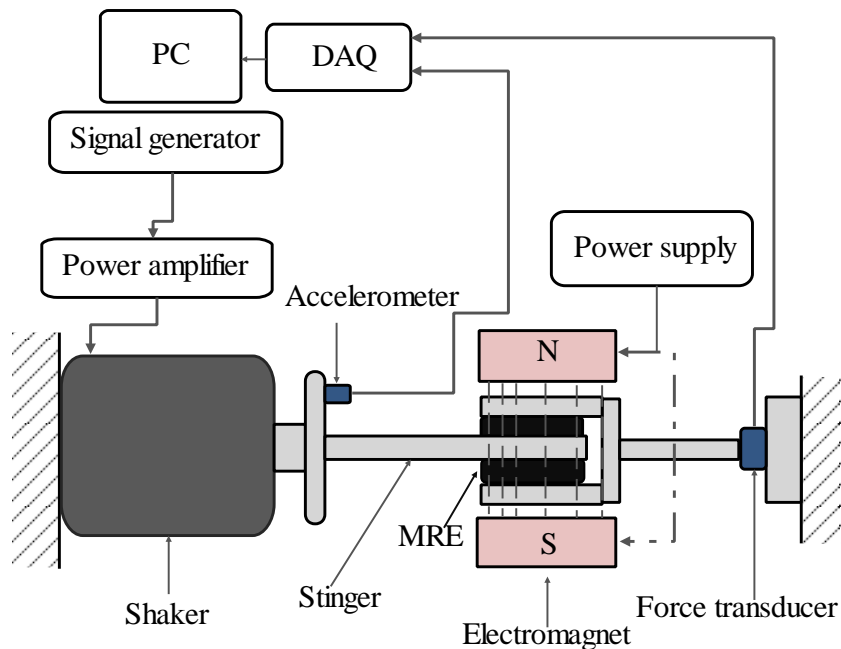


Figure 3.3 Schematic of the experimental setup of dynamic characterization of MRE.

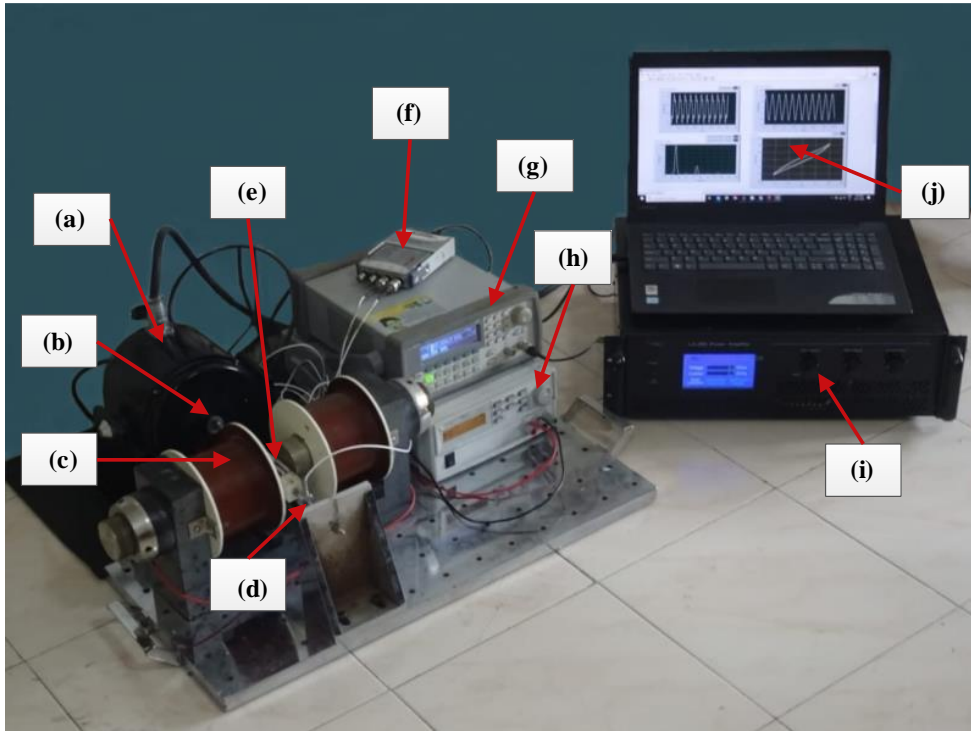


Figure 3.4 Photograph of the experimental setup of dynamic characterization of MRE. (a) Electrodynamic shaker, (b) Accelerometer, (c) Electromagnet, (d) Force transducer, (e) MRE, (f) NI-9234, (g) Function generator, (h) DC power supply, (i) Power amplifier and (j) LabVIEW.

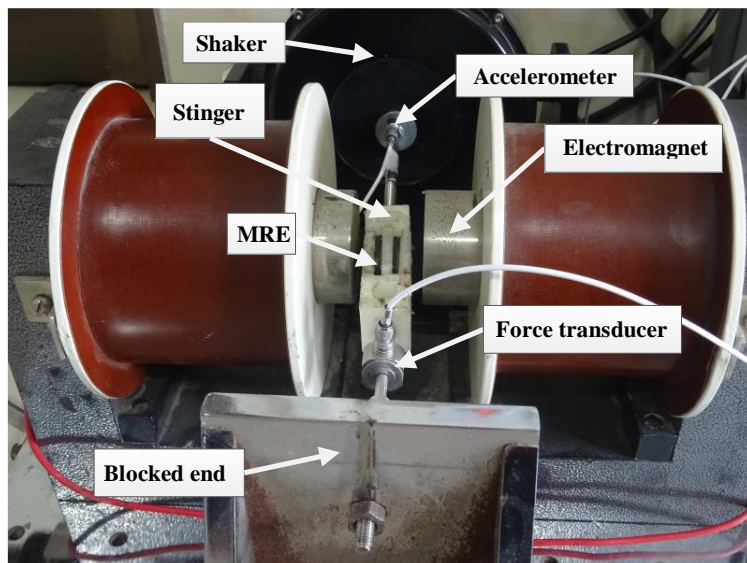


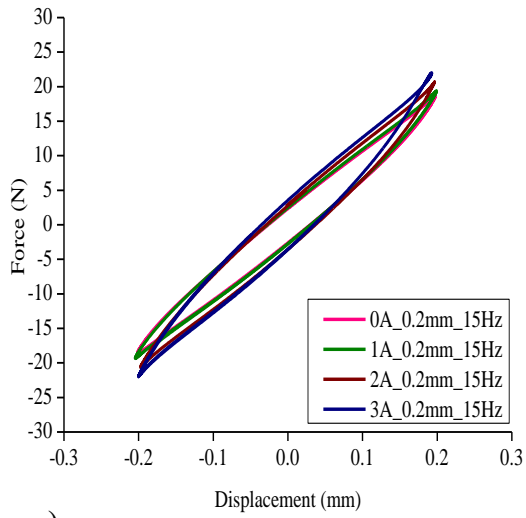
Figure 3.5 Close view of the MRE assembly.

3.4 Stiffness and Damping of MRE

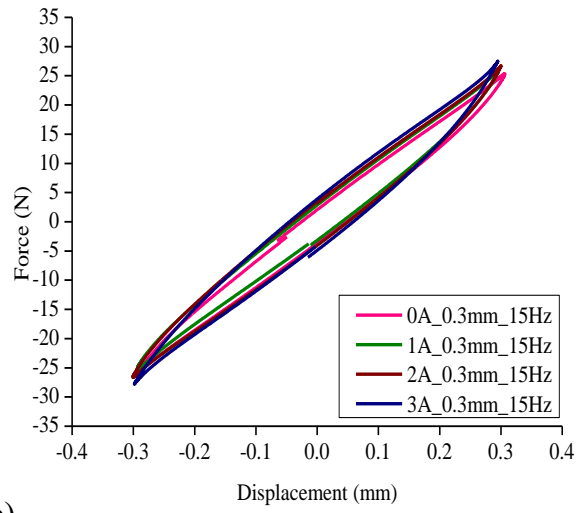
Dynamic characterization of MRE is performed under four variable frequencies of 15Hz, 30Hz, 45Hz and 60Hz at displacements of 0.2mm, 0.3mm, 0.5mm and 0.6mm and current of 0A, 1A, 2A and 3A. The MRE is subjected to steady-state excitation for a combination of each frequency and displacement at all input current, and force-displacement data is recorded. The force-displacement graphs or hysteresis loops are considered for the analysis of the dynamic properties of the MRE.

3.4.1 Dynamic Characterization under Variable Current

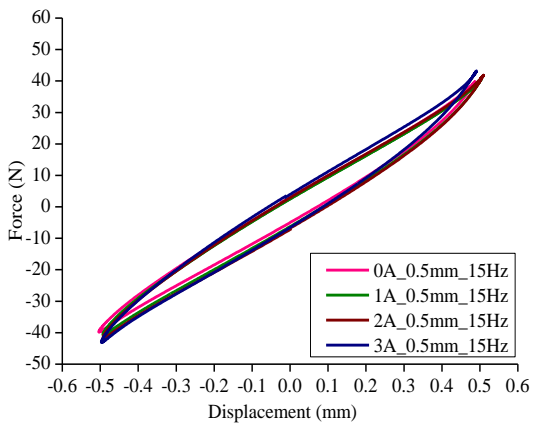
The hysteresis loops of the variable current, constant displacement and frequency are plotted from Figure 3.6 to Figure 3.9. The current is varied from 0A to 3A in the step of 1A and the displacement and frequency are kept constant for each graph. Figure 3.6 (a) depicts the hysteresis loop of variable current with a displacement of 0.2 mm and a constant frequency of 15 Hz. It is concluded that, as the current increases from 0 A to 3 A, the slope of the force-displacement curve rises, depicting the increase in the stiffness of MRE. The stiffness of the MRE increases under the influence of the input current/magnetic field. In the presence of a magnetic field, the carbonyl iron particles align themselves in the direction of the applied field. This results in the formation of magnetic dipoles between adjacent carbonyl iron particles, which induces compressive forces on the interlaying matrix, increasing the stiffness of MRE (Poojary and Gangadharan 2017)(Shenoy et al. 2020). It is also observed from Figure 3.6(a) that there is no significant variation in the area of hysteresis loops indicating there is no change in the damping of the MRE with the variable magnetic field/current (Yang et al. 2012a). Similar results are observed for the all-remaining cases of the variable current, constant displacement and constant frequency.



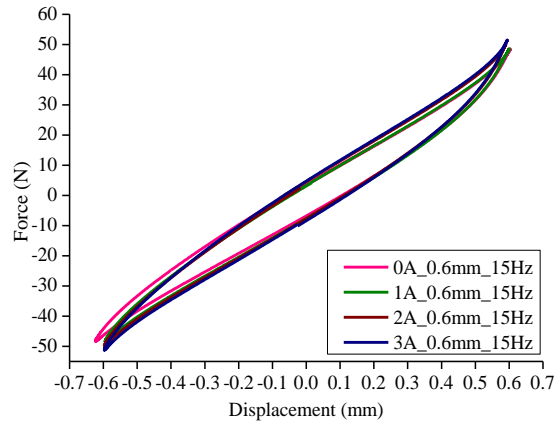
a)



b)

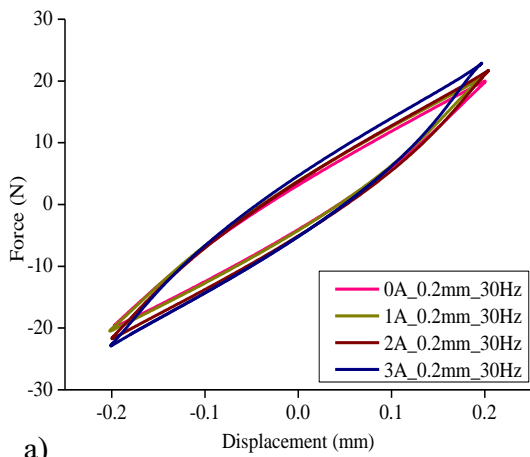


c)

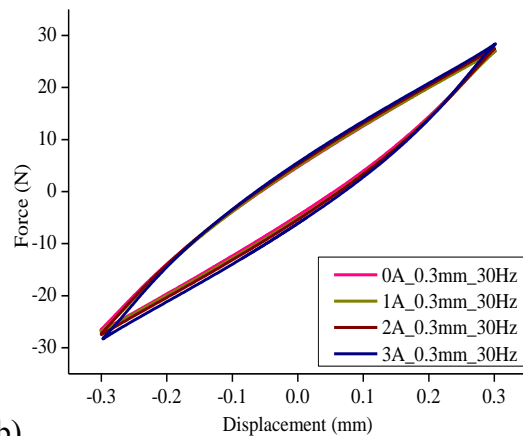


d)

Figure 3.6 Hysteresis loops of the MRE for variable current at a constant frequency of 15Hz and displacement of a) 0.2mm, b) 0.3mm, c) 0.5mm, and d) 0.6mm.



a)



b)

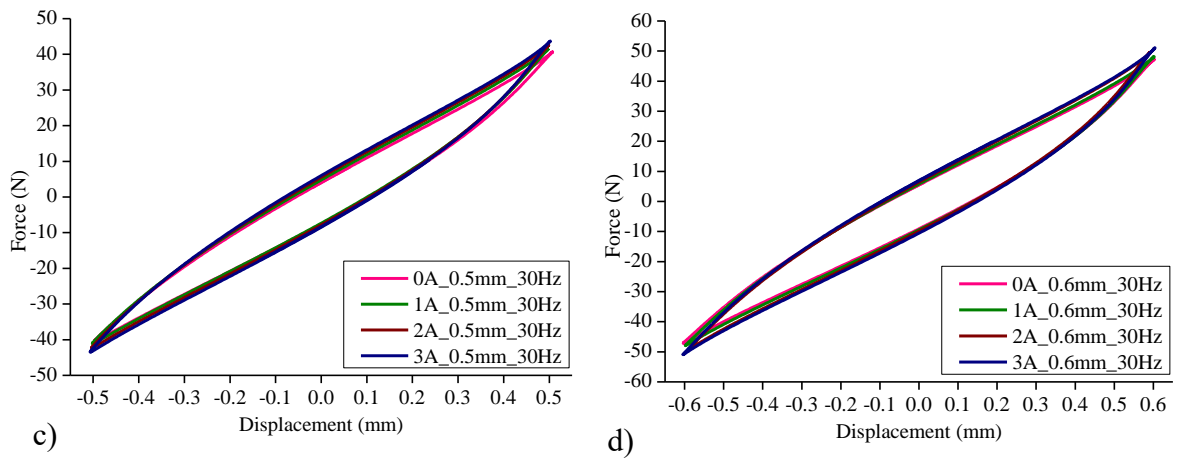


Figure 3.7 Hysteresis loops of the MRE for variable current at a constant frequency of 30Hz and displacement of a) 0.2mm, b) 0.3mm, c) 0.5mm, and d) 0.6mm.

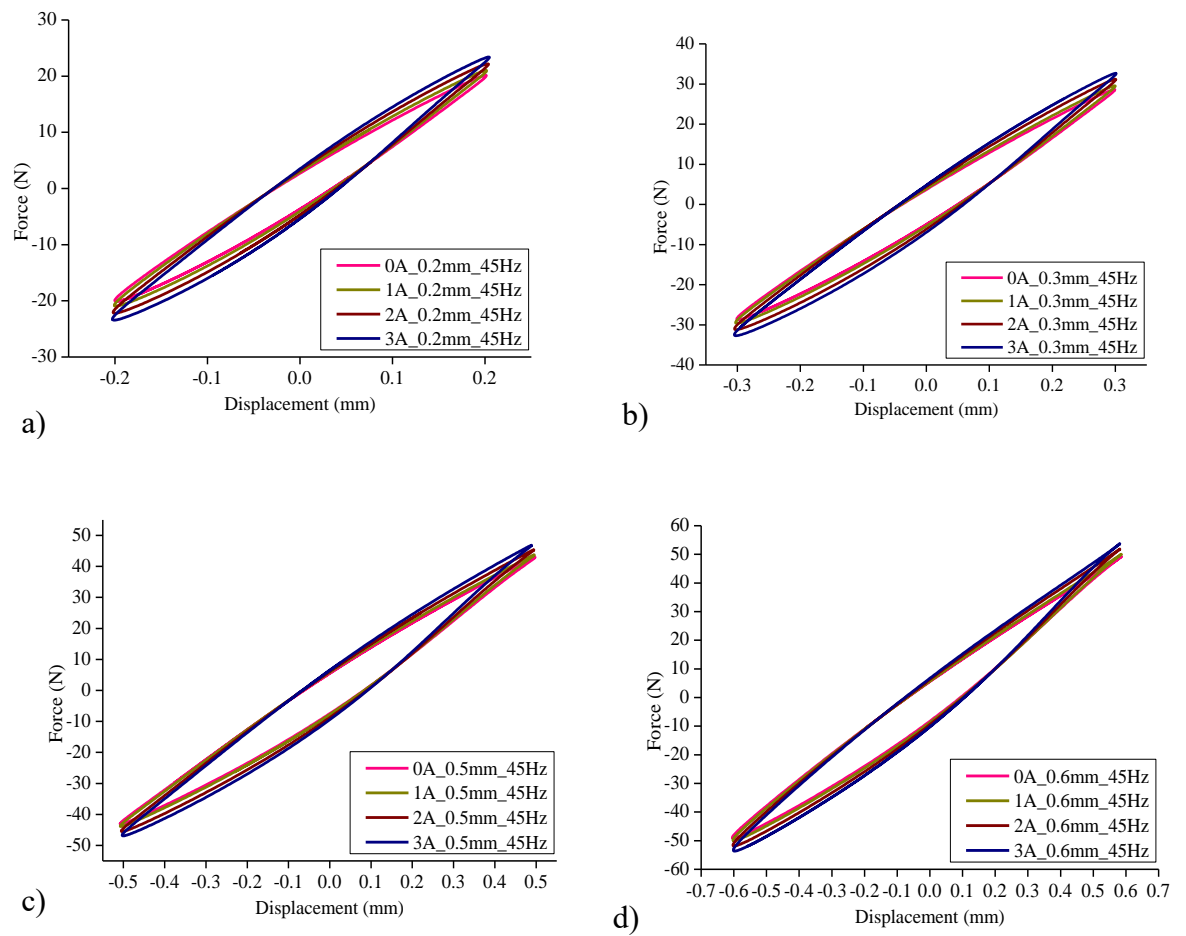


Figure 3.8 Hysteresis loops of the MRE for variable current at a constant frequency of 45Hz and displacement of a) 0.2mm, b) 0.3mm, c) 0.5mm, and d) 0.6mm.

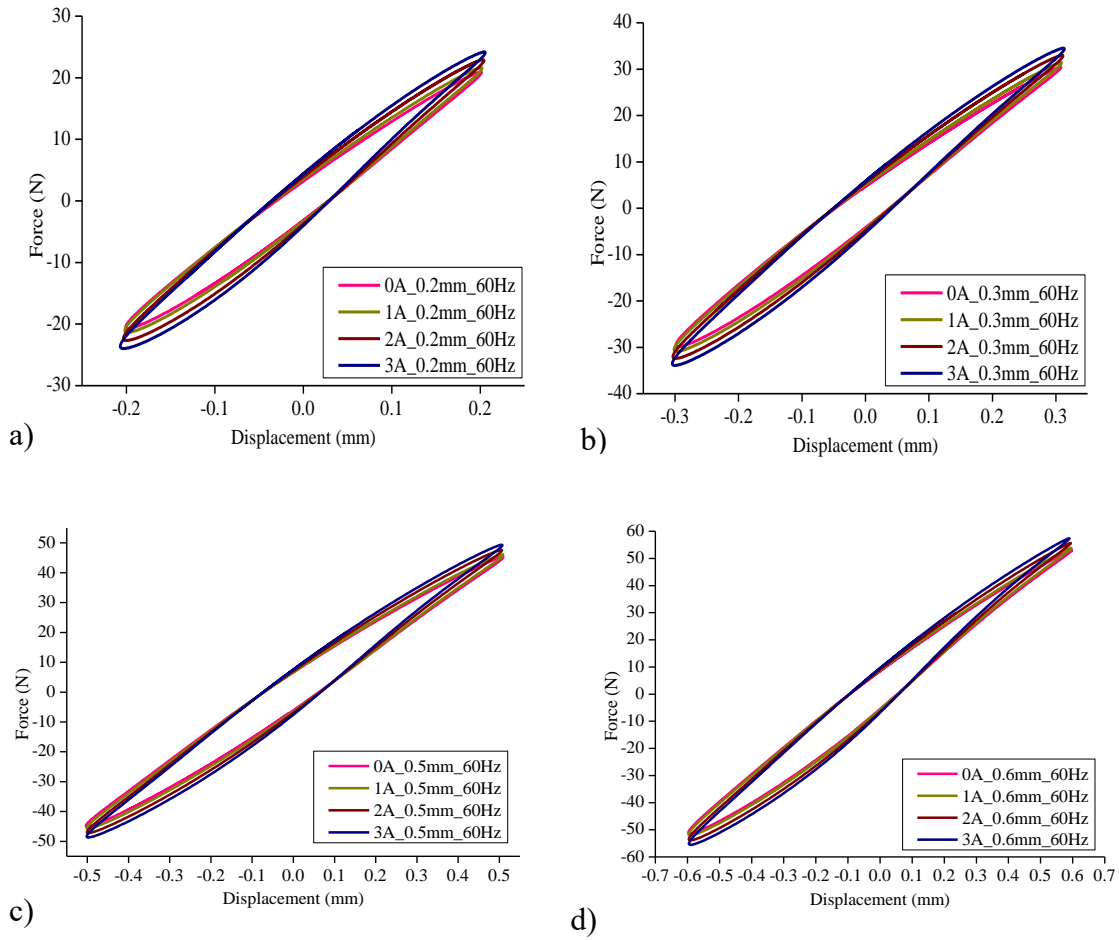


Figure 3.9 Hysteresis loops of the MRE for variable current at a constant frequency of 60Hz and displacement of a) 0.2mm, b) 0.3mm, c) 0.5mm, and d) 0.6mm.

3.4.2 Dynamic Characterization under Variable Displacement

Figure 3.10 to Figure 3.13 depict the hysteresis loops of variable displacement, constant current and frequency. The displacements consider for this study are 0.2mm, 0.3mm, 0.5mm and 0.6mm. The remaining parameters, like current and frequency, are kept constant. Figure 3.10 (a) depicts the hysteresis loop of variable displacement with a current of 0A and a constant frequency of 15 Hz. The plot shows that the increase in input displacement leads to an increase in the area of the loop and a decrease in the slope, indicating a reduction in stiffness and an increase in damping of MRE. The decline in stiffness is attributed to the formation of the gap between the bound rubber

and the individual iron particles (Poojary et al. 2017). Also, the increase in damping is credited to the rise in the interfacial sliding friction between the particle and the bound rubber (Chen et al. 2008). A similar effect is observed for all cases of the variable displacement, constant current and constant frequency.

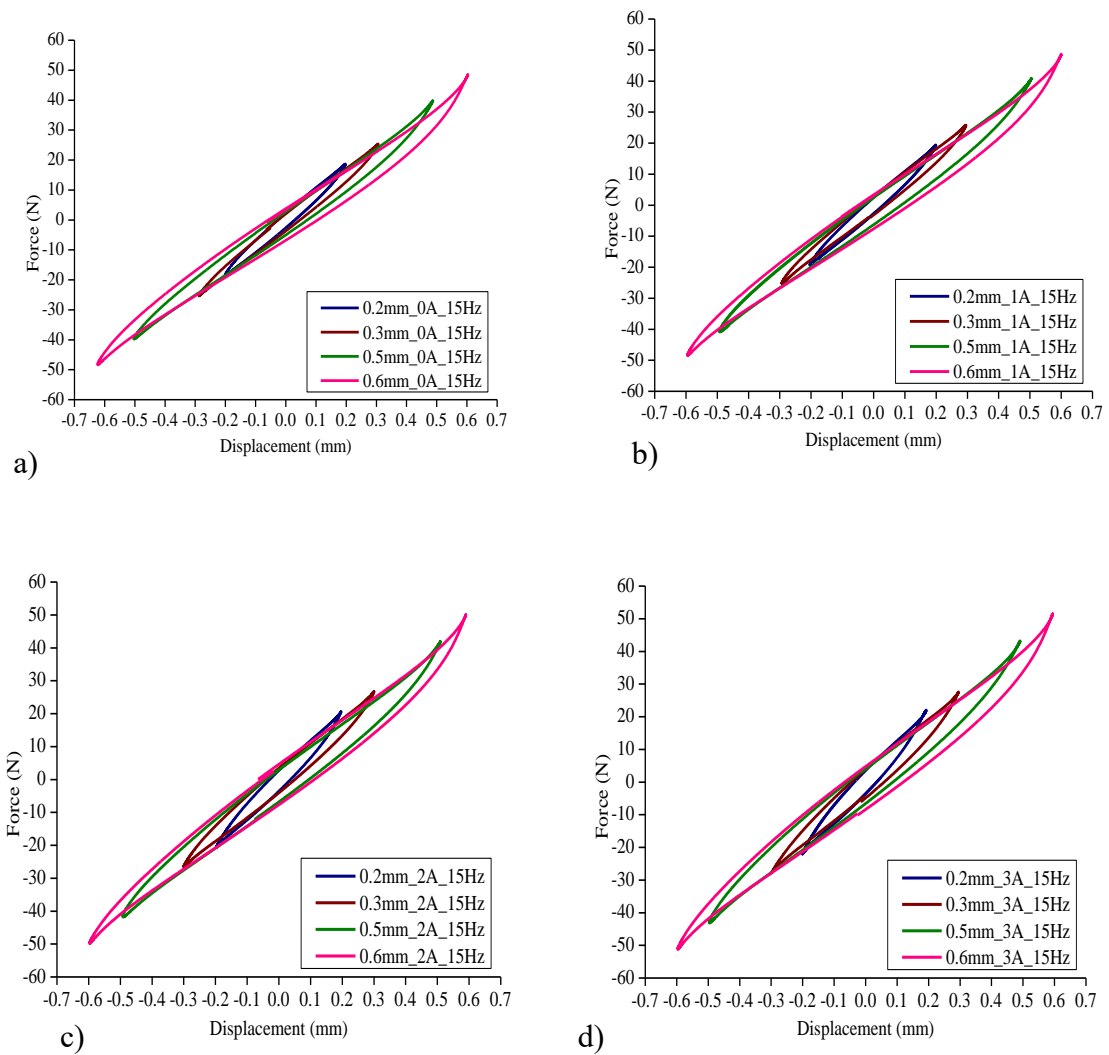


Figure 3.10 Hysteresis loops of the MRE for variable displacement at a constant frequency of 15Hz and current of a) 0A, b) 1A, c) 2A, and d) 3A.

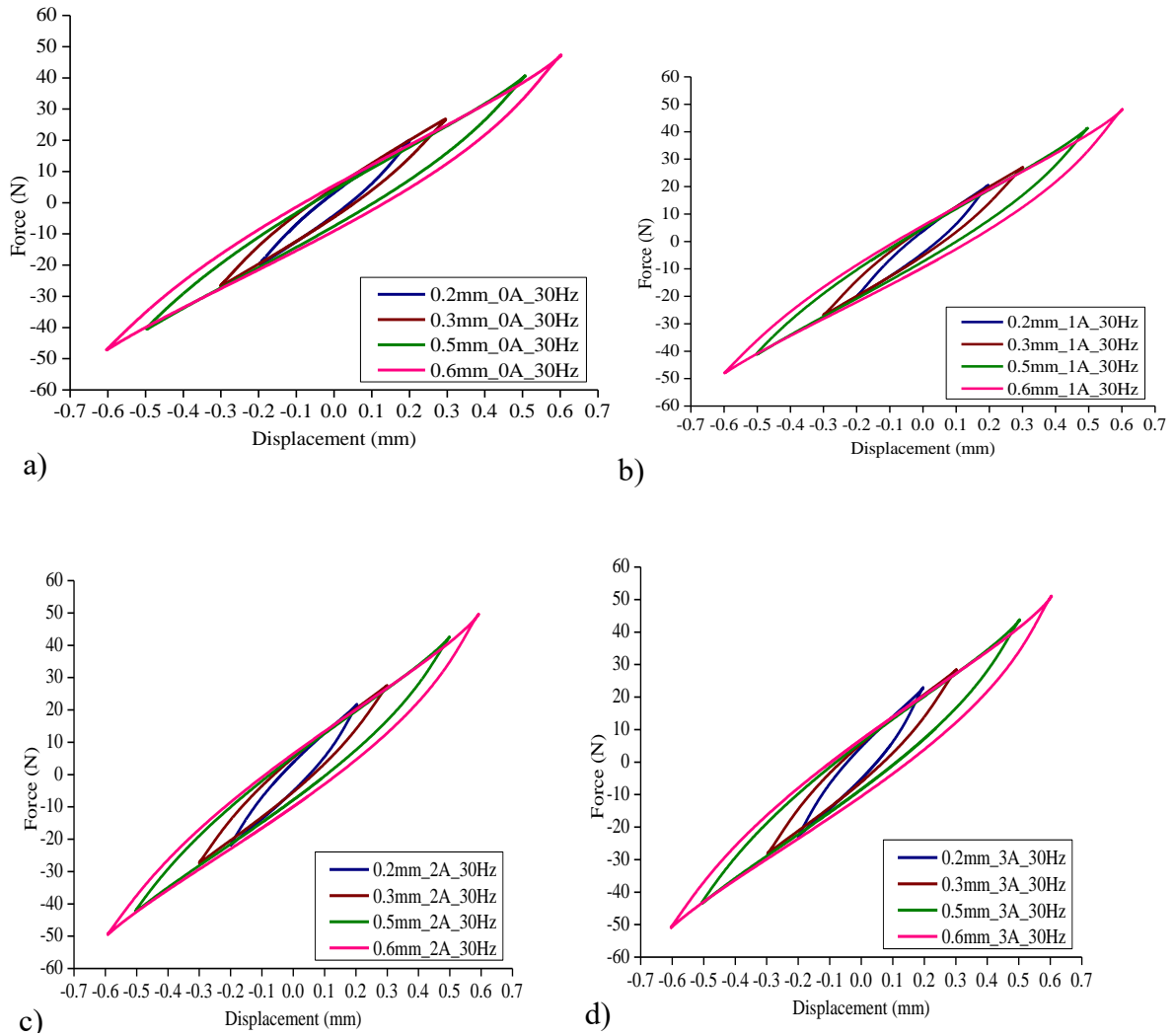
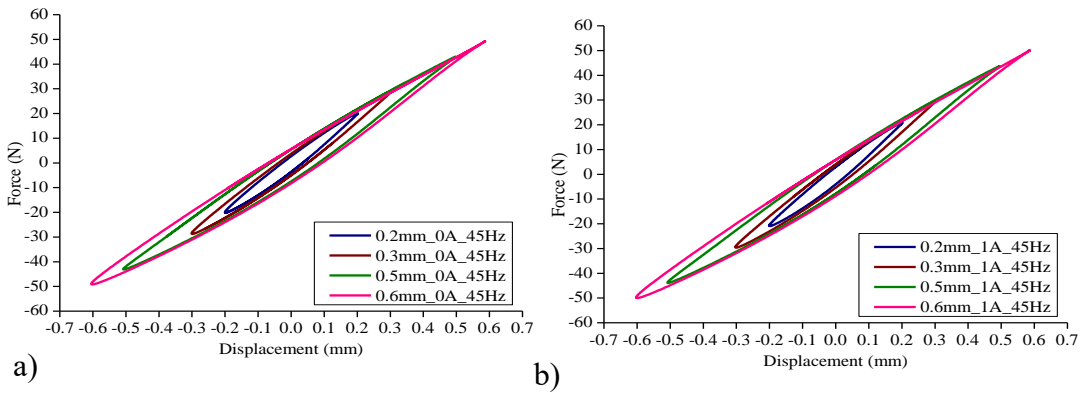
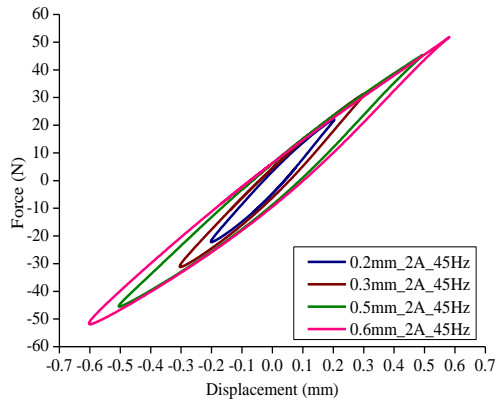
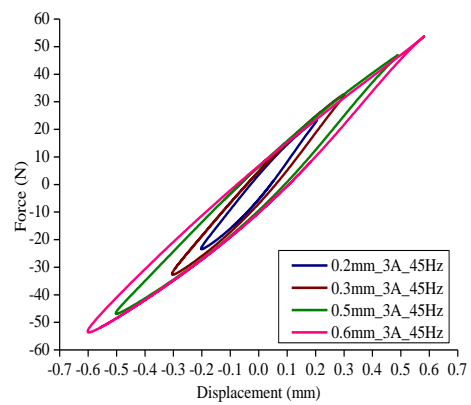


Figure 3.11 Hysteresis loops of the MRE for variable displacement at a constant frequency of 30Hz and current of a) 0A, b) 1A, c) 2A, and d) 3A.



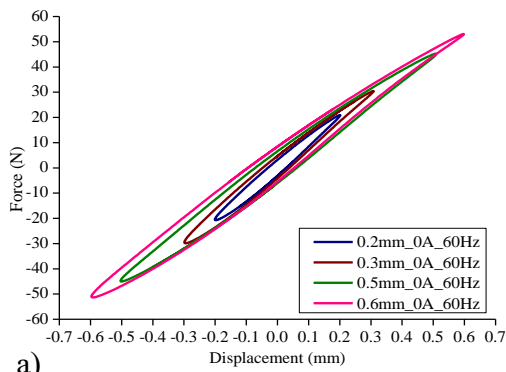


c)

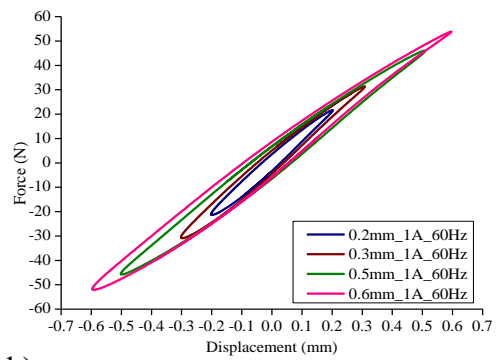


d)

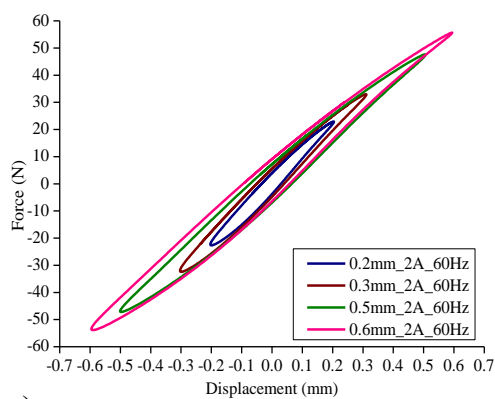
Figure 3.12 Hysteresis loops of the MRE for variable displacement at a constant frequency of 45Hz and current of a) 0A, b) 1A, c) 2A, and d) 3A.



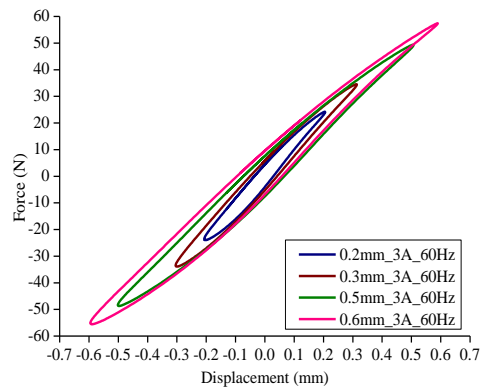
a)



b)



c)



d)

Figure 3.13 Hysteresis loops of the MRE for variable displacement at a constant frequency of 60Hz and current of a) 0A, b) 1A, c) 2A, and d) 3A.

3.4.3 Dynamic Characterization under Variable Frequency

The hysteresis loops of variable frequency, constant current and displacement are depicted from Figure 3.14 to Figure 3.17. The frequencies are varied from 15Hz to 60Hz in steps of 15Hz. However, the current and frequency are kept constant. Figure 3.14 (a) shows the hysteresis loop of the variable frequency with a constant displacement of 0.2mm and a constant current of 0A. As the frequency of excitation increases, the slope of the hysteresis loop increases resulting in increased stiffness of MRE. This behavior of MRE results from the viscoelastic hardening of rubber material at higher operating frequencies (Poojary and Gangadharan 2017). There is not much variation is observed in the area of hysteresis loops, indicating no influence on damping of the MRE due to variation in operating frequencies. For other cases of variable frequency, constant displacement and a constant current similar trend is observed.

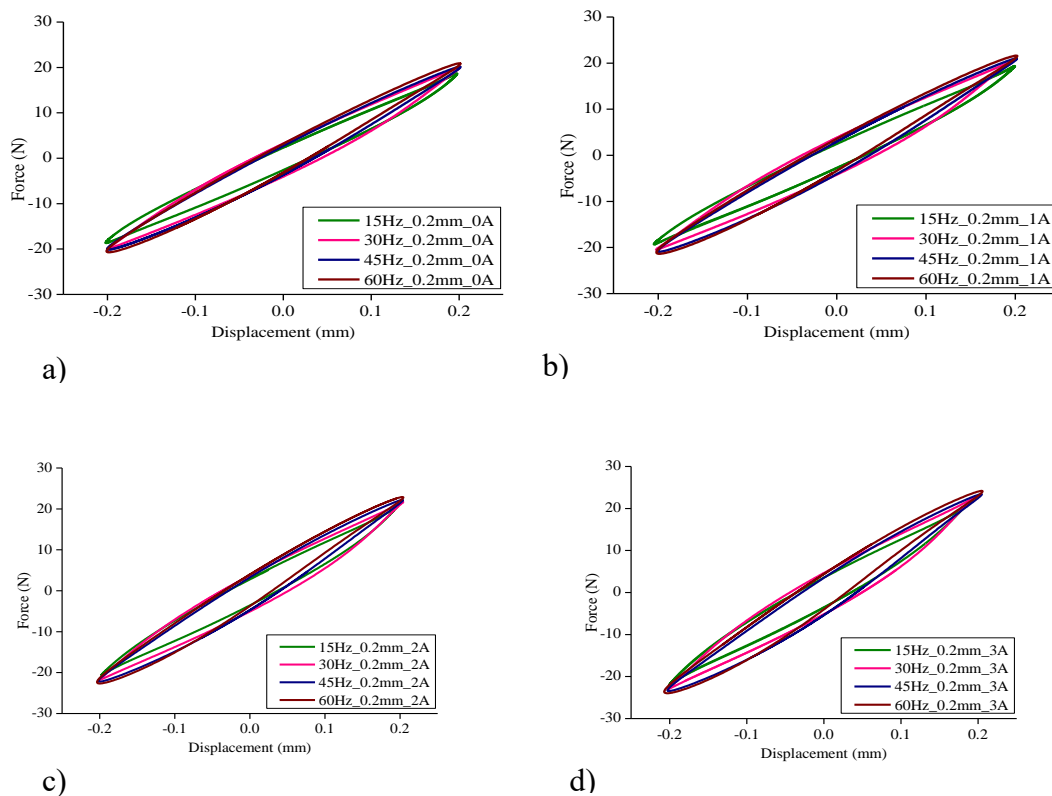
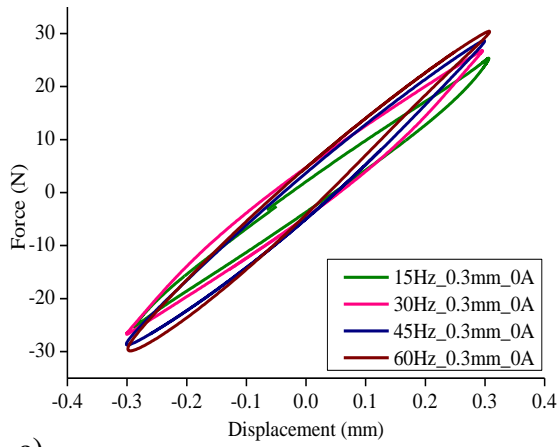
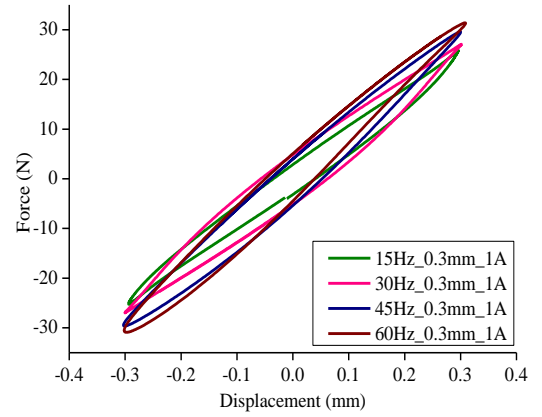


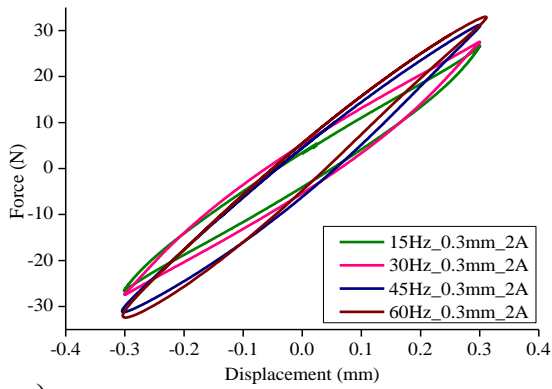
Figure 3.14 Hysteresis loops of the MRE for the variable frequency at a constant displacement of 0.2mm and current of a) 0A, b) 1A, c) 2A, and d) 3A.



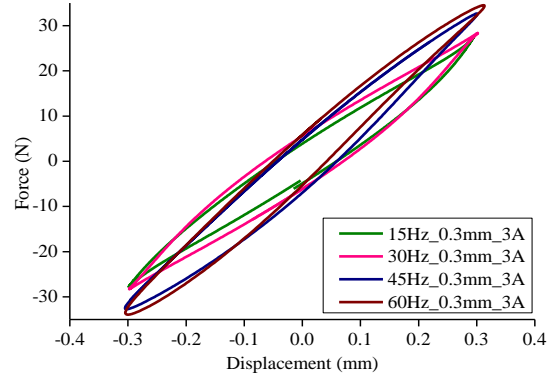
a)



b)

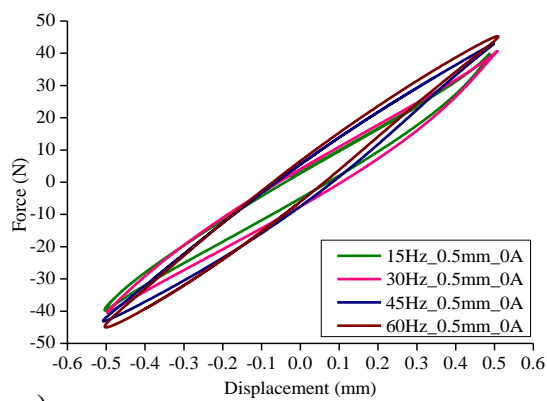


c)

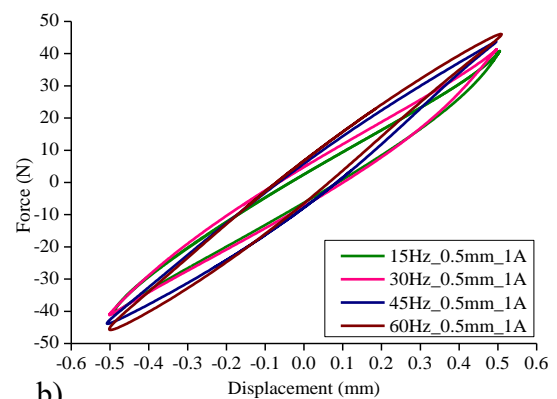


d)

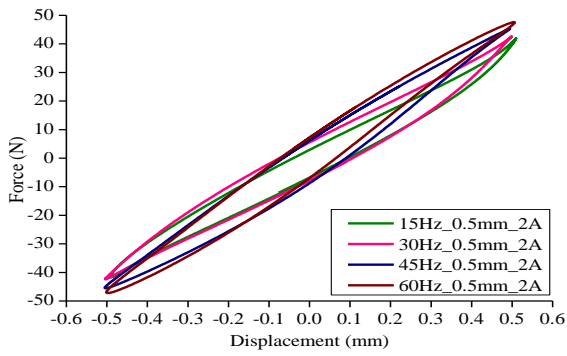
Figure 3.15 Hysteresis loops of the MRE for the variable frequency at a constant displacement of 0.3mm and current of a) 0A, b) 1A, c) 2A, and d) 3A.



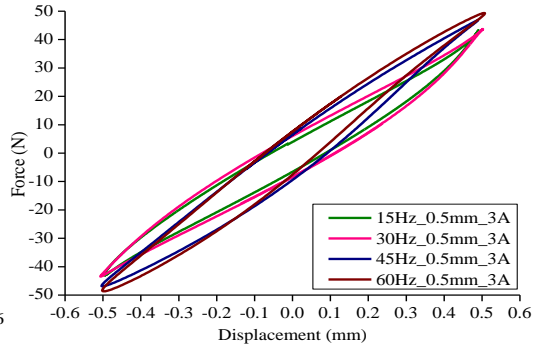
a)



b)

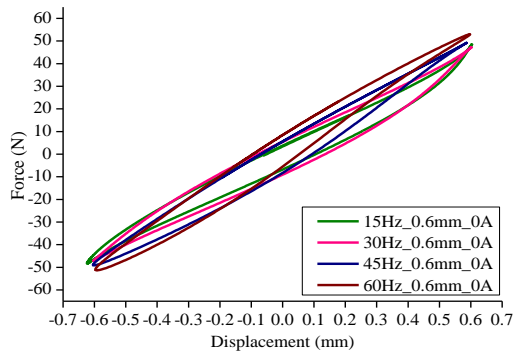


c)

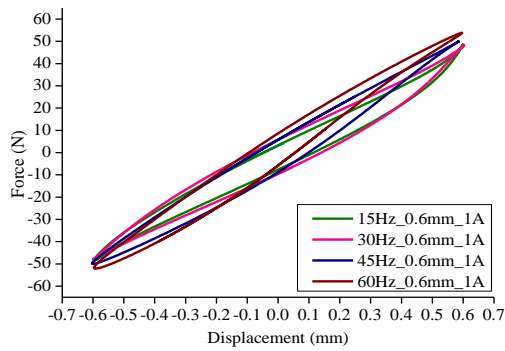


d)

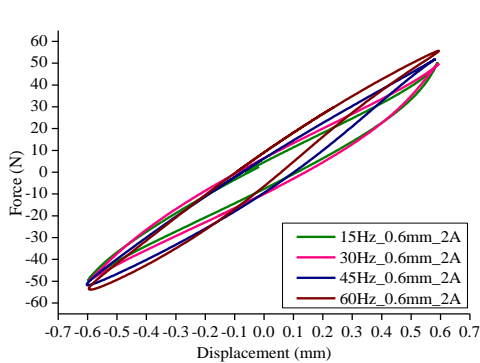
Figure 3.16 Hysteresis loops of the MRE for the variable frequency at a constant displacement of 0.5mm and current of a) 0A, b) 1A, c) 2A, and d) 3A.



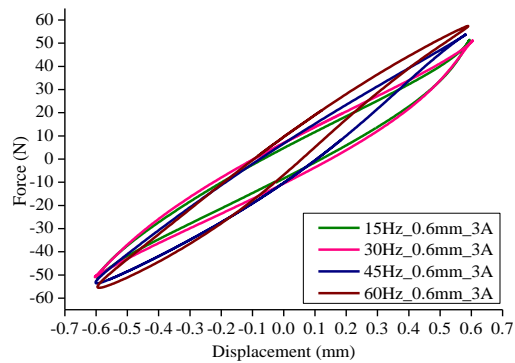
a)



b)



c)



d)

Figure 3.17. Hysteresis loops of the MRE for the variable frequency at a constant displacement 0.6mm and current of a) 0A, b) 1A, c) 2A, and d) 3A.

3.5 Modeling of MRE

The dynamic characterization confirms the field-induced behavior of MRE and the influence of displacement and frequency. This field-induced characteristic of MRE is very useful in vibration control as a semi-active system. The simulations of the semi-active system with a model-based controller need an accurate model of the MRE. The present section deals with the modeling of MRE, considering the Bouc-Wen model.

3.5.1 Bouc-Wen Model

The performance of model-based controllers depends on the precise model of MRE. The Bouc-Wen model precisely predicts the nonlinear behavior of MRE, as proposed by (Yang et al. 2013). Figure 3.18 shows the schematic diagram of the Bouc-Wen model. The mathematic expression (Yang et al. 2013) of the force is written as

$$F = \alpha k_0 + (1 - \alpha)k_0 z + c_0 \dot{x} \quad (3.1)$$

$$\dot{z} = A\dot{x} - \beta|\dot{x}||z|^{n-1}z - \mu\dot{x}|z|^n \quad (3.2)$$

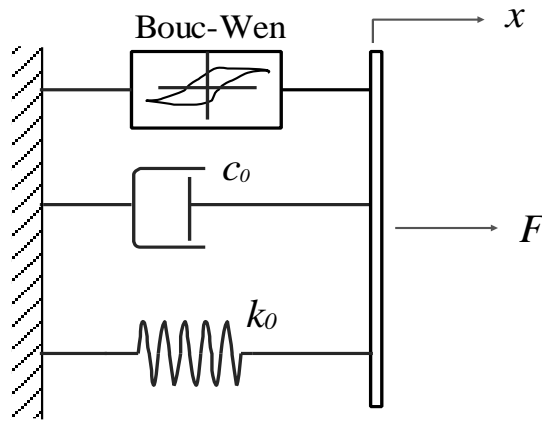


Figure 3.18 Schematic of Bouc-Wen model (Yang et al. 2013).

where, c_0 and k_0 are the viscous coefficient and stiffness of the spring, respectively, α is the stiffness ratio of post-to- pre yielding of and z is an evolutionary variable that describes the feature of the hysteresis loop. A , β , μ , and n are the non-dimensional parameters and defines the size and shape of the hysteresis loop (Gu et al. 2019). The six optimal parameters of the model are estimated in MATLAB/Simulink using the least-square method combined with the Trust-region-reflective algorithm (Yang et al., 2013). The Trust-region-reflective algorithm minimizes the value of the selected function, $g(x)$. It approximates the function $g(x)$ with a simpler function $p(x)$, which

effectively imitates the behavior of $g(x)$ in the neighborhood N (a trust region). It is essential to choose a specific trust region approach and approximate the $p(x)$ value to minimize the function $g(x)$. The objective in this is to minimize the root mean square, which is defined as (Yang et al., 2013),

$$J = \sum_{i=1}^N \sqrt{\frac{(F_{pi} - F_{ei})^2}{N}} \quad (3.3)$$

where, N is the experimental data of one loop. F_e is the experimentally found force and F_p is the model-predicted force).

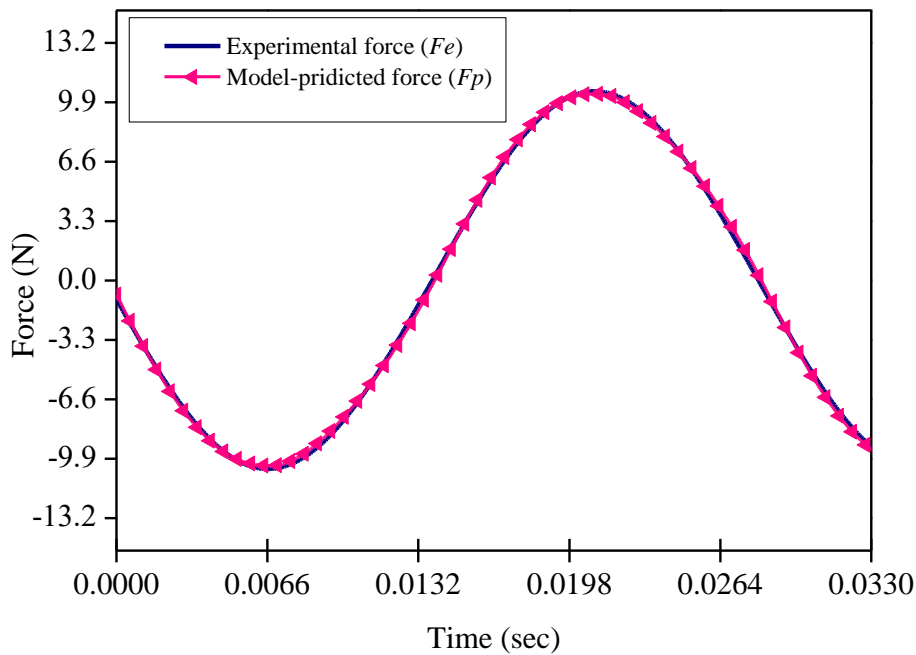


Figure 3.19 Plots of the force response of experimental and model-predicted.

All the parameters of the Bouc-Wen model are finely tuned to minimize the error between experimental data and predicted data. Figure 3.19 shows the experimental and model-predicted data of one cycle excitation of the MRE double lap shear.

3.5.2 Field-Dependent Parameters of the Bouc-Wen Model

The Bouc-Wen modeling of the MRE is done under variable frequencies of 35Hz, 40Hz and 45Hz and current of 0A, 1A, 2A and 3A for the displacements of 0.1mm. The range of the operating frequency and displacement is chosen depending on the shift frequency of MRE vibration isolation, which is discussed in Chapter 4.

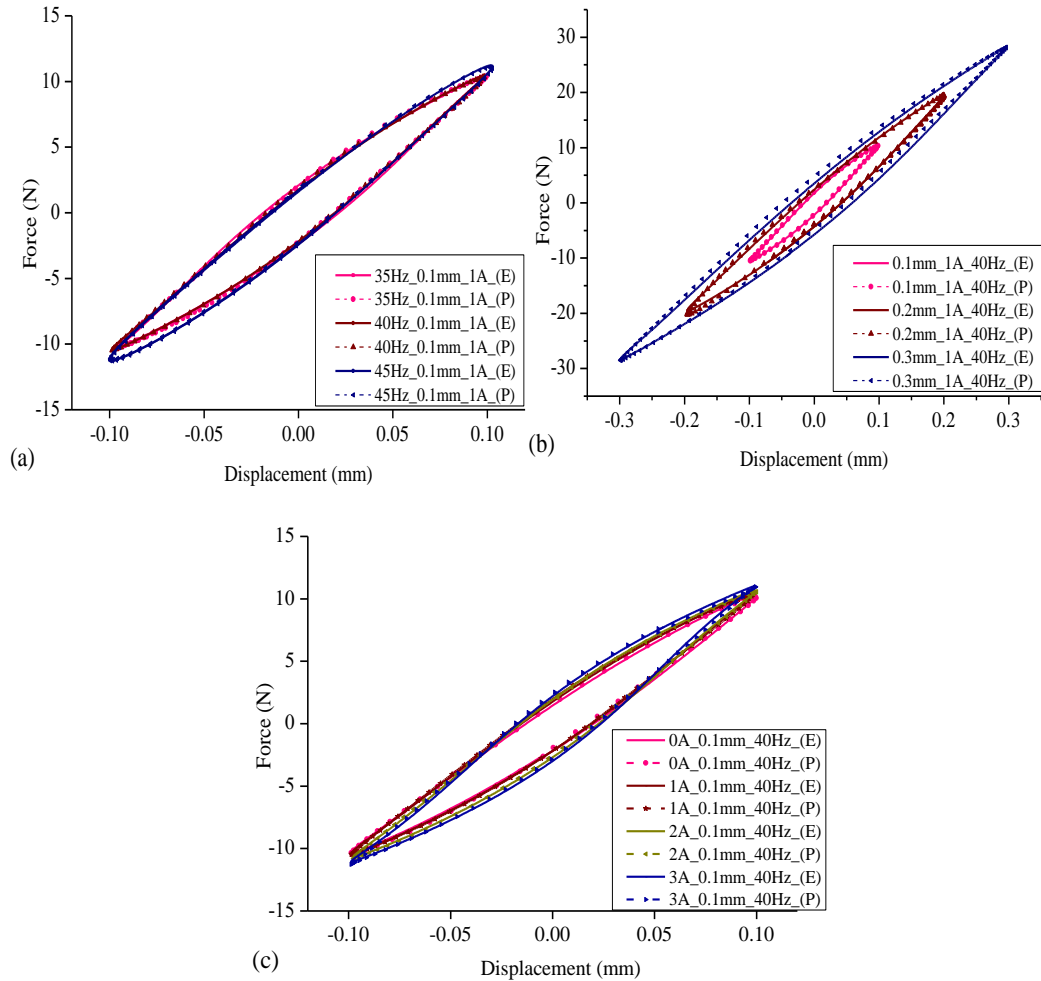


Figure 3.20 Experimental and predicted hysteresis loops: (a) variable frequency, (b) variable displacement and (c) variable current.

Figure 3.20 (a) depicts the hysteresis loop of variable frequency from 30Hz to 45 Hz at a current 1A and the displacement of 0.1mm. For the selected range of the frequencies, the slope of the hysteresis loop reveals a small rise in the stiffness with the increase in the excitation frequency. This specifies a reduced effect of the frequency of excitation on the stiffness of the MRE. Besides, the simulated figures are in good agreement with

the experimental outcomes. Figure 3. 20 (b) shows the hysteresis loop of variable displacement from 0.1mm to 0.3mm at a current of 1A and a frequency of 40Hz. An increase in input displacement increases the area of the loop and decreases the slope, indicating a reduction in stiffness and an increase in damping of MRE. The simulated hysteresis loops are in good agreement with the experiments. The hysteresis loop of variable current from 0A to 3A at a displacement of 0.1mm and a frequency of 40Hz is as shown in Figure 3.20 (c). The stiffness and damping of the MRE increase as the input current increases. The implementation of a model-based controller on the MRE intelligent devices requires an accurate field-dependent model of MRE. The Bouc-Wen model is used to estimate the same, and the parameters of the model are estimated by the parameter estimation app in Matlab/Simulink. A single hysteresis loop represents the force-displacement behavior of the MRE for input operating parameters. The operating parameters, displacement is 0.1mm, frequency is 40Hz, and currents are 0,1,2,3 A. Figure 3.20 (c) shows the predicted and experimental hysteresis loops of the MRE. The parameters of the Bouc-Wen model for different current input are presented in Table 3.1

Table 3.1 Optimal parameters under variable current.

Parameters	Variable current			
	0 A	1 A	2 A	3 A
A	-0.00389	-3.4936	-12.21	-26.67
α	12.113	10.348	10.672	12.84
β	-1.2902	3.9897	3.61	4.1054
c_0	0.006384	0.0124	0.0079	-0.0074
k_0	8.4915	2.8774	1.024	0.436
n	1	1	1	1
μ	2.1965	-3.4491	-3.57	-4.0951

The parameters for variable current are expressed (Yang et al. 2013) as

$$A = A_a + A_b I, \quad \alpha = \alpha_a + \alpha_b I, \quad c_0 = c_{0a} + c_{0b} I \quad \text{and} \quad k_0 = k_{0a} + k_{0b} I. \quad (3.4)$$

where, $A_a, \alpha_a, c_{0a}, k_{0a}$ are zero current parameters, $A_b, \alpha_b, c_{0b}, k_{0b}$ are current depends on parameters of the Bouc-Wen model and I is the input current. Table 3.2 is used to linear fit the parameters of the Bouc-Wen model, as depicted in Figure 3.21. The corresponding linear fit parameters of the Bouc-Wen model are presented in Table 3.4.

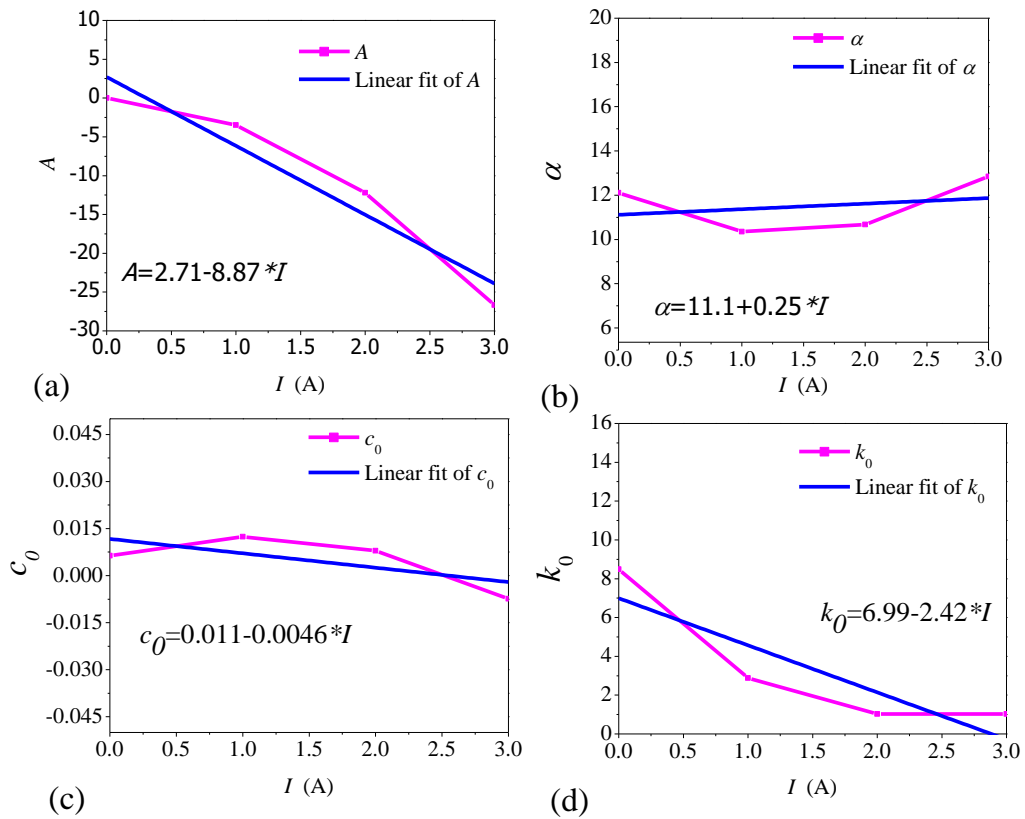


Figure 3.21 Plots of the Bouc-Wen model parameters; (a) A vs. I , (b) α vs. I , (c) c_0 vs. I and (d) k_0 vs. I .

The Bouc-Wen model accurately predicted the behavior of the MRE under the different operating conditions like input displacement, frequency and current. To simulate the model-based controllers, it is essential to model the MRE for its parameters. The values of the model parameters are presented in Table 3.3 defines the actual behavior of MRE. The input operating conditions produces the estimated force used to simulate the model-based controllers for the MRE vibration isolation.

Table 3.4 Optimal field-dependent parameters.

Parameters	Values
A_a	2.71
α_a	11.11
β	2.6
c_{0a} , (N-s/mm)	0.011
k_{0a} , (N/mm)	6.99
n	1
μ	2.22
A_b	-8.87
α_b	-0.25
c_{0b} , (N-s/mm)	-0.0046
k_{0b} , (N/mm)	-2.42

3.6 Closure

The stiffness and damping of MRE depend on the operating frequency, displacement and current/magnetic field. The dynamic stiffness of the MRE increases with an increase in current. Further, the damping of the MRE increases and the stiffness decreases with an increase in input displacement. The operating frequency has little influence on the dynamic properties of MRE. This highlights the vibration mitigation capabilities of the MRE for a wide range of operating frequencies at low input displacements. The Bouc-Wen model accurately predicts the nonlinear behavior of MRE and is further used for the simulation of the MRE vibration isolation in Chapter 4.

4. Performance of Model-based Linear Controllers on Magnetorheological Elastomer Vibration Isolation

4.1 Introduction

This chapter discusses the performance of the model-based controllers on the Magnetorheological elastomer vibration isolation. First, the fabrication of an MRE vibration isolator with anisotropic MRE has been discussed. The dynamic properties of the MRE vibration isolator are extracted from shift frequency data. Further, the model-based PID and LQR controller's implementation on MRE vibration isolation has been reported in this chapter.

4.2 Vibration Isolation

The vibration isolator reduces the undesirable vibration in machines and structures (Behrooz et al. 2014b). It consists of a spring and damper between the vibrating mass and the source of vibration through moving mass. Figure 4.1 shows the schematic of the vibration isolation.

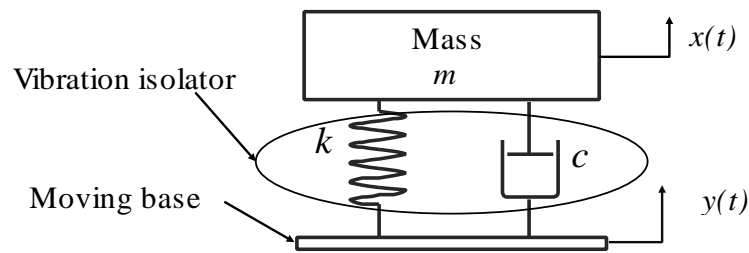


Figure 4.1 Mathematical model of vibration isolation.

The equation of motion for the vibration isolation is expressed as

$$m\ddot{x}(t) + c\dot{x}(t) + kx(t) = c\dot{y}(t) + ky(t) \quad (4.1)$$

where, m is the mass of the payload; c and k are the damping coefficient and the stiffness of the vibration isolator. $x(t)$ and $y(t)$ are the displacements of the payload and the base, respectively.

The force acting on the mass is

$$F_T = c\dot{y}(t) + ky(t) \quad (4.2)$$

The steady solution is expressed as,

$$x(t) = X \cos(\omega t - \phi) \quad (4.3)$$

Differentiating the Equation (4.3), the velocity written as

$$\dot{x}(t) = -\omega X \sin(\omega t - \phi) \quad (4.4)$$

Substituting Equations (4.3) and (4.4) in Equation (4.2), we have the force transmitted to the mass as,

$$F_T = kX \cos(\omega t - \phi) + c \omega X \sin(\omega t - \phi) \quad (4.5)$$

$$F_T = kX \cos(\omega t - \phi) + c \omega X \sin\left(\omega t - \phi + \frac{\pi}{2}\right) \quad (4.6)$$

Solving the Equation (4.6), the corresponding force transmitted is as follows

$$F_T = \sqrt{(kX)^2 + (c\omega X)^2} = X\sqrt{k^2 + c^2\omega^2} \quad (4.7)$$

Also, the amplitude of the steady-state response is expressed as,

$$X = \frac{f_0}{\sqrt{(\omega_n^2 - \omega^2)^2 + (2\xi\omega_n\omega)^2}} = \frac{F_0/k}{\sqrt{(1 - r^2)^2 + (2\xi r)^2}} \quad (4.8)$$

where, natural frequency, $\omega_n = \sqrt{k/m}$, damping ratio, $\xi = c/2m\omega_n$, force, $f_0 =$

F_0/m , frequency ratio $r = \omega/\omega_n$, and the response of mass, $x(t) = X \cos(\omega t - \phi)$

Substituting Equation (4.8) into Equation (4.7) yields

$$F_T = \frac{F_0/k}{\sqrt{(1 - r^2)^2 + (2\xi r)^2}} \sqrt{k^2 + c^2\omega^2} \quad (4.9)$$

$$F_0 = \frac{\sqrt{1 + c^2\omega^2/k^2}}{\sqrt{(1 - r^2)^2 + (2\xi r)^2}} = \frac{1 + (2\xi r)^2}{\sqrt{(1 - r^2)^2 + (2\xi r)^2}} \quad (4.10)$$

where, $c^2\omega^2/k^2 = (2m\xi\omega_n\omega)^2/k^2 = (2\xi r)^2$. The Transmissibility Ratio ($T.R$) is the ratio of the magnitude of the transmitted force to the magnitude of the applied force (J.Inman 2011) is written as,

$$T R = \frac{F_T}{F_0} = \sqrt{\frac{1 + (2\xi r)^2}{\sqrt{(1 - r^2)^2 + (2\xi r)^2}}} \quad (4.11)$$

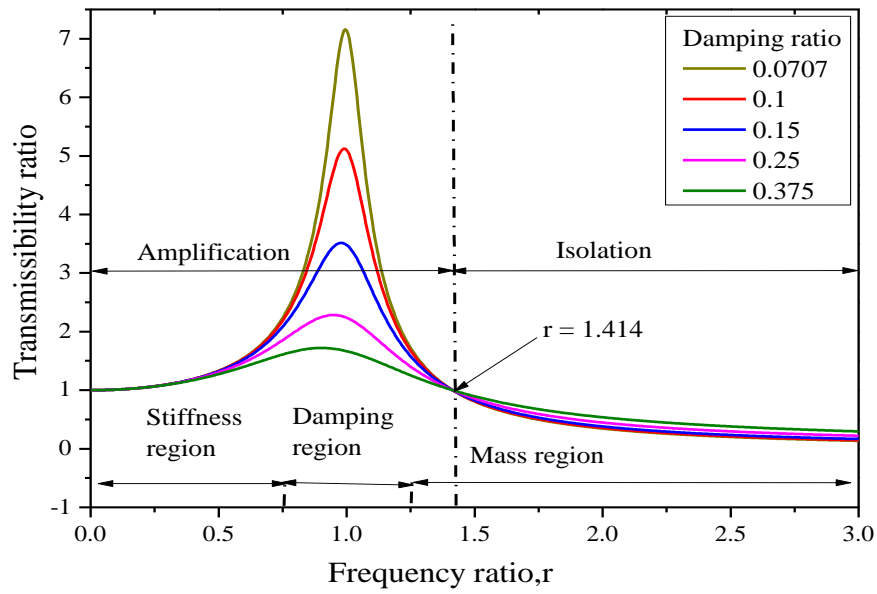


Figure 4.2 Plots of frequency ratio vs. transmissibility ratio.

Figure 4.2. illustrates the frequency ratio vs. transmissibility ratio vibration isolation for the varying values of the damping ratio. The frequency ratio is mainly divided into amplification and isolation regions. In the amplification region, the transmissibility ratio is higher compared to that of the isolation region. The transmissibility ratio in the amplification region can be controlled by varying the stiffness and damping of the system, making it stiffness and damping controlled region. In this work, MRE-based semi-active isolation is considered, whose stiffness and damping can be varied by changing the magnetic field. The amplification region is considered due to the variable properties of MRE to control the vibration and the following section discusses real-time implantation of MRE vibration isolation.

4.3 Magnetorheological Elastomer Vibration Isolation

4.3.1 Fabrication of MRE Vibration Isolator

Figure 4.3. illustrates the in-house fabricated MRE vibration isolator. It consists of a mass, MRE and electromagnet. Two MRE samples of size, $25 \times 25 \times 3$ mm thick, and are glued between the electromagnet and the stinger on either side. The MRE isolators are subjected to double lap shear mode. The isolator has an end mass of 0.61 kg. The electromagnet is constructed with 2400 turns of AWG18. A magnetic field of 0.66 T is attained at a maximum current of 5 A to the electromagnet.

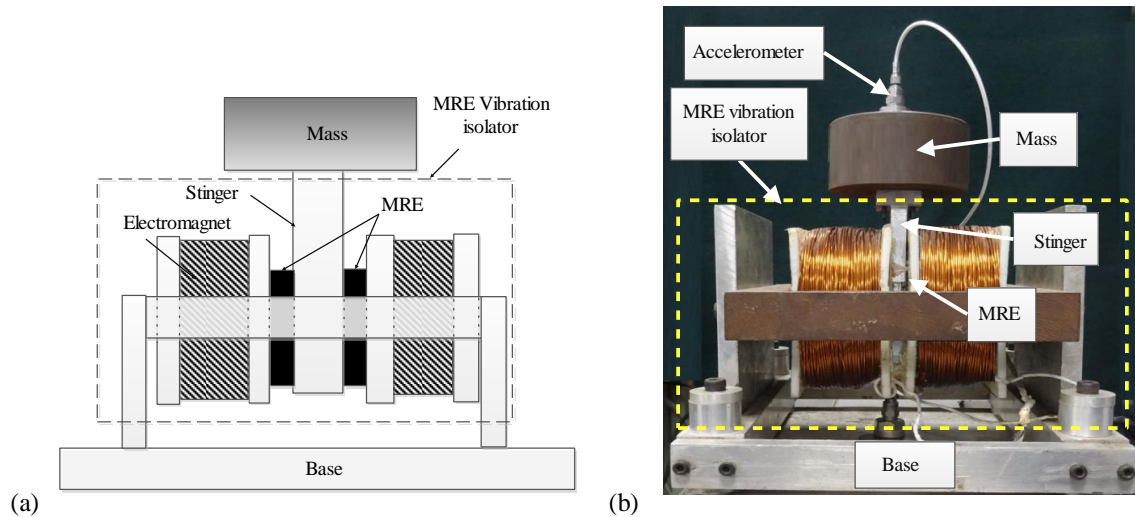


Figure 4.3 MRE vibration isolator: (a) schematic and (b) photograph.

4.3.2 The Frequency Shift of MRE Vibration Isolator

The MRE vibration isolator is subjected to sweep excitation from 5 Hz to 90 Hz, as shown in Figure 4.4. Figure 4.5 (a) and (b) depict the measured frequency response function and phase angle for variable current. The natural frequency of the MRE vibration isolator increases from 39 Hz to 43 Hz for the current of 0 A to 2.5 A. The shift in the natural frequency is credited to the magnetic field-induced increase in the MRE stiffness. The magnetic field forces the carbonyl iron particles to align in the direction of magnetic flux. This results in the development of magnetic dipoles among the adjacent particles, which induces compressive forces on the rubber matrix. These compressive forces lead to an increase in the overall stiffness of MRE (Poojary and Gangadharan 2017). Furthermore, the damping coefficient's increase is attributed to the

rise in the interfacial sliding friction between the iron particles and the bound rubber (Yang et al., 2012b). Table 4.1 presents the dynamic properties of the MRE vibration isolator.

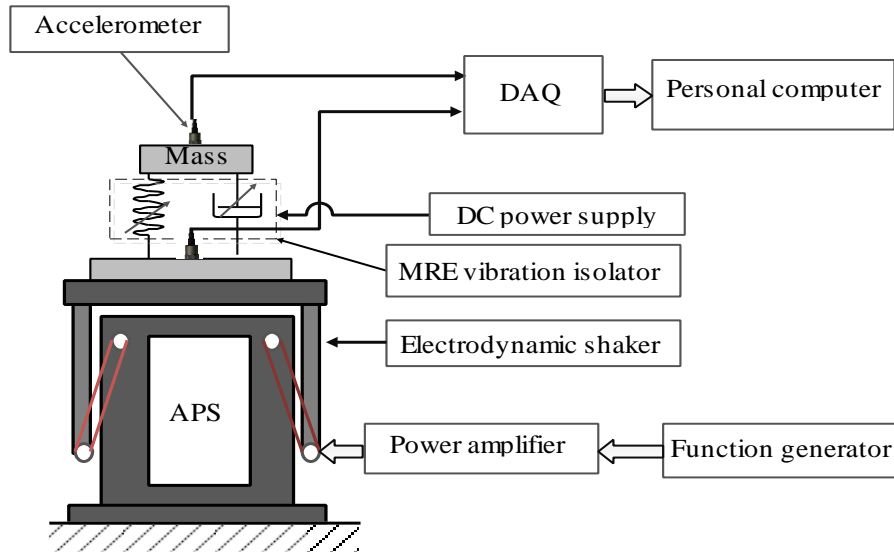


Figure 4.4 Schematic of MRE vibration isolation.

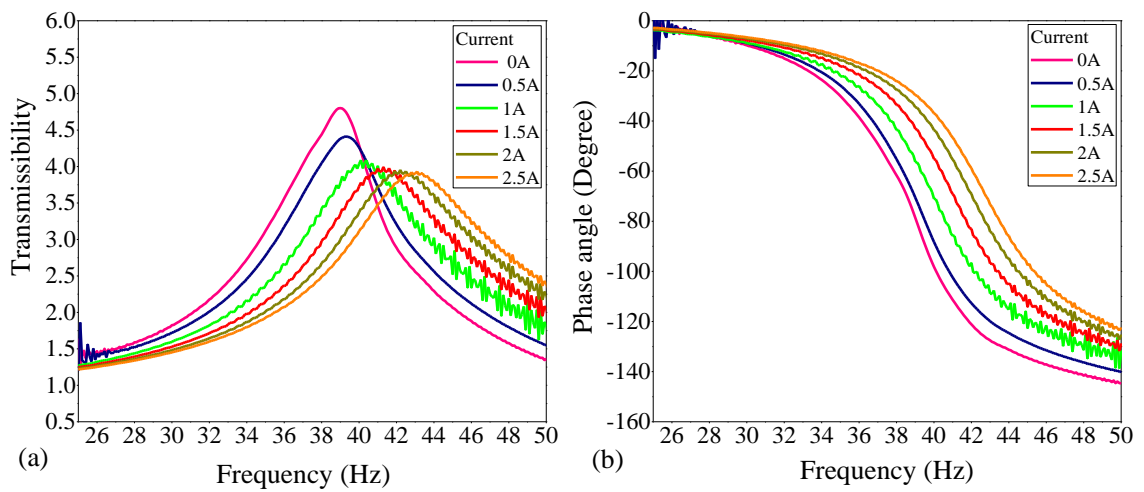


Figure 4.5 Plots of (a) Transmissibility vs. frequency and (b) phase angle vs. frequency.

Table 4.1 Measured dynamic properties of the MRE vibration isolator under the variable current

Current (A)	Voltage (V)	Magnetic Field (T)	Frequency (Hz)	Stiffness (kN/m)	Damping Coefficient (N-s/m)	Damping factor
0	0	0	39	36.63	31.68	0.106
0.5	5.32	0.073	39.5	37.57	35.12	0.116
1	10.64	0.150	40.5	39.50	40.04	0.129
1.5	15.96	0.210	41.5	41.47	42.30	0.133
2	21.23	0.315	42.5	43.49	43.65	0.134
2.5	26.6	0.331	43	44.52	44.16	0.134

4.4 System Dynamics of MRE Vibration Isolation

The simulation and real-time implementation of controllers need a thorough knowledge of the dynamics of the system. The present section discusses the MRE vibration isolation, the state-space equation of MRE vibration isolation and model-based linear controllers.

4.4.1 Vibration Isolation with Control Input

Vibration isolation is considered as a two-degree freedom system to derive the state-space equation, as shown in Figure 4.6.

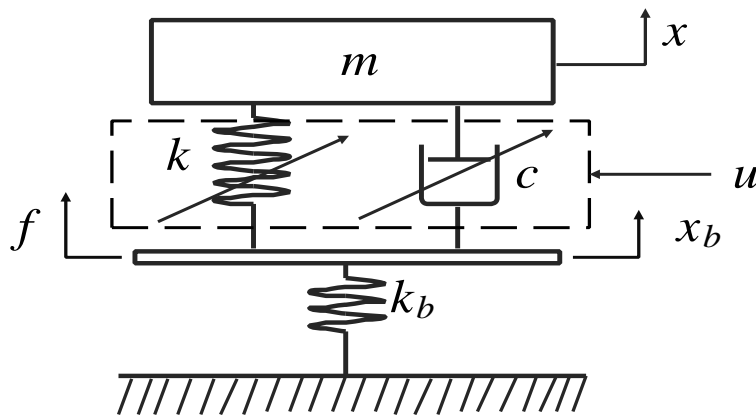


Figure 4.6 Schematic of MRE vibration isolation with control input.

The governing differential equation of MRE vibration isolation is written as,

$$m_b \ddot{x}_b + k_b x_b + k(x_b - x) = f(t) + u \quad (4.12)$$

$$m\ddot{x} + k(x - x_b) + c(\dot{x} - \dot{x}_b) = -u \quad (4.13)$$

where m , k and c are the mass, stiffness and damping coefficient, respectively, of the MRE vibration isolator. m_b and k_b are the mass and stiffness of the base, respectively. x , \dot{x} and \ddot{x} are the displacement, velocity and acceleration of the mass, respectively. x_b , \dot{x}_b and \ddot{x}_b are the displacement, velocity and acceleration of the base, respectively. u is the control input and $f(t)$ is the input excitation.

4.4.2 State-Space Equation of MRE Vibration Isolation

The simulation of the controllers requires the dynamics of the MRE vibration isolation. Equations (4.12) and (4.13) defines the dynamic of the MRE vibration isolation. The state-space equation is a matrix system of these equation written in the form of the state vector $\dot{x}(t)$ and $y(t)$. These state space equations are utilized for the simulation of the MRE vibration isolation with controllers in MATLAB/SIMULINK in Chapters 4 and 5. The state-space equation (Nise 2011) of MRE vibration isolation is expressed as

$$\dot{x}(t) = Ax(t) + Bu(t) \quad (4.14)$$

$$y(t) = Cx(t) + Du(t) \quad (4.15)$$

where, x is the state vector, y is the output vector, u is the control input, A is the system matrix, B is the input matrix, C is the output matrix and D is the feedforward matrix. The dot indicates the first derivative of time, t . These vectors and matrices are of form;

$$\dot{x} = \begin{bmatrix} \dot{x}_b \\ \dot{x} \\ \ddot{x}_b \\ \ddot{x} \end{bmatrix}, x = \begin{bmatrix} x_b \\ x \\ \dot{x}_b \\ \dot{x} \end{bmatrix}, u = \begin{bmatrix} f \\ u \end{bmatrix}, A = \begin{bmatrix} 0 & 0 & 1 & 0 \\ 0 & 0 & 0 & 1 \\ -\frac{(k+k_b)}{m_b} & \frac{k}{m_b} & 0 & 0 \\ \frac{k}{m} & -\frac{k}{m} & \frac{c}{m} & -\frac{c}{m} \end{bmatrix},$$

$$B = \begin{bmatrix} 0 & 0 \\ 0 & 0 \\ \frac{1}{m_b} & \frac{1}{m} \\ 0 & -\frac{1}{m} \end{bmatrix}, \quad C = \begin{bmatrix} 1 & 0 & 0 & 0 \\ 0 & 1 & 0 & 0 \\ 0 & 0 & 1 & 0 \\ 0 & 0 & 0 & 1 \end{bmatrix} \text{ and } D = \begin{bmatrix} 0 & 0 \\ 0 & 0 \end{bmatrix}.$$

4.5 Linear Controllers

Real-time implementation of MRE vibration isolation requires the input current and the controllers to regulate the electromagnet's current. The following sections discuss the implementation of model-based linear controllers on MRE vibration isolation.

4.5.1 Proportional Integral Derivative Controller

A proportional integral derivative (PID) controller is the simplest and yet very effective method to regulate systems input. Because of its feature, it is the standard technique for industrial applications (Vijay and Jena 2017). In the present work, the PID controller has been used for the control of MRE vibration isolation. Vibration isolation consists of the MRE and electromagnet. PID-controlled current is supplied to the electromagnet. The electromagnet eventually varies the magnetic field resulting in the required variation in the dynamic stiffness and damping properties of the MRE vibration isolator. The schematic of the PID controller is shown in Figure 4.7, and the input of PID control is expressed as

$$u(t) = K_p e(t) + K_i \int e(t) dt + K_d \frac{d}{dt} e(t) \quad (4.16)$$

where $u(t)$ is the control input, e is the signal error defined as $e = (x_d - x)$. x_d and x are the desired and actual displacements, respectively. K_p , K_i and K_d are the proportional, integral and derivative gains of the PID controller, respectively.

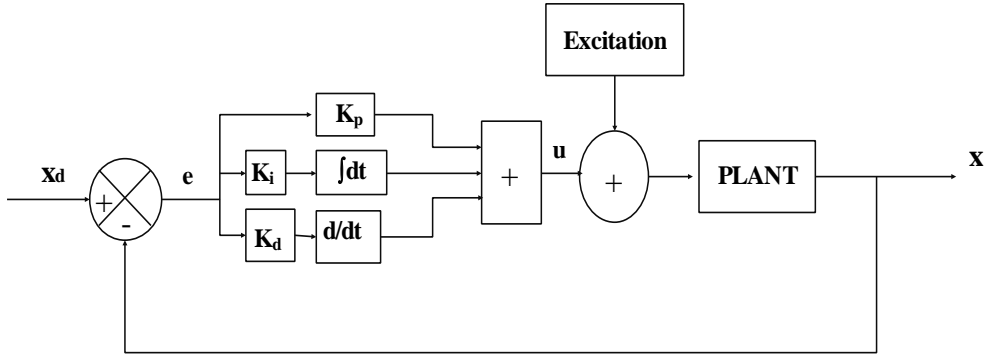


Figure 4.7 Schematic of PID controller.

4.5.2 Linear Quadratic Regulator Controller

Linear quadratic regulator (LQR) is an optimal controller that uses a cost minimization function to optimize the effort required by the controller (Luiz et al., 2013). The input of the LQR controller is expressed (Luiz et al. 2013) as

$$u(t) = -Kx(t) \quad (4.17)$$

where, K is the feedback gain-matrix. To find the control signal, u that minimizes the cost function, the performance index is defined by

$$J = \int_0^{\infty} (x^T Qx + u^T Ru) dt \quad (4.18)$$

where, Q is the semi-positive diagonal matrix that weights x and R is the positive matrix that weights the control effort, u . The feedback gain matrix, K is obtained by

$$K = R^{-1}BP \quad (4.19)$$

where, P is the solution of algebraic Riccati equation defined by

$$ATP + PA + Q - PBR^{-1}BTP \quad (4.20)$$

The Linear quadratic regulator (LQR) is the state-feedback of the controller. It requires all the states of the system that to be controlled. If all the states are not known physically, unknown states or full states can be estimated using a state estimator or observer. Figure 4.8 shows the schematic of the LQR controller with the observer.

Equations (4.14) and (4.15) defines the actual system.

The observer is modeled (Nise 2011) as,

$$\dot{\hat{x}}(t) = A\hat{x}(t) + Bu(t) + L(y(t) - \hat{y}(t)) \quad (4.21)$$

$$\hat{y}(t) = C\hat{x}(t) + Du(t) \quad (4.22)$$

where, L is the gain matrix of the observer.

Substitution of Equation (4.22) in (4.21) yields

$$\dot{\hat{x}}(t) = A\hat{x}(t) + Bu(t) + L(y(t) - C\hat{x}(t) + Du(t)) \quad (4.23)$$

$$\dot{\hat{x}}(t) = (A - LC)\hat{x}(t) + (B - LD)u(t) + Ly(t) \quad (4.24)$$

The objective of the observer is to estimate the exact state, $x(t)$, of any system. The estimated error, $e(t) = (x(t) - \hat{x}(t))$ must lead to zero as $t \rightarrow \infty$.

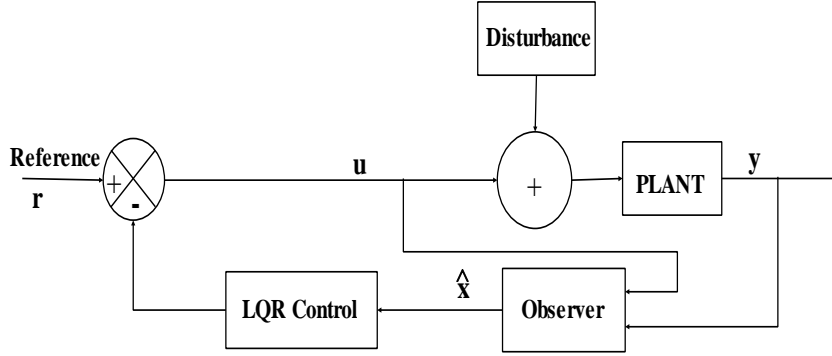


Figure 4.8 Schematic of LQR controller with the observer.

The estimation error is defined as

$$e(t) = x(t) - \hat{x}(t) \quad (4.25)$$

$$\dot{e}(t) = Ax(t) + Bu(t) - [(A - LC)\hat{x}(t) + (B - LD)u(t) + Ly(t)] \quad (4.26)$$

$$\dot{e}(t) = (A - LC)x(t) - (A - LC)\hat{x}(t) \quad (4.27)$$

$$\dot{e}(t) = (A - LC)e(t) \quad (4.28)$$

The state equation of the estimation error is the homogeneous differential equation governed by $(A - LC)$. The L matrix should be chosen in such a way that the eigenvalues of $(A - LC)$ must fall left-half of the complex plane for asymptotically stability, i.e., $e(t) \rightarrow 0$ as $t \rightarrow \infty$.

4.5.3 Model-based PID and LQR Controllers

Equations (4.16) and (4.17) are considered for implementing the Bouc-Wen model-based PID and LQR controllers. The design controllers are combined with the

Bouc-Wen model through the clipped control algorithm, as shown in Figure 4.9. The rules for the clipping force signal is expressed (Dyke 1996) as,

$$v = v_{max} H[(F_D - F)F] \quad (4.29)$$

where v is the voltage, v_{max} is the maximum voltage, H is the Heaviside function (Dyke 1996), F_D is the desired optimal control force and F is the force of the model. From Equation (4.15), the control voltage (Luiz et al. 2013) is written as,

$$v = \begin{cases} v_{max}, & F_D > F \\ 0, & F_D \leq F \end{cases} \quad (4.30)$$

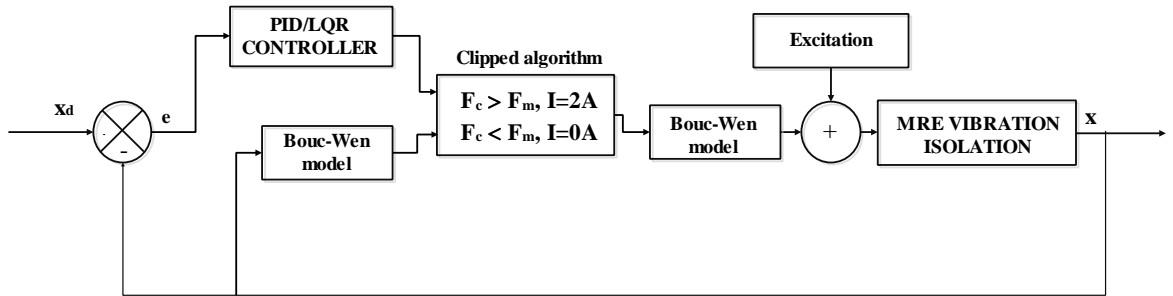


Figure 4.9. Schematic model-based controllers with MRE vibration isolation.

4.6 Simulation Analysis

The simulation of the proposed controller for MRE vibration isolation under single frequency excitation is executed in MATLAB/Simulink. The parameters of the MRE vibration isolation are considered for simulation study are mass, $m = 0.61\text{kg}$, stiffness, $k = 36.63\text{ kN/m}$ and damping coefficient, $c = 31.68\text{N-s/m}$. Both the PID and LQR controllers are simulated for single-frequency excitation. Bouc-Wen model-based PID and LQR with the clipped control algorithm are used for the simulation. The condition for the control current is expressed as

$$I = \begin{cases} 2\text{ A}, & F_C > F_M \\ 0\text{ A}, & F_C \leq F_M \end{cases} \quad (4.31)$$

where I is the control current, F_C is the force generated by PID or LQR, and F_M is the force generated by the Bouc-Wen model.

4.7 Results and Discussion

4.7.1 Single-Frequency Excitation with Model-based PID Controller

The steady-state excitation is carried out for the operating frequency from 34Hz to 40Hz in steps of 2 Hz to simulate the MRE vibration isolation with the PID controller. The Simulink program of the model-based PID controller is shown in Figure 4.10.

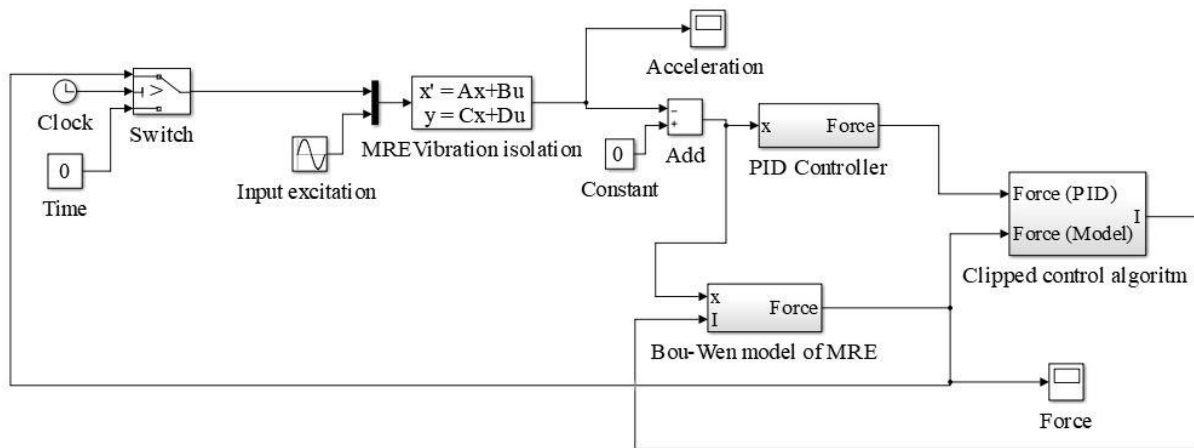


Figure 4.10 Simulink program of model-based PID controller.

The time response of all the simulated frequencies is depicted in Figure 4.11 to Figure 4.14. Figure 4.11 (a) shows the response of the PID controller at the excitation frequency of 34Hz. The simulation time of 10 s is divided into control-off and control-on, wherein the acceleration value for control-off is 27.46 m/s^2 . With control-on, the acceleration reduces to 18.06 m/s^2 . Hence, the control force of 7.35N, as shown in Figure 4.11 (b). The control-on state is divided into two parts, i.e., the transient response and the steady-state response. The transient response is less than 0.4 s, and after that, it attains the steady-state condition making it a stable controller. From Table 4.2, it is observed that the maximum reduction of the acceleration is 34.23% at the excitation frequency of 34Hz, and a similar response is observed for other simulated frequencies.

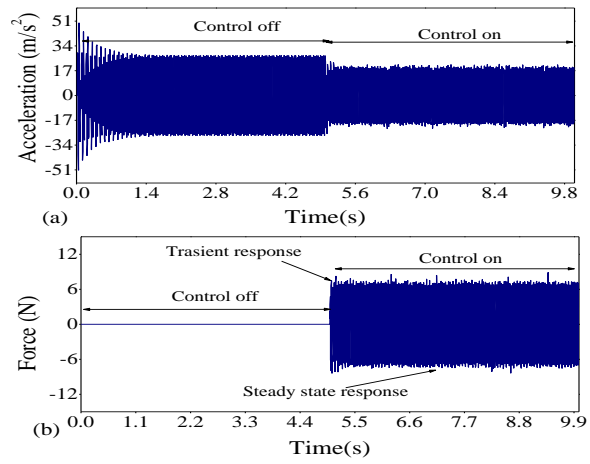


Figure 4.11 Simulated responses at 34Hz: (a) acceleration and (b) force.

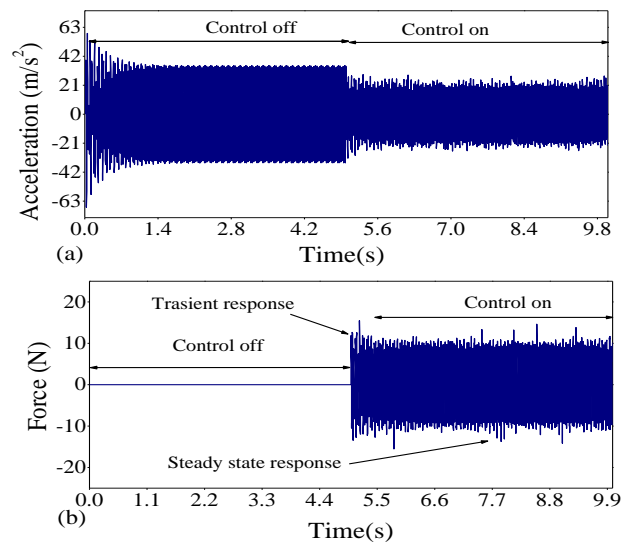


Figure 4.12 Simulated responses at 36Hz: (a) acceleration and (b) force.

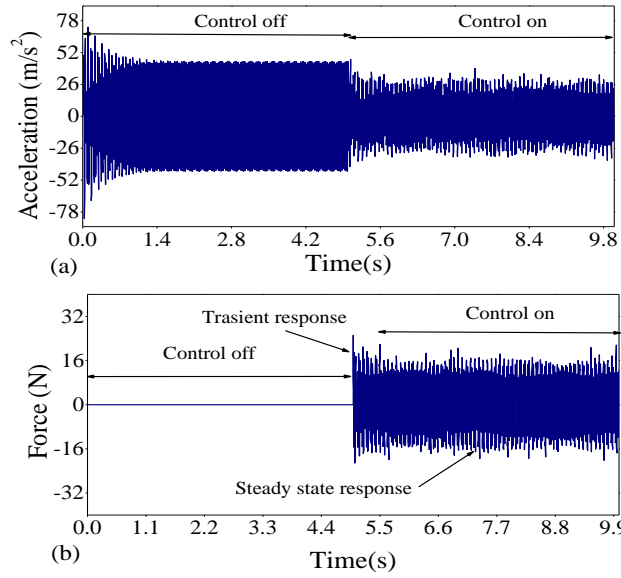


Figure 4.13 Simulated responses at 38Hz: (a) acceleration and (b) force.

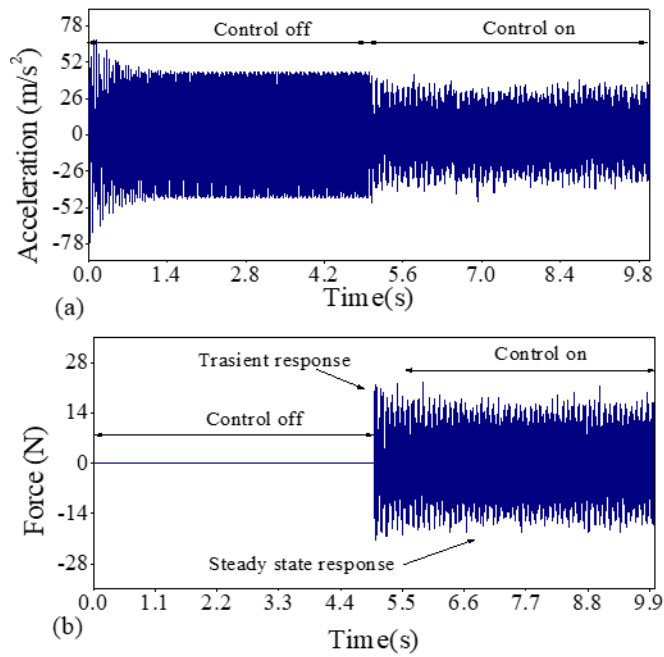


Figure 4.14 Simulated responses at 40Hz: (a) acceleration and (b) force.

Table 4.2 Simulated results of MRE vibration isolation with model-based PID controller.

Frequency (Hz)	$\ddot{x}(\text{m/s}^2)$		% of decrease	Force (N)	PID gain		
	Control off	Control on			K_p	K_i	K_d
34	27.46	18.06	34.23161	7.35	12	0.35	0.41
36	35.31	25.89	26.67799	10.65	18	0.46	0.6
38	44.55	29.89	32.90685	16.17	15	0.31	0.31
40	45.32	39.35	13.17299	17.51	16	0.25	0.31

4.7.2 Single-Frequency Excitation with Model-based LQR Controller

MRE vibration isolation is subjected to a steady-state excitation from 34Hz to 40Hz in steps of 2Hz. The Simulink program of the model-based LQR controller is shown in Figure 4.15.

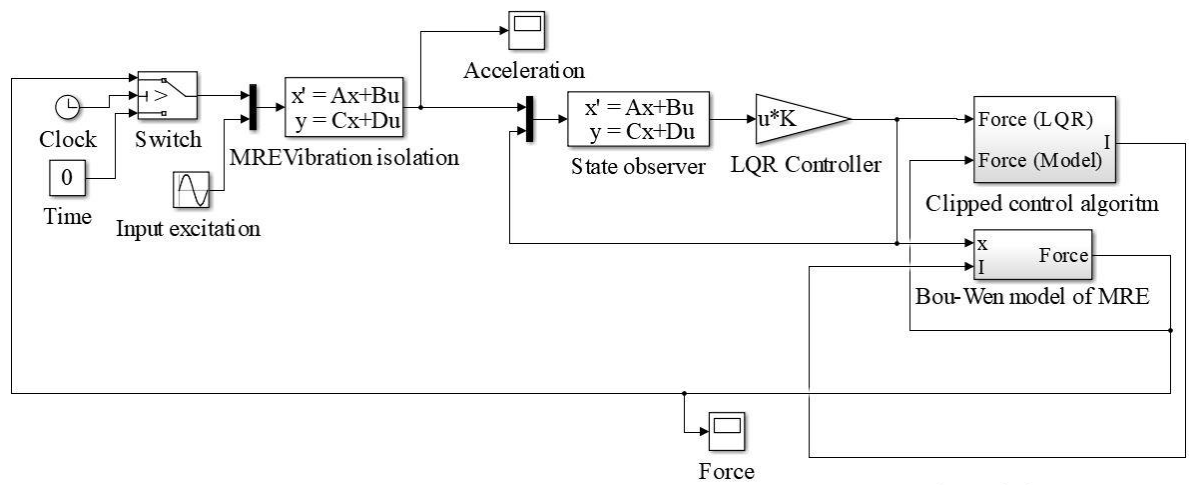


Figure 4.15 Simulink program of model-based LQR controller.

The simulated time response for all the frequencies considered in this study is depicted in Figure 4.16 to Figure 4.19. Figure 4.16(a) shows the time response of the LQR controller at an excitation frequency of 34Hz. The simulation time is divided as control-off and control-on, wherein the first 3 s the acceleration is 27.52m/s^2 . With control-on, the acceleration reduces to 20.02 m/s^2 and the control force of 7.44 N, as shown in Figure 4.16 (b). Thus, the control takes less than 0.3 s to reach a steady-state response.

From Table 4.3, it is observed that the maximum reduction of the acceleration is 26.52% at the excitation frequency of 34Hz, and a similar response is observed for other simulated frequencies. This shows the effectiveness of the controller in vibration control.

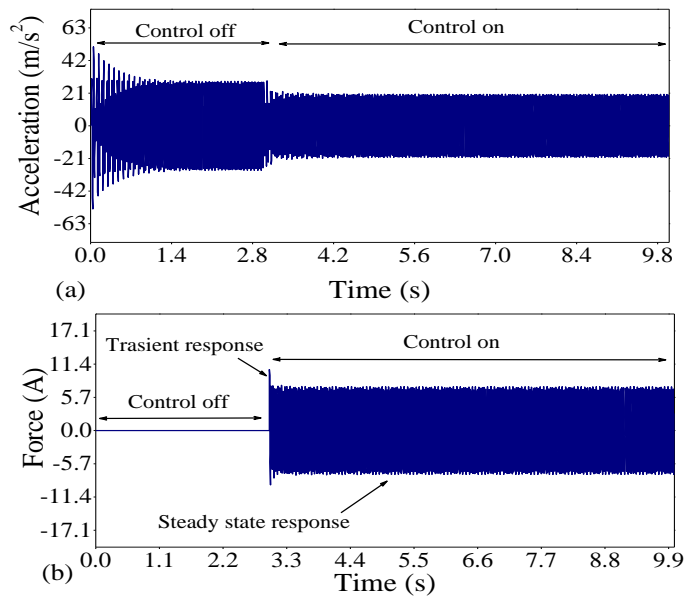


Figure 4.16 Simulated responses at 34Hz: (a) acceleration and (b) force.

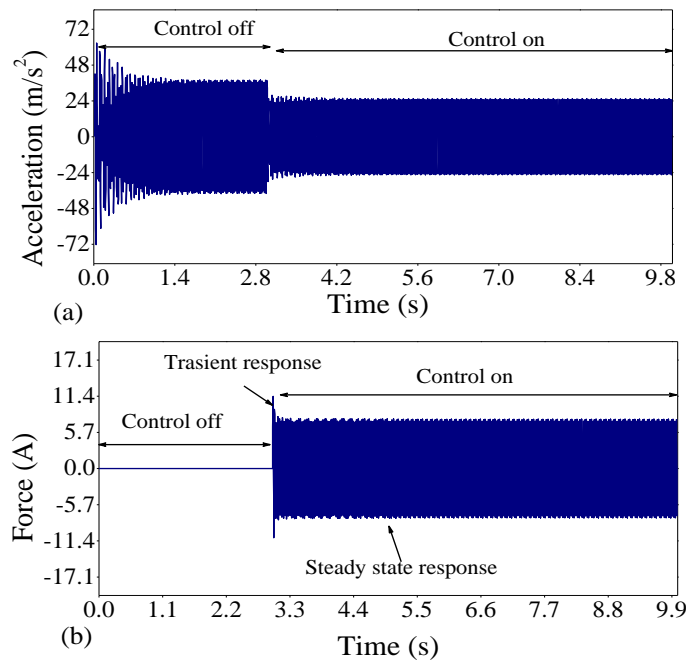


Figure 4.17 Simulated responses at 36 Hz: (a) acceleration and (b) force.

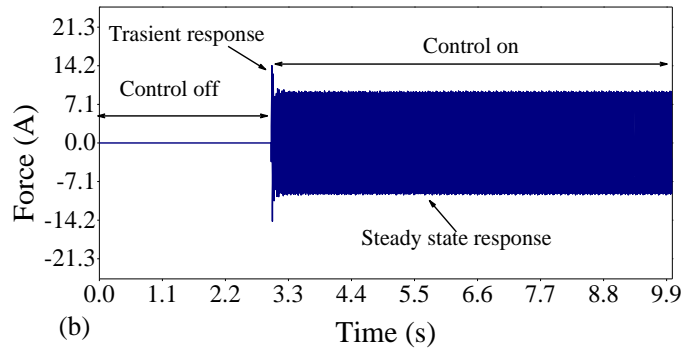
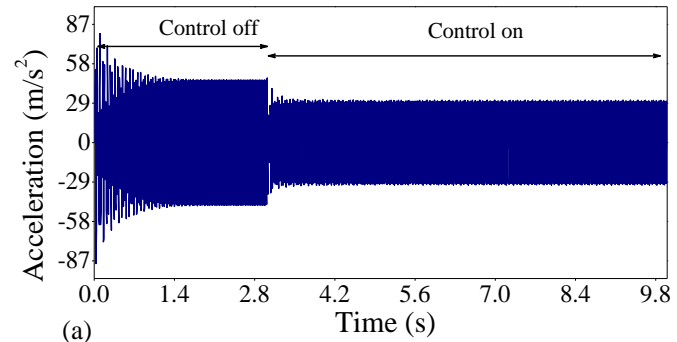


Figure 4.18 Simulated responses at 38Hz: (a) acceleration and (b) force.

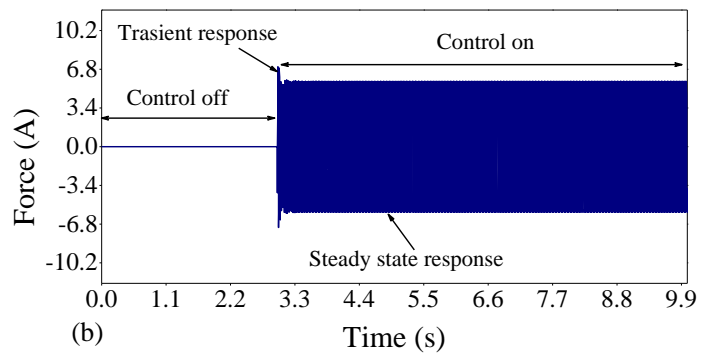
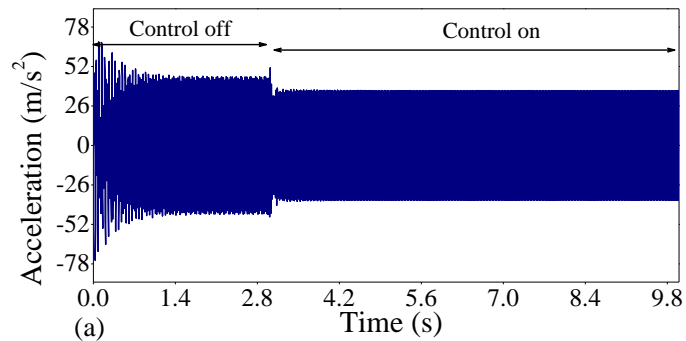


Figure 4.19 Simulated responses at 40 Hz: (a) acceleration and (b) force.

Table 4.3 Results of MRE vibration isolation with model-based LQR controller under different excitation frequencies.

Frequency (Hz)	LQR simulation				LQR Experimental			
	\ddot{x} (m/s ²)	\ddot{x} (m/s ²)	% of	Force	\ddot{x} (m/s ²)	\ddot{x} (m/s ²)	% of	Current
	Control off	Control on	decrease	(N)	Control off	Control on	decrease	(A)
34	27.52	20.22	26.52	7.44	28.57	20.01	29.96	1.93
36	38.23	24.85	34.99	7.78	36.73	25.05	31.79	1.88
38	45.74	29.92	34.58	9.51	47.41	30.37	35.94	1.89
40	43.15	36.12	16.29	5.49	48.66	37.11	23.73	1.91

4.8 Experimental Setup for the Real-Time Controller of MRE Vibration Isolation

Figure 4.20 illustrates the schematic of the experimental setup of a real-time controller for the MRE vibration isolation. The proposed PID and LQR controllers are deployed on the Compact RIO Real-time controller (Make National Instruments; Type cRIO-9022). The input module (NI-9234) and output module (NI-9264) are mounted on the Compact RIO.

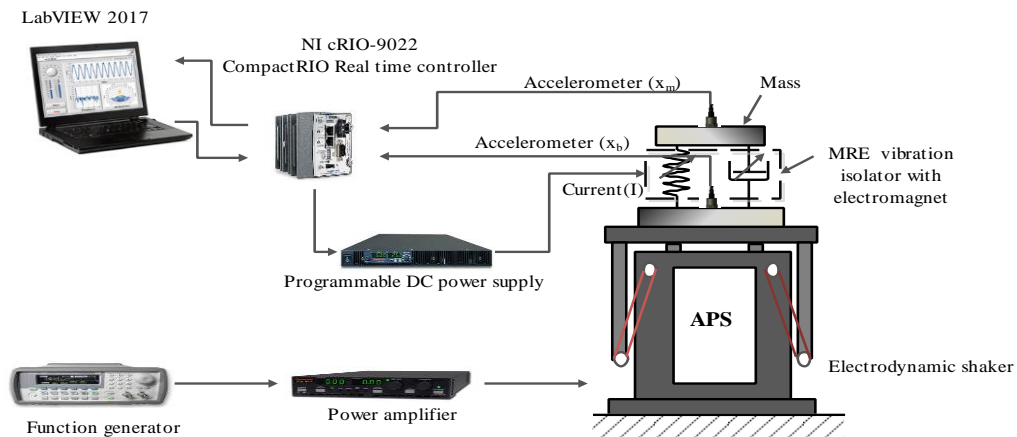


Figure 4.20 Schematic of the experimental set-up of the Real-time controller.

The Electrodynamic shaker (*APS 420 ELECTRO-SEIS*) is used to excite the MRE vibration isolation. The output acceleration signals are acquired with an input module and processed in the LabVIEW RT platform. A voltage output module controls the

electromagnet's input via a DC power supply (AMETEK, XG150-5.6, Programmable power supply). Figure 4.21 depicts the photograph of the experimental setup.

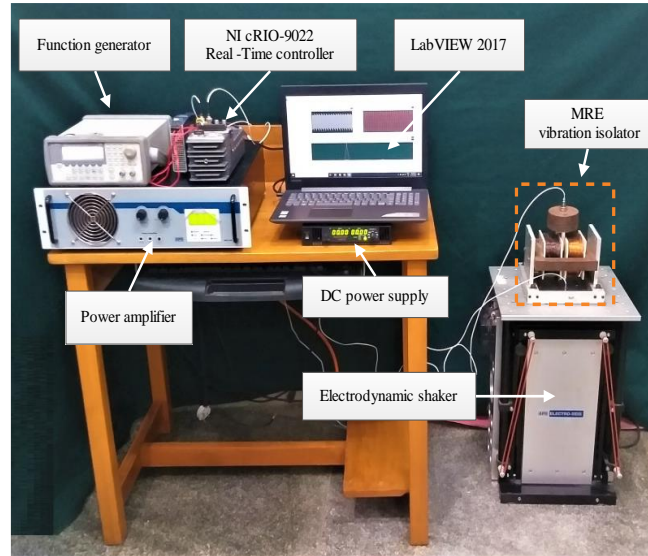


Figure 4.21 Photograph of the experimental setup of the Real-time controller.

4.9 Results and Discussion

The proposed PID and LQR controllers are investigated experimentally under single frequency excitation. The optimal gains obtained from simulation are used with little modification for the experimental analysis. The following sections discuss the same.

4.9.1 The Experiment of Single-Frequency Excitation with PID Controller

The experimental analysis of the MRE vibration isolation is carried out for the same frequencies, as discussed in the simulation of the PID controller.

Figure 4.22 shows the LabVIEW program of real-time implementation of the PID controller on MRE vibration isolation. The time response of the excitation from 34Hz to 40Hz is obtained in steps of 2Hz with the shaker excited for 10 s. In the first 5 s (with control-off), the measured acceleration is 27.37 m/s^2 . When control-on, the acceleration reduces to 19.73 m/s^2 and the control current is 1.98 A, as shown in Figure 4.23(b). Thus, the controller achieves a steady-state response in less than 0.5 s. In addition, it is observed that the derivative and integral gains of the PID controller accurately and rapidly reduces the vibration amplitude of the MRE vibration isolation.

From Table 4.4. It is evident that the maximum reduction of the acceleration is 27.7% at the excitation frequency of 34Hz, and similar behavior is observed for other frequencies depicted in Figure 4.23 to Figure 4.26. This is because PID controller requires only one state of the system (i.e., displacement) for effective reduction of vibration amplitude of the MRE vibration isolation. However, LQR is a full state feedback controller that requires all the states of the system and needs to develop the state estimator to estimate the system's states.

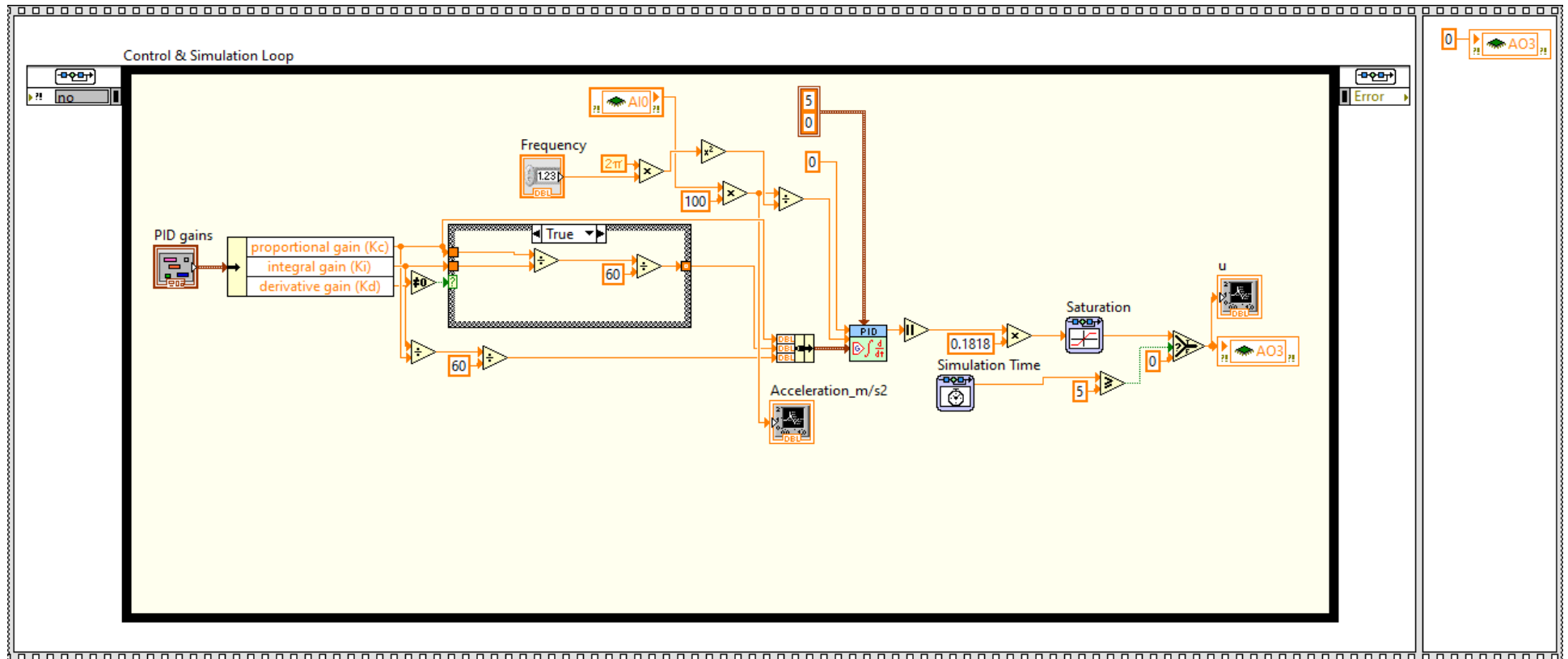


Figure 4.22. LabVIEW program of PID controller.

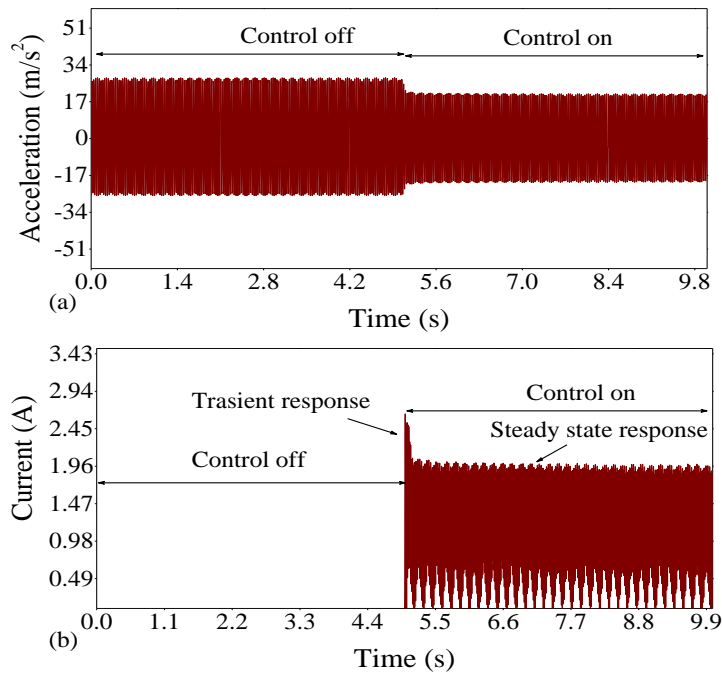


Figure 4.23 Measured responses at 34Hz: (a) acceleration and (b) control current.

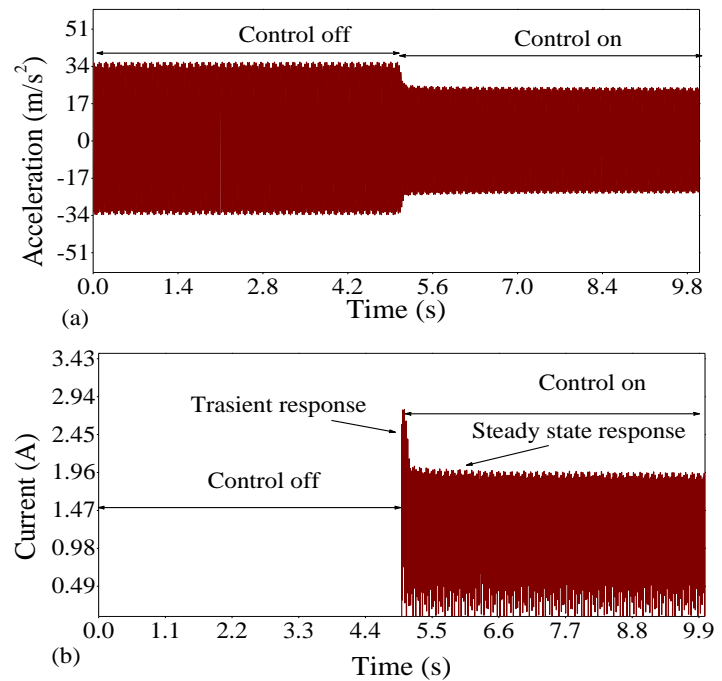


Figure 4.24 Measured responses at 36Hz: (a) acceleration and (b) control current.

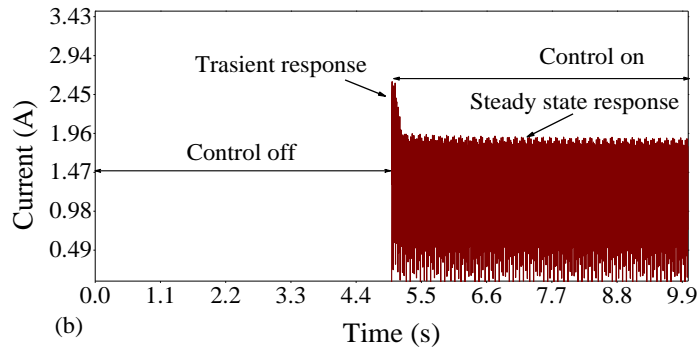
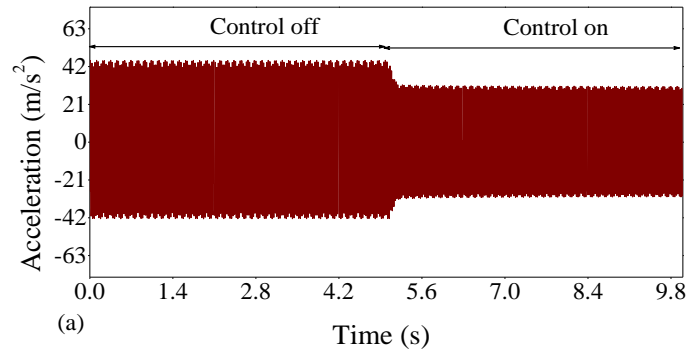


Figure 4.25 Measured responses at 38Hz: (a) acceleration and (b) control current.

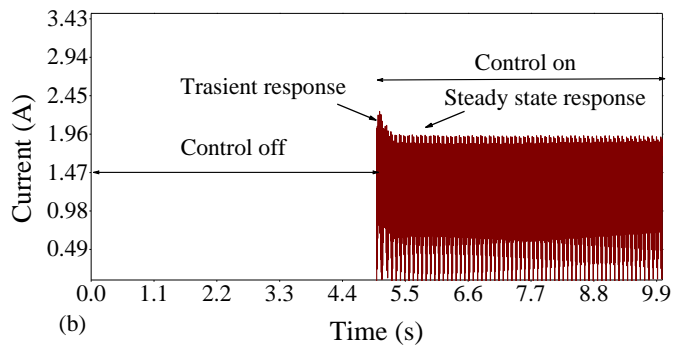
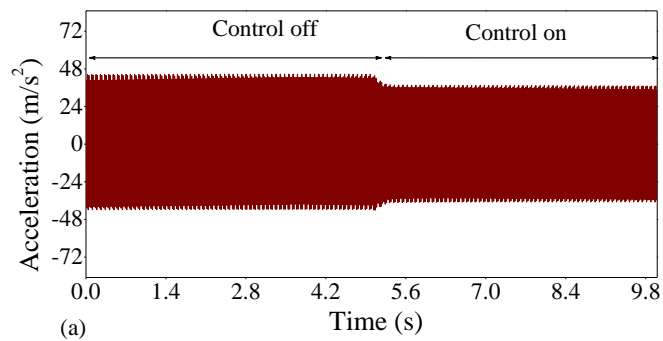


Figure 4.26 Measured responses at 40Hz: (a) acceleration and (b) control current.

Table 4.4 Experimental results of MRE vibration isolation with PID control.

Frequency (Hz)					PID gain		
	\ddot{x} (m/s ²) Control off	\ddot{x} (m/s ²) Control on	% of decrease	Current (A)	K_p	K_i	K_d
34	27.37	19.73	27.91	1.98	10	0.42	0.41
36	35.87	24.46	31.80	1.94	15	0.34	0.32
38	44.53	31.05	30.27	1.91	15	0.26	0.26
40	44.66	36.29	18.74	1.92	15	0.22	0.21

4.9.2 The Experiment of Single-Frequency Excitation with LQR Controller

The LabVIEW program of real-time implementation of the LQR controller for the MRE vibration isolator is shown in Figure 4.27. The gains of Figure 4.28 to Figure 4.31 show the measured time response of the excitation frequency from 34Hz to 40Hz in steps of 2Hz. The gain vectors and matrices of the observer and LQR controller for 34Hz are defined by $L = [47 \ -48 \ 37196 \ 40461]^T$ and $Q = [600000 \ 0 \ 0 \ 0; 0 \ 900 \ 0 \ 0; 0 \ 0 \ 90 \ 0; 0 \ 0 \ 0 \ 10]$, $R = [0.045]$ and $K = [679.8 \ 1201.4 \ -21.7 \ 2.6]^T$. For the other frequencies of excitation, the gain matrixes are obtained similarly in MATLAB. The MRE vibration isolation was subjected to excitation of 10 s with control off and control on. In the first 5 s, the measured acceleration amplitude is 28.57 m/s². With the control-on, the acceleration reduces to 20.01 m/s² for a control current of 1.93A, as shown in Figure 4.28. The controller attains a steady-state response in less than 0.3 s. The LQR controller is a full state feedback controller that requires all the states of the system. In this study, the state estimator is developed to estimate the states of the system. Due to the estimation error of the states, there will be an error between actual states and estimated states which affects the performance of the controller. From Table 4.5, it is observed that the maximum reduction of the measured acceleration is 29.96% at the excitation frequency of 34Hz. Similar behavior is observed for all other frequencies considered in this study.

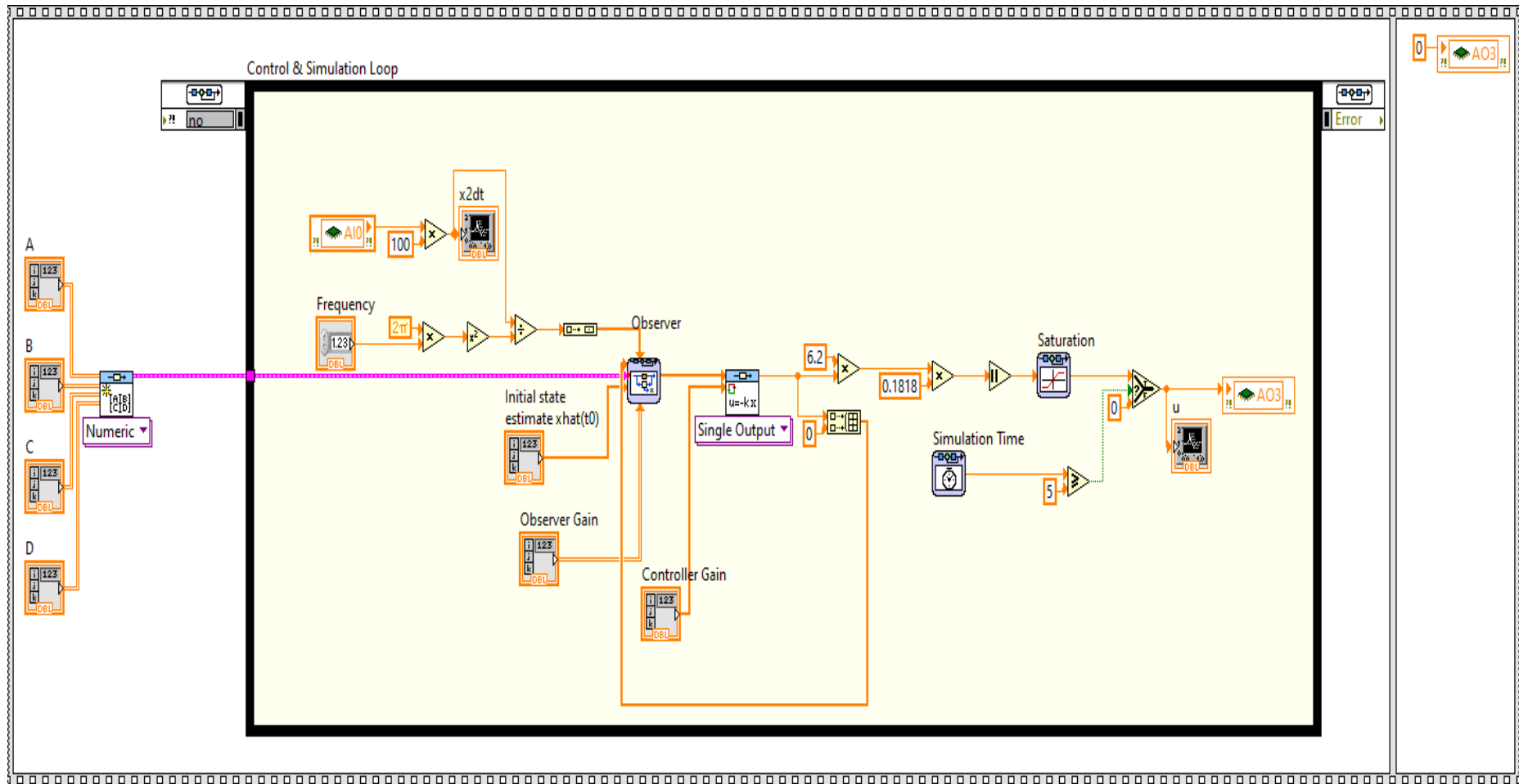


Figure 4.27 LabVIEW program of LQR controller.

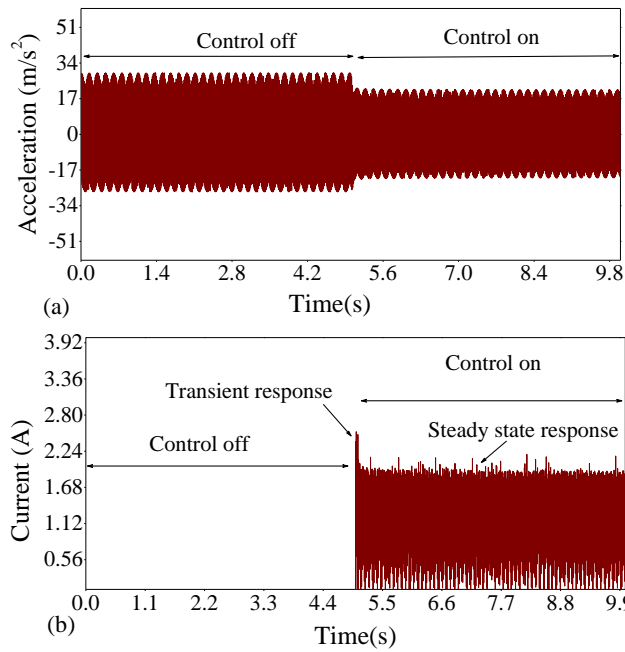


Figure 4.28 Measured responses at 34Hz: (a) acceleration and (b) control current.

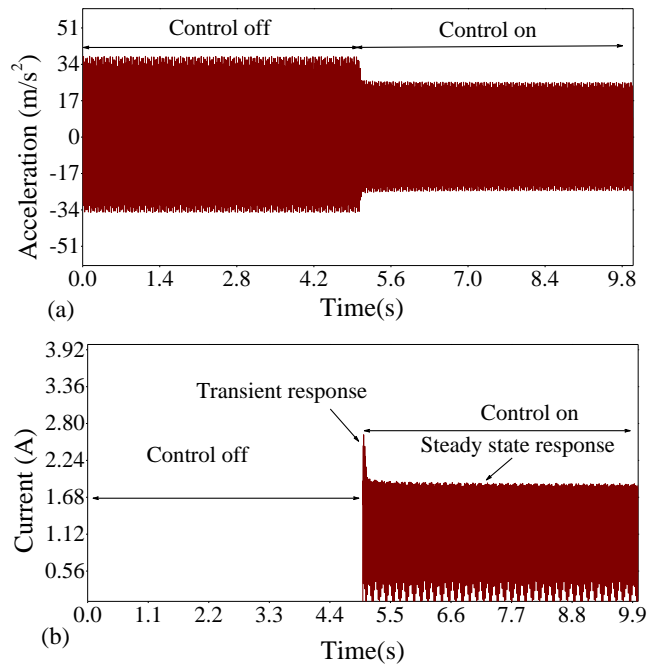


Figure 4.29 Measured responses at 36Hz: (a) acceleration and (b) control current.

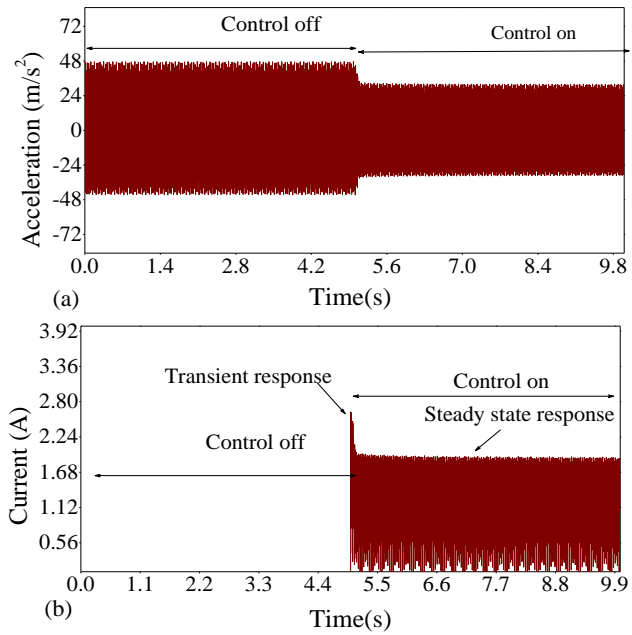


Figure 4.30 Measured responses at 38Hz: (a) acceleration and (b) control current.

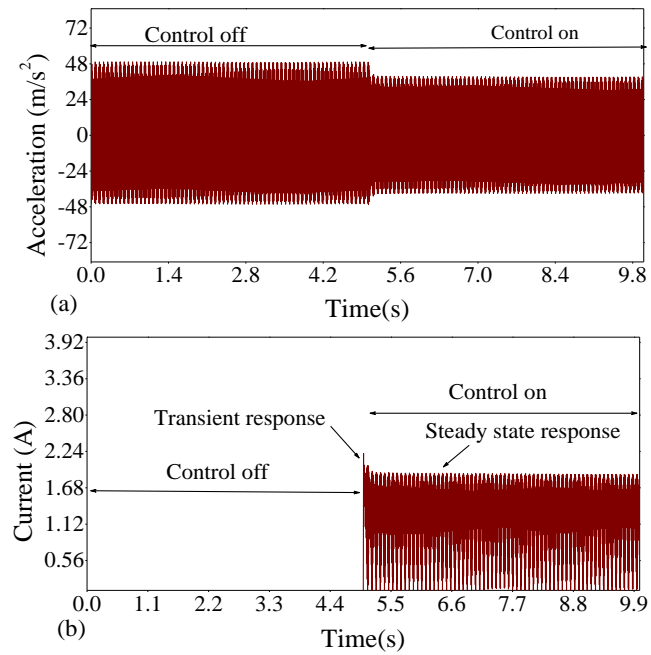


Figure 4.31 Measured responses at 40Hz: (a) acceleration and (b) control current.

Table 4.5 Results of MRE vibration isolation under different excitation frequencies.

Frequency (Hz)	LQR simulation				LQR Experimental			
	$\ddot{x}(m/s^2)$	$\ddot{x}(m/s^2)$	% of	Force	$\ddot{x}(m/s^2)$	$\ddot{x}(m/s^2)$	% of	Current
	Control off	Control on	decrease	(N)	Control off	Control on	decrease	(A)
34	27.52	20.22	26.52	7.44	28.57	20.01	29.96	1.93
36	38.23	24.85	34.99	7.78	36.73	25.05	31.79	1.88
38	45.74	29.92	34.58	9.51	47.41	30.37	35.94	1.89
40	43.15	36.12	16.29	5.49	48.66	37.11	23.73	1.91

4.10 Closure

The current chapter investigated the numerical and experimental performance of the model-based PID and LQR controller on MRE vibration isolation. Optimal parameters of the Bouc-Wen model are used to simulate the model-based controllers. In-house fabricated MRE vibration isolator is subjected to steady-state excitation to ascertain the dynamic properties of the MRE. The natural frequency of the MRE vibration isolation shifts from 39 Hz to 43 Hz with a current of 2.5A. The PID and LQR controllers are analyzed numerically and experimentally for the MRE vibration isolation at the single frequency excitation. The excitation frequency is varied from 34Hz to 40Hz in steps of 2Hz. For the PID controller, the maximum reduction of measured acceleration is 30.27% at a control current of 1.91 A for the excitation frequency of 38Hz.

Similarly, for the LQR controller, the maximum reduction of the measured acceleration is 35.94 % at a control current of 1.89 A. From the results, it is evident that both controllers are effective in the mitigation of vibration. However, the LQR has a higher performance compared to the PID controller. The linear controllers effectively reduce vibration amplitude only when the MRE vibration isolation is linear and time-invariant. As a viscoelastic composite material, MRE behaves nonlinearly at higher displacement and poses time-varying properties. Generally, nonlinear robust and Intelligent adaptive controls are more suitable for dynamic systems with nonlinearity and time-varying properties. Chapter 5 discusses the design and implantations of the nonlinear and intelligent adaptive controls for the MRE vibration isolation.

5. Intelligent Non-Linear Controls for the Magnetorheological Elastomer Vibration Isolation

5.1 Introduction

This chapter discusses the design and implantations of the nonlinear and intelligent nonlinear controls based on neural network and fuzzy system for the Magnetorheological elastomer vibration isolation at single and variable frequencies of excitation.

5.2 Nonlinear Systems and Controls

All the systems existing in today's world possess nonlinearities and uncertainties. The model uncertainties can be classified as structured (parametric) and unstructured (unmodelled dynamics) uncertainties. The structured uncertainties correspond to unknown plant parameters, and unstructured uncertainties correspond to the simplified depiction of systems' dynamics (Lu 2007). These model inaccuracies produce adverse effects on the system to be controlled. To accommodate the same, it is mandatory to design a robust and adaptive controller. The most effective robust controller is the sliding mode control.

Considering the single input nonlinear system (Lu 2007)

$$\ddot{x} = f(X) + b(X) u \quad (5.1)$$

where, \ddot{x} is the state (acceleration) of the system, u is the control input and X is the state vector, $[x \dot{x} \dots x^{(n-1)}]^T$. $f(X)$ is an imprecise system with a known upper bound and is a continuous function of X . Similarly, the control gain $b(X)$ is not precisely known but known of sign and is bounded by continuous functions of X . The objective of the controller is to track the desired time-varying state, x_d in the presence of model imprecision of system. Let the tracking error be

$$e = x - x_d = [e \dot{e} \ddot{e}]^T \quad (5.2)$$

Furthermore, sliding surface $s(t)$ in state-space in R^n by the scalar equation,

$$s(x, t) = (\dot{e} + \lambda e)^{(n-1)} \quad (5.3)$$

where, λ is a positive constant. Considering $n = 2$ we have,

$$s(x, t) = \dot{e} + \lambda e \quad (5.4)$$

For tracking problem, $e = x_d - x$. The sliding surface $s(t)$ has to zero, $s = 0$ for $t > 0$. The control law u can be achieved by choosing such a way that the sliding surface becomes zero and is expressed as,

$$\frac{1}{2} \frac{d}{dt} s^2 \leq -\eta |s| \quad (5.5)$$

Equation (5.5) or sliding condition makes the surface an invariant set. Even with input disturbance and parameter uncertainties, it stays the same as the invariant set. The control law has to be discontinuous around $s(t)$ to consider the presence of model imprecision. This leads to the chattering effect and needs to be removed. This can be attained by smoothing discontinuity present in control law by introducing the thin boundary layer around the switching surface (Liu and Wang 2011) and is expressed as,

$$B(t) = \{x: |s(x, t)| \leq \Phi\} \quad (5.6)$$

where, Φ is the boundary layer thickness. The robust controls are effective with the known bound of model uncertainties, and if the bound is unknown, then the controls become ineffective. This problem can be overcome by using adaptive controls. The adaptive controls similar to robust control but has the additional feature of updating the model during the process with change input. This feature makes the adaptive controls more effective than robust control in unknown model uncertainties (Slotine 1991)(Liu and Wang 2011). The performance of adaptive can be improved by incorporating intelligent systems like Fuzzy systems and Neural networks.

5.3 Fuzzy Systems

5.3.1 Basic Concept

The fuzzy sets were introduced by Zadeh in 1965 (Wang 1997). Till today, the fuzzy system has been used in many applications, including control problems. The fuzzy system is rule-based and utilizes fuzzy logic to approximate any arbitrary systems. IF-THEN statements consist of words that are characterized by continuous membership functions (Wang 1997). Thus, a fuzzy system has mainly three parts,

linguistic variables, membership function and rules. Linguistic variables define the input and output variables of the system to be controlled in the form of words. Thus, the Fuzzy system needs at least one input and one output linguistic variable to define the system.

Considering the X as the universe, the fuzzy set, A of X is defined by (Wang 1997)

$$A = \{(x, \mu_A(x)) | x \in X\} \quad (5.7)$$

where, $\mu_A(x)$ is the membership function (MF) of the fuzzy set, A and x is the element of X . The membership function $\mu_A(x)$ of the fuzzy set, A has values between 0 and 1. The membership function maps each element of the universe to a membership grade between 0 and 1. There are many standard membership functions, which are illustrated in Figure 5.1. If the MF has 0 or 1, the fuzzy set, A is changed to a classical set. Classical sets are also called crisp sets.

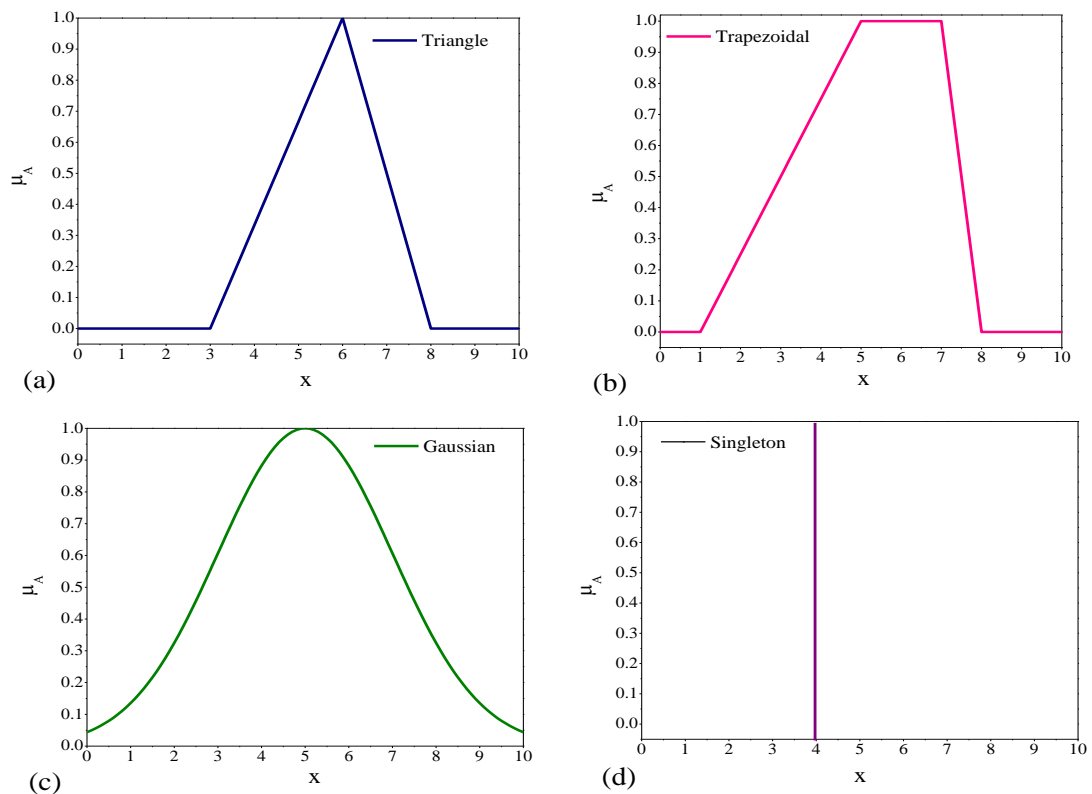


Figure 5.1 Plots of the standard membership functions.

Considering the same operation of fuzzy sets: Intersection and union. Now we assume two fuzzy sets, A and B , in the same universe U .

The union of these two fuzzy sets is a fuzzy set whose membership function is

$$\mu_{A \cup B}(x) = S(\mu_A(x), \mu_B(x)) = \mu_A(x) \tilde{\vee} \mu_B(x) \quad (5.8)$$

where, $\tilde{\vee}$ is an S -norm operator. Considering the two examples of the S norm operator.

$$\text{Maximum: } S_{max}(a, b) = \max(a, b) = a \vee b \quad (5.9)$$

$$\text{Algebraic sum: } S_{ab}(a, b) = a + b - ab \quad (5.10)$$

The intersection of two fuzzy sets, A and B , is a fuzzy set whose membership function is defined as

$$\mu_{A \cap B}(x) = T(\mu_A(x), \mu_B(x)) = \mu_A(x) \tilde{\wedge} \mu_B(x) \quad (5.11)$$

where, $\tilde{\wedge}$ is a T -norm operator. Considering the two examples of the T norm operator.

$$\text{Minimum: } T_{min}(a, b) = \min(a, b) = a \wedge b \quad (5.12)$$

$$\text{Algebraic product: } T_{ab}(a, b) = ab \quad (5.13)$$

Introducing fuzzy relations. A fuzzy relation is defined as it is a fuzzy set in the Cartesian product of U_1, U_2, \dots, U_n , where U_1, U_2, \dots, U_n , are the universe. The fuzzy relations Q in $U_1 \times U_2 \times \dots \times U_n$ as,

$$Q = \left\{ \left((u_1, u_2, \dots, u_n), \mu_Q(u_1, u_2, \dots, u_n) \right) \mid (u_1, u_2, \dots, u_n) \in U_1 \times U_2 \times \dots \times U_n \right\} \quad (5.14)$$

where, $\mu_Q(u_1, u_2, \dots, u_n)$ is the membership function of the fuzzy relation. The Cartesian product of two fuzzy sets U_1 and U_2 is defined as A binary fuzzy relation. Considering X and Y be two universes and a binary fuzzy R is $X \times Y$ is expressed as,

$$R = \left\{ \left((x, y), \mu_R(x, y) \right) \mid (x, y) \in X \times Y \right\} \quad (5.15)$$

An if-then rule can be described as

$$\text{If } x \text{ is } A, \text{ then } y \text{ is } B \quad (5.16)$$

where x and y are the linguistic variables. A and B are the fuzzy sets in X and Y universe. If part (x is A) is called antecedent or premise, then part (y is B) is called the conclusion or consequence. A fuzzy if-then rule is defined as a binary fuzzy relation.

The membership function of fuzzy relation is expressed as,

$$\mu_R(x, y) = \mu_{A \times B}(x, y) = \mu_{A \rightarrow B}(x, y) = \mu_A(x) \tilde{\wedge} \mu_B(x) \quad (5.17)$$

We define inference rule modus ponens as,

Premise 1(rule): if x is A then y is B

Premise 2(fact): x is A

Conclusion: y is B

Further, the generalized modus ponens. The form of fuzzy reasoning is expressed as

Premise 1(rule): if x is A then y is B

Premise 2(fact): x is A'

Conclusion: y is B'

The fuzzy set A' and the fuzzy relation $A \rightarrow B$, the fuzzy set B' is defined as

$$B' = A' \circ R = A' \circ (A \rightarrow B) \quad (5.18)$$

where, $A' \circ R$ is the composition of A' and R . Let us considered two compositions. Max-min composition and max-product composition. The membership function of B' of max-min composition is expressed as,

$$\mu_{B'}(x) = \max_x \min [\mu_{A'}(x), \mu_R(x, y)] \quad (5.19)$$

$$\mu_{B'}(x) = \max_x \min [\mu_{A'}(x), \mu_R(x, y)] = \vee_x [\mu_{A'}(x) \wedge \mu_R(x, y)] \quad (5.20)$$

where, \vee_x is the maximum operation and \wedge is the minimum operation.

The membership function of B' of max-product composition is given by,

$$\mu_{B'}(x) = \max_x [\mu_{A'}(x), \mu_R(x, y)] = \vee_x [\mu_{A'}(x) \mu_R(x, y)] \quad (5.21)$$

The above fuzzy reasoning is used for a single if-then rule ($A \rightarrow B$) with a single antecedent (x is A). We describe two fuzzy rules with two antecedents as follows

$$\text{Premise 1(rule): if } x \text{ is } A_1 \text{ and } y \text{ is } B_1 \text{ then } z \text{ is } C_1 \quad (5.22)$$

$$\text{Premise 1(rule): if } x \text{ is } A_2 \text{ and } y \text{ is } B_2 \text{ then } z \text{ is } C_2$$

$$\text{Premise 3(fact): } x \text{ is } A' \text{ then } y \text{ is } B'$$

$$\text{Conclusion: } z \text{ is } C$$

5.3.2 Fuzzy System and their Properties

The fuzzy system has four major components: fuzzy rule base, fuzzy inference engine, fuzzifier and defuzzifier, as shown in Figure 5.2.

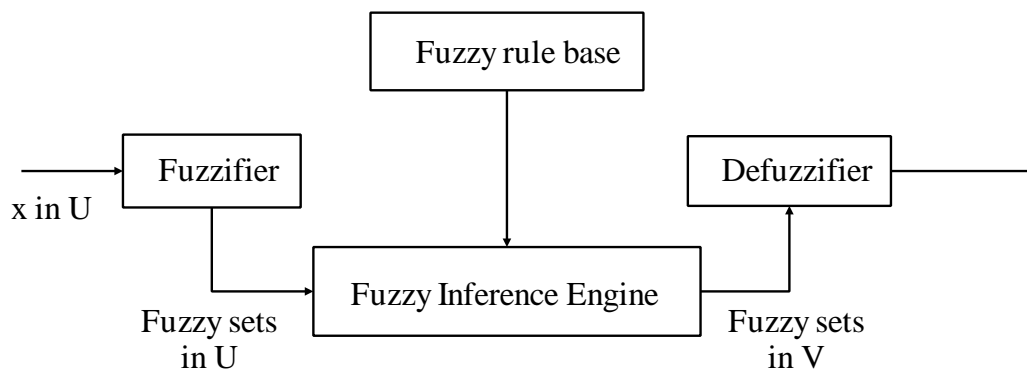


Figure 5.2 Fuzzy system.

The fuzzy rule base contains a set of fuzzy IF-THEN rules. The fuzzy rule is expressed as

$$Ru^l = IF x_1 \text{ is } A_1^l \text{ and } \dots \text{ and } x_n \text{ is } A_n^l, THEN y \text{ is } B^l \quad (5.23)$$

where, A_1^l and B^l are fuzzy sets, respectively. $x = (x_1, x_2, \dots, x_n) \in U$ and $y \in V$ are the input and output linguistic variables of the fuzzy system, and n is the number of rules in the fuzzy system that $l = 1, 2, \dots, n$. The fuzzy rule base is the core of the fuzzy system, where all remaining components are expected to work for its efficient implementation. In that fuzzy inference engine maps the fuzzy set A' in U to a fuzzy set B' in V . One of the types of fuzzy inference engines is the product inference engine. This engine uses Mamdani's product implication, T -norm operators for algebraic products and max for all the S -norm operators.

$$\mu_{B'}(y) = \max_{l=1}^M \sup_{x \in U} (\mu_{A'}(x) \prod_{i=1}^n \mu_{A_i^l}(x_i) \mu_{B^l}(y)) \quad (5.24)$$

The product inference engine finds the fuzzy set B' in V with fuzzy set A' in U is defined. The fuzzifier is used for mapping the real-valued crisp point $x^* \in U \subset R^n$ to fuzzy set A' in U .

The single value fuzzifier maps the real-valued crisp points $x^* \in U$ into single-valued fuzzy set A' in U , whose membership function is 1 at x^* and 0 for all other points, and is expressed as,

$$\mu_{A'}(x) = \begin{cases} 1 & \text{if } x = x^* \\ 0 & \text{otherwise} \end{cases} \quad (5.25)$$

To consider the fuzzy system as a controller, the output has to be a crisp point. The defuzzifier maps the B' in V to crisp value point. Let us introduce the center average defuzzifier and is expressed as

$$y^* = \frac{\sum_{l=1}^M y^l \omega^l}{\sum_{l=1}^M \omega^l} \quad (5.26)$$

where, y^l is the center of the fuzzy set B , ω^l is the height of the fuzzy set B' and $l = 1, 2, \dots, M$ are the number of fuzzy rules. Considering the $M = 2$ we can illustrate the simple example of center average defuzzifier as shown in Figure 5.3.

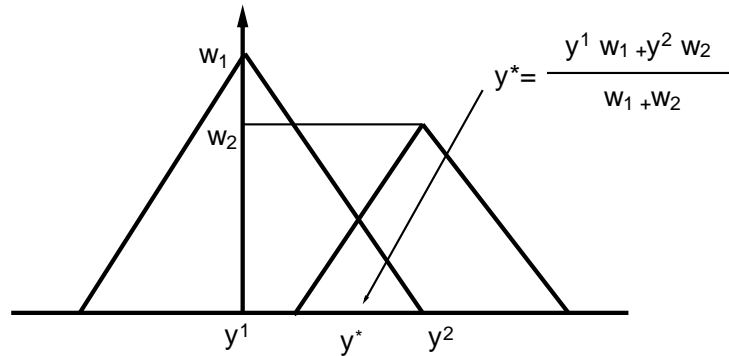


Figure 5.3 Centre average method.

5.3.3 Adaptive Fuzzy System (AFS)

In general, the fuzzy logic control works are based on the principle of universal approximation, and any nonlinear function can be approximated by using fuzzy systems (Wang et al. 2001a). A fuzzy logic contains fuzzy if-then rules and is expressed as

$$R^{(j)}: \text{If } q_0 \text{ is } F_0^j \text{ and } q_n \text{ is } F_n^j \text{ then } p \text{ is } B^j \quad (5.27)$$

where, q_i and p are input and out variables. F_1^j and B^j are fuzzy sets. With center-average defuzzification, product inference and singleton fuzzification, the output of the fuzzy is presented as (Wang et al. 2001a),

$$p(q) = \frac{\sum_{j=1}^l p^j (\prod_{i=1}^n \phi_{F_i^j}(q_i))}{\sum_{j=1}^l \prod_{i=1}^n \phi_{F_i^j}(q_i)} \quad (5.28)$$

where, $\phi_{F_i^j}(q_i)$ is the membership function of the input variable q_i and p^l represents a crisp value at which the membership function ϕ_{B^j} for fuzzy output, the set reaches its maximum value, which is assumed as $\phi_{B^j}(p^l = 1)$.

By introducing the concept of basic fuzzy function, $\phi(q)$. The output of the fuzzy system is given by

$$p(q) = \varphi^T \phi(q) \quad (5.29)$$

where, $\varphi = (p^1, \dots, p^l)^T$, $\phi(q) = (\phi^1(q), \dots, \phi^l(q))^T$, Gaussian membership function and expressed as

$$\phi^j(q) = \frac{\prod_{i=1}^n \phi_{F_i^j}(q_i)}{\sum_{j=1}^l \prod_{i=1}^n \phi_{F_i^j}(q_i)} \quad (5.30)$$

The switching terms, $\eta \tanh(s)$ of sliding mode control is approximated by the fuzzy logic system and written as

$$\hat{h}(s) = \hat{\varphi}^T \phi(s) \quad (5.31)$$

5.4 Neural Network

The human brain processes the information through a network of neurons (Ramírez-Figueroa 2010). The human brain has around 100 to 500 billion neurons interconnected with each other (Ramírez-Figueroa 2010). Where each neuron consists of a nucleus, dendrites, axons and synapses. The computation of information takes place in the nucleus, which is the center of the neuron. The processed information from the nucleus pass to synapses through the axon in the form of an electrical signal. Dendrites and synapses act as input and output of the neurons. The dendrites receive information from

the synapse of another neuron connected with the synaptic gap (Aggarwal 2018), as shown in

Figure 5.4 (Tayyab. 2014). Each neuron has several synapses and dendrites. A neuron can be connected to many other neurons; this leads to sending and accepting information from many other neurons. All the interconnect neuron receives the information having different weights, some have higher weights than others. Also, some excitatory, and some are inhibitory. This characteristic of the biological neural network is central to artificial neural networks (ANN's).

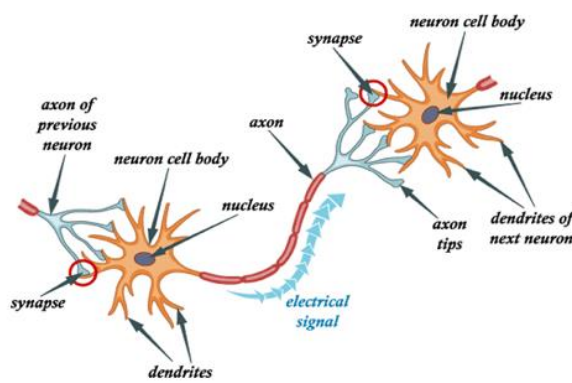


Figure 5.4 Interconnection of biological neural nets (Tayyab. 2014).

Figure 5.5 shows the schematic analogy of a biological neural network. The neuron receives the data with their wights from all other interconnected neurons via input (dendrites), and computed data transmits to other neurons via output (synapses) (Graupe 2013).

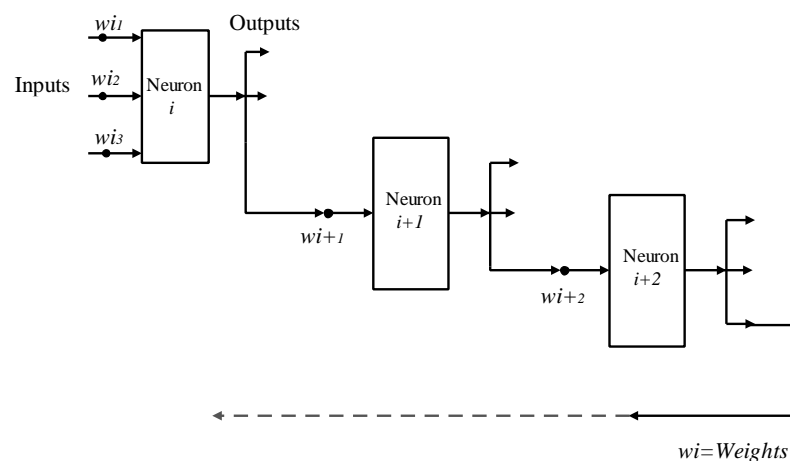


Figure 5.5 Schematic of the analogy of a biological neural network (Graupe 2013).

5.4.1 Radial Basic Function Neural Network

Neural networks work on the universal approximation, and any arbitrary nonlinear system can be approximated using the neural networks adaptive control (Wei et al., 2012).

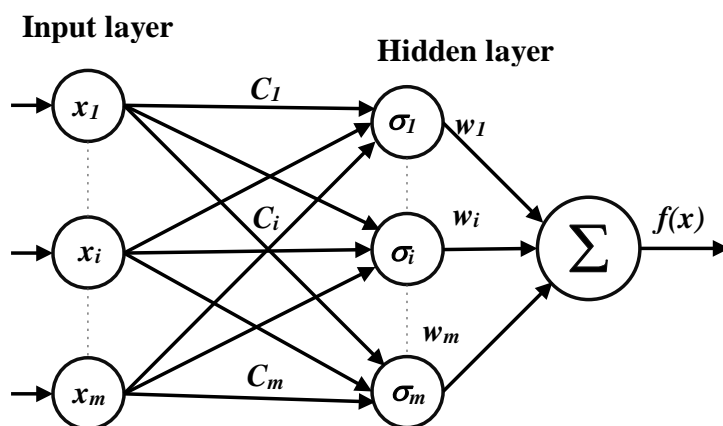


Figure 5.6 Radial basis functions neural network.

In this control, the radial basis function neural network (RBFNN) shown in Figure 5.6 is considered to approximate the nonlinearity and parameter uncertainties of MRE vibration isolation. The approximation function is defined (Vijay and Jena 2018) as

$$f(x) = W^T \sigma(x) + \epsilon(x) \quad (5.32)$$

where, input state vector, $x = [x_1 \ x_i \dots \ x_m]^T$, $W = [w_1 \ w_i \dots \ w_m]^T$ is the weight matrix and ϵ is the approximation error.

The $\sigma(x)$ is the RBF activation functions is defined as

$$\sigma_i(x) = \exp\left(-\frac{\|x - c_i\|^2}{2b_i^2}\right), \quad \text{for } i = 1, 2, \dots, m \quad (5.33)$$

where, c_i and b_i are the center and width of the i^{th} neuron. Fuzzy systems and neural network have been considered for the development of adaptative observer-based intelligent controls for the MRE vibration isolation having time-varying properties. The RBF activation functions for the given input, x is as shown in Figure 5.7

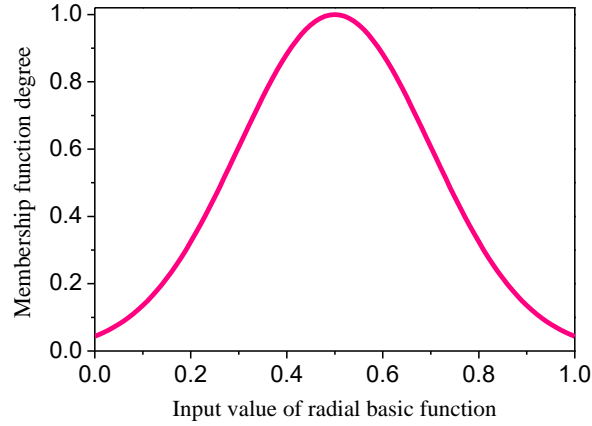


Figure 5.7 Plot of radial basic function.

5.5 Design of Nonlinear Robust and Intelligent Adaptive Control Strategies

Real-time implementation of MRE vibration isolation depends on current, and the controller is crucial to regulate the electromagnet's current. The following sections discuss the theoretical design and stability analysis of the proposed control strategies for MRE vibration isolation.

5.5.1 Sliding Mode Control (SMC)

Sliding mode control is nonlinear control that works efficiently with parameter uncertainties owing to its robust nature. It contains an equivalent and a switching control term to provide stability to the uncertainties and external disturbance (Parameswaran et al., 2015).

The governing differential equation of MRE vibration isolation with the control input and parameter uncertainties Figure 5.8 is given by

$$m\ddot{x} + k(x - x_b) + c(\dot{x} - \dot{x}_b) = u(t) + dt \quad (5.34)$$

where, m , k and c are the mass, stiffness and damping coefficient, respectively. x is the displacement of the mass, x_b is the displacement of the base, and both are a function of time, t . u is the control input, and dt is the time-varying uncertainties with known upper bounds, D , i.e., $|dt| \leq D$.

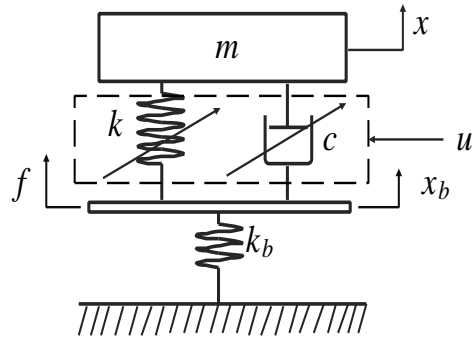


Figure 5.8 Schematic of MRE vibration isolation.

Rearranging the Equation (5.34), we obtain the acceleration of the MRE vibration isolation as

$$\ddot{x} = f(x, t) + u + dt \quad (5.35)$$

where, $f(x, t) = -m^{-1} (k(x - x_b) + c(\dot{x} - \dot{x}_b))$

The total control effort of the MRE vibration isolation, u is of the form

$$u = u_{eq} + u_s \quad (5.36)$$

where, u_{eq} is the equivalent control and u_s is the switching control.

The sliding surface, s is of the type

$$s = -\lambda e - \dot{e} \quad (5.37)$$

where, e is the error signal, i.e., the difference between actual displacement, x , and desired displacement, x_d of MRE vibration isolation and λ is the positive constant. The sliding mode control ensures that, $e \rightarrow 0$. This can be achieved by compelling state trajectory to move towards the sliding surface (Suryawanshi et al., 2016).

Differentiating Equation (5.37) with respect to time, t and using the Equation (5.35), we have

$$\dot{s} = -\lambda \dot{e} - \ddot{x}_d + f(x, t) + u + dt \quad (5.38)$$

To achieve the desired state trajectory without uncertainties and external disturbance, the equivalent control, u_{eq} is obtained by equating Equation (5.38) to zero. Thus, we have,

$$u_{eq} = \lambda \dot{e} + \ddot{x}_d - f(x, t) - dt \quad (5.39)$$

However, with parameter uncertainties and disturbance, the equivalent control does not guarantee good results and might lead to instability. Therefore, secondary control must be considered for the stability of the system. The total control with secondary control is expressed as

$$u = \lambda \dot{e} + \ddot{x}_d - f(x, t) + u_s \quad (5.40)$$

where, $u_s = -\eta \text{sign}(s)$ and η is a positive constant.

With parameter uncertainties and external disturbance, $e \rightarrow 0$ can be achieved with the following condition.

$$s\dot{s} = s u_s = s [-\eta \text{sign}(s)] = -\eta |s| \leq 0 \quad (5.41)$$

Discontinuous function presents in sliding mode control includes chattering phenomena that lead to variation in the control output. The boundary layer is adapted to minimize the chattering effect. Further, the discontinuous function changed to a continuous function close to the switching surface. The relation of the boundary layer is expressed as

$$B(t) = \{x: |s(x, t)| \leq \Phi\} \quad (5.42)$$

where, Φ is the boundary layer thickness.

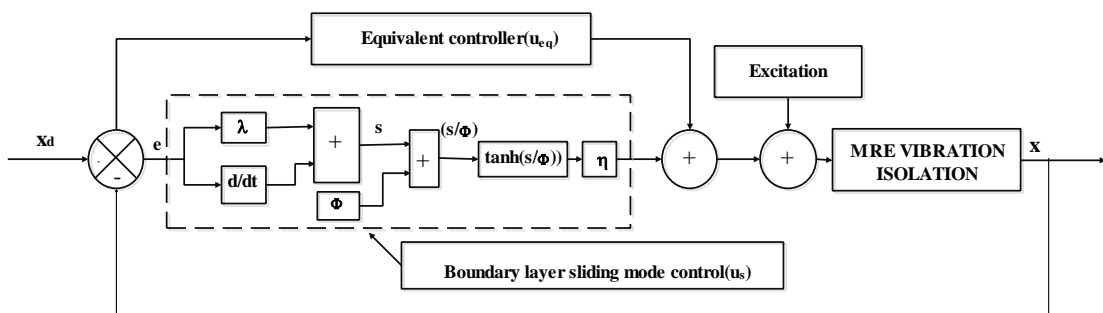


Figure 5.9 Schematic of boundary layer sliding mode control.

With the addition of the boundary layer, the boundary sliding mode control (BSMC), as shown in Figure 5.9, can be expressed as

$$u = \lambda \dot{e} + \ddot{x}_d - f(x, t) - \eta \text{sat}(s/\Phi) \quad (5.43)$$

where the saturation function is given (Fei and Xin 2015) by

$$\text{sat}\left(\frac{s}{\Phi}\right) = \begin{cases} \tanh\left(\frac{s}{\Phi}\right), & \text{for } \left|\frac{s}{\Phi}\right| \geq 1 \\ \frac{s}{\Phi}, & \text{for } \left|\frac{s}{\Phi}\right| \leq 1 \end{cases} \quad (5.44)$$

5.5.2 Adaptive Observer-based Intelligent Nonlinear Control

Equation (5.43) is a robust nonlinear control and works with a known bound of parameter uncertainties and disturbance. However, when the range of the uncertainties is unknown, the robust control is less effective. In such cases, adaptive control proves to be a beneficial approach. The following sections discuss adaptive control and observer design based on intelligent systems like neural networks and fuzzy logic systems.

Defining the error signal of position, e to design the control (Vijay and Jena 2016)

$$e = x_{1d} - x_1 \quad (5.45)$$

$$\dot{x}_r = x_{2d} - \lambda e \quad (5.46)$$

where, x_{1d} and x_{2d} are the desired displacement and velocity of the system. \dot{x}_r and λ are auxiliary signals and positive constant, respectively. Redefining the governing differential MRE vibration isolation as single a degree of freedom system as follows

$$m\dot{x}_2 + kx_1 + cx_2 = u + dt \quad (5.47)$$

The sliding surface is defined as

$$s = x_2 - \dot{x}_r = \dot{e} + \lambda e \quad (5.48)$$

Substituting Equation (5.46) and (5.48) in Equation (5.47), we obtain as,

$$m\dot{s} = -cs + f(x) - dt + u \quad (5.49)$$

$$f(x) = m\ddot{x}_r + kx_1 + cx_2 \quad (5.50)$$

$$f(x) = -m(\dot{x}_{2d} - \lambda e) + kx_1 + c(x_{2d} - \lambda e) \quad (5.51)$$

The approximation of $f(x)$ is defined as

$$\hat{f}(x) = \widehat{W}^T \sigma(x) + \epsilon(x) \quad (5.52)$$

Considering Equations. (5.32), (5.49) and (5.52), we obtain

$$m\dot{s} = -cs + f(x) - dt + u \quad (5.53)$$

The total control input of neural network fuzzy sliding mode control defined as $u = u_{eq} + u_s$, u_{eq} is equivalent control input, which is approximated with a neural network and $u_s = -\kappa_0 s - \eta \tanh(s)$ is sliding mode control. The switching terms, $\eta \tanh(s)$, is approximated with fuzzy logic. κ_0 is a positive constant.

Rewriting Equation (5.53) by considering both the neural network and Fuzzy logic system,

$$m\dot{s} = -cs - \kappa_0 s + \varphi^{*T} \phi(s) + \omega^* + W^{*T} \sigma(x) + \epsilon^* + dt \quad (5.54)$$

$$m\dot{s} = -cs - \kappa_0 s + \tilde{\varphi}^T \phi(s) + \hat{\varphi}^T \phi(s) + \omega^* + \varepsilon_{fs} + \widehat{W}^T \sigma(x) + \widetilde{W}^T \sigma(x) + \epsilon^* + \varepsilon_{nn} \quad (5.55)$$

where, $\widetilde{W} = W^* - \widehat{W}$, W^* is the optimal weight matrix, $\tilde{\varphi} = \varphi^* - \hat{\varphi}$, φ^* is the optimal output membership function vector, and ε_{fs} and ε_{nn} are disturbances associated with fuzzy logic and neural network, respectively.

The adaptive law of neural network for the equivalent control term is

$$\dot{\widehat{W}} = -\dot{\widetilde{W}} = \beta \sigma(x) s \quad (5.56)$$

and adaptive law of fuzzy system for switching control term is

$$\dot{\hat{\varphi}} = -\dot{\tilde{\varphi}} = \gamma \phi(s) s \quad (5.57)$$

where, β and γ are the adaptive gains of neural network and fuzzy logic, respectively.

Lyapunov stability candidate function is defined as

$$V = \frac{1}{2} s^T m s + \frac{1}{2\beta} \tilde{W}^T \tilde{W} + \frac{1}{2\gamma} \tilde{\varphi}^T \tilde{\varphi} \quad (5.58)$$

$$\dot{V} = \frac{1}{2} s^T \dot{m} s + s^T m \dot{s} + \frac{1}{2\beta} \tilde{W}^T \dot{\tilde{W}} + \frac{1}{2\gamma} \tilde{\varphi}^T \dot{\tilde{\varphi}} \quad (5.59)$$

Substituting the Equation (5.55) and Equation (5.59),

$$\begin{aligned} \dot{V} = & \frac{1}{2} s^T \dot{m} s + s^T (-cs - \kappa_0 s - \tilde{\varphi}^T \phi(s) + \hat{\varphi}^T \phi(s) + \omega^* + \varepsilon_{fs} + \hat{W}^T \sigma(x) \\ & + \tilde{W}^T \sigma(x) + \epsilon^* + \varepsilon_{nn}) + \frac{1}{2\beta} \tilde{W}^T \dot{\tilde{W}} + \frac{1}{2\gamma} \tilde{\varphi}^T \dot{\tilde{\varphi}} \end{aligned} \quad (5.60)$$

$$\begin{aligned} \dot{V} = & \frac{1}{2} s^T (\dot{m} - 2c) s + s^T (-\kappa_0 s + \omega^* - \varepsilon_{fs} + \epsilon^* - \varepsilon_{nn}) + \tilde{W}^T \left(\frac{1}{\beta} \dot{\tilde{W}} + \sigma(x) \right) s^T \\ & + \tilde{\varphi}^T \left(\frac{1}{\gamma} \dot{\tilde{\varphi}} + \phi(s) \right) s^T \end{aligned} \quad (5.61)$$

By solving Equation (5.61), we get

$$\dot{V} \leq -\kappa_0 s^T s + \|s\| \theta_{nn} + \|s\| \theta_{fs} \quad (5.62)$$

where, $\theta_{nn} = \|\epsilon^* - \varepsilon_{nn}\|$ and $\theta_{fs} = \|\omega^* - \varepsilon_{fs}\|$ are upper bounds of neural network and fuzzy system approximation, respectively. The terms $\|s\| \theta_{nn} + \|s\| \theta_{fs}$ are bounded by

$$\|s\| \theta_{nn} \leq \frac{1}{2} (\|s\|^2 + \alpha \theta_{nn}^2) \quad (5.63)$$

and

$$\|s\| \theta_{fs} \leq \frac{1}{2} (\|s\|^2 + \alpha \theta_{fs}^2) \quad (5.64)$$

where, $\alpha > 0$ is chosen such that $\int_0^\infty \alpha dt < \infty$.

Substituting Equations (5.63) and (5.64) into Equation (5.62), we get the stability of control (Sun et al. 2011) as

$$\dot{V} \leq -\kappa_0 \|s\|^2 + \frac{1}{2} (\|s\|^2 + \alpha(\theta_{nn}^2 + \theta_{fs}^2)) \quad (5.65)$$

Integrating Equation (5.65) on both sides for $t = 0$ to T ,

$$V(T) - V(0) \leq -\left(\kappa_0 - \frac{1}{2}\right) \int_0^T \|s\|^2 dt + \frac{1}{2} (\theta_{nn}^2 + \theta_{fs}^2) \int_0^T \alpha dt \quad (5.66)$$

Since $V(T) \geq 0$ and $\int_0^T \alpha dt < \infty$,

$$\lim_{T \rightarrow \infty} \sup \frac{1}{T} \int_0^T \|s\|^2 dt \leq \frac{1}{\left(\kappa_0 - \frac{1}{2}\right)} \left[V(0) + \frac{1}{2} (\theta_{nn}^2 + \theta_{fs}^2) \int_0^T \alpha dt \right] \lim_{T \rightarrow \infty} \frac{1}{T} \quad (5.67)$$

5.5.2.1 Neural network-based adaptive observer (NNAO)

In the present study, a neural network-based adaptive observer (Vijay and Jena 2016) has been utilized to estimate the displacement and velocity of the proposed MRE vibration isolation with parameter uncertainties and external disturbance. For completeness, the following relations are considered. The acceleration of the MRE vibration isolation is defined by

$$\dot{x}_2 = f(x_1, x_2) + m^{-1}u - m^{-1}dt \quad (5.68)$$

where,

$$f(x_1, x_2) = m^{-1}(-kx_1 - cx_2) \quad (5.69)$$

The neural network approximation of Equation (5.69) is given by

$$f(x_1, x_2) = W_o^{*T} \sigma_o(x_1, x_2) + \epsilon_o^* \quad (5.70)$$

where, W_o^{*T} is the ideal weight matrix of observer and ϵ_o^* is an approximation error.

The neural network-based adaptive observer estimates displacement, x_1 and velocity, x_2 as \hat{x}_1 and \hat{x}_2 , respectively, and estimation errors are $\tilde{x}_1 = x_1 - \hat{x}_1$ and $\tilde{x}_2 = x_2 - \hat{x}_2$. The estimation of $f(x_1, x_2)$ is defined as

$$f(x_1, x_2) = \widehat{W}_o^T \sigma_o(\hat{x}_1, \hat{x}_2) \quad (5.71)$$

The neural network-based adaptive observer is defined,

$$\dot{\hat{x}}_1 = \hat{x}_2 + \kappa_1(x_1 - \hat{x}_1) \quad (5.72)$$

$$\dot{\hat{x}}_2 = \widehat{W}_o^T \sigma_o(\hat{x}_1, \hat{x}_2) - m^{-1}dt + \kappa_2 \tilde{x}_1 + \kappa_0 \dot{\tilde{x}}_1 \quad (5.73)$$

$$\dot{\tilde{x}}_2 = \dot{x}_2 - \hat{x}_2 \quad (5.74)$$

$$\begin{aligned} \dot{\tilde{x}}_2 = & W_o^{*T} \sigma_o(x_1, x_2) - W_o^{*T} \sigma_o(x_1, x_2) + W_o^{*T} \sigma_o(x_1, x_2) + \epsilon_o^* + m^{-1}u \\ & - m^{-1}dt - \widehat{W}_o^T \sigma_o(\hat{x}_1, \hat{x}_2) - m^{-1}dt + \kappa_2 \tilde{x}_1 + \kappa_0 \dot{\tilde{x}}_1 \end{aligned} \quad (5.75)$$

$$\dot{\tilde{x}}_2 = W_o^{*T} \tilde{\sigma}_o(x_1, x_2) - \widehat{W}_o^T \sigma_o(\hat{x}_1, \hat{x}_2) - m^{-1}dt + \kappa_2 \tilde{x}_1 + \kappa_0 \dot{\tilde{x}}_1 \quad (5.76)$$

$$\dot{\tilde{x}}_1 = \tilde{x}_2 - \kappa_1 \tilde{x}_1 \quad (5.77)$$

$$\dot{\tilde{x}}_2 = W_o^{*T} \tilde{\sigma}_o(x_1, x_2) - \widehat{W}_o^T \sigma_o(\hat{x}_1, \hat{x}_2) - m^{-1}dt + \epsilon_o^* + \kappa_2 \tilde{x}_1 + \kappa_0 \dot{\tilde{x}}_1 \quad (5.78)$$

By substituting Eq. (5.74) into (5.78), we get,

$$\dot{\tilde{x}}_2 = W_o^{*T} \tilde{\sigma}_o(x_1, x_2) - \widehat{W}_o^T \sigma_o(\hat{x}_1, \hat{x}_2) - m^{-1}dt + \epsilon_o^* + \kappa_0 \dot{\tilde{x}}_1 \quad (5.79)$$

The estimated adaptive law for the neural network-based adaptive observer is,

$$\dot{\widehat{W}}_o = -\dot{\widetilde{W}}_o = \beta_o \sigma_o(\hat{x}_1, \hat{x}_2) \tilde{x}_2^T \quad (5.80)$$

β_o is the adaptive gain of the neural network.

Lyapunov stability function of the adaptive observer is defined as,

$$V = \frac{1}{2} \tilde{x}_2^T \tilde{x}_2 + \frac{1}{2\beta_o} \widetilde{W}_o^T \widetilde{W}_o \quad (5.81)$$

$$\begin{aligned} \dot{V} = & \tilde{x}_2^T (W_o^{*T} \tilde{\sigma}_o(x_1, x_2) - \widehat{W}_o^T \sigma_o(\hat{x}_1, \hat{x}_2) - m^{-1}dt + \epsilon_o^* + \kappa_0 \dot{\tilde{x}}_1) \\ & + \frac{1}{\beta_o} \widetilde{W}_o^T \dot{\widetilde{W}}_o \end{aligned} \quad (5.82)$$

$$\begin{aligned} \dot{V} = & \tilde{x}_2^T (W_o^{*T} \tilde{\sigma}_o(x_1, x_2) - m^{-1}dt + \epsilon_o^* - \kappa_0 \dot{\tilde{x}}_1) \\ & + \widetilde{W}_o^T \left(\frac{1}{\beta_o} \dot{\widetilde{W}}_o + \sigma_o(\hat{x}_1, \hat{x}_2) \tilde{x}_2^T \right) \end{aligned} \quad (5.83)$$

$$\dot{V} \leq -\kappa_0 \tilde{x}_2^T \tilde{x}_2 + \|\tilde{x}_2\| \delta \quad (5.84)$$

$$\dot{V} \leq -\kappa_0 \tilde{x}_2^T \tilde{x}_2 + \|\tilde{x}_2\| \delta \quad (5.85)$$

where, $\delta = \|W_o^{*T} \tilde{\sigma}_o(x_1, x_2) - m^{-1} dt + \epsilon_o^*\|$ is the upper bound of the NN approximation error.

The term, $\|\tilde{x}_2\| \delta$ is bounded by $\|\tilde{x}_2\| \delta \leq \left(\frac{1}{2} \|\tilde{x}_2\|^2 + \alpha \delta^2\right)$ and substituting it into Equation (5.85) for the stability analysis, we have

$$\dot{V} \leq -\kappa_0 \tilde{x}_2^T \tilde{x}_2 + \left(\frac{1}{2} \|\tilde{x}_2\|^2 + \alpha \delta^2\right) \quad (5.86)$$

Integrating both side of the Equation (5.86) from $t=0$ to T , we obtain

$$V(T) - V(0) \leq -\left(\kappa_0 - \frac{1}{2}\right) \int_0^T \|\tilde{x}_2\|^2 dt + \frac{1}{2} \delta^2 \int_0^T \alpha dt \quad (5.87)$$

Since $V(T) \geq 0$ and $\int_0^T \alpha dt < \infty$

$$\lim_{T \rightarrow \infty} \sup \frac{1}{T} \int_0^T \|\tilde{x}_2\|^2 dt \leq \frac{1}{\left(\kappa_0 - \frac{1}{2}\right)} \left[V(0) + \frac{1}{2} \delta^2 \int_0^T \alpha dt \right] \lim_{T \rightarrow \infty} \frac{1}{T} \quad (5.88)$$

5.5.2.2 Neural network-based adaptive observer neural network fuzzy sliding mode control (NNAONFSMC)

Neural network fuzzy sliding mode control has been developed by considering neural network-based adaptive observer. Figure 5.10 depicts the proposed controller. The estimated errors of the displacement and velocity of the MRE vibration isolation, respectively, are defined as

$$\hat{e} = x_{1d} - \hat{x}_1 \quad (5.89)$$

$$\dot{\hat{e}} = x_{2d} - \hat{x}_2 \quad (5.90)$$

and the estimated sliding surface as

$$\hat{s} = \dot{\hat{e}} + \lambda \hat{e} \quad (5.91)$$

The neural network adaptive observer estimates x_1 and x_2 as \hat{x}_1 and \hat{x}_2 , respectively, and estimation errors are $\tilde{x}_1 = x_1 - \hat{x}_1$ and $\tilde{x}_2 = x_2 - \hat{x}_2$.

The estimation of the $f(x)$ is expressed as

$$\hat{f}(\hat{x}) = \hat{W}_c^T \sigma(\hat{x}) \quad (5.92)$$

where, \hat{W}_c^T and $\sigma(\hat{x})$ are the weight matrix and RBFNN input function, respectively.

The total control law of the NNAONFSMC is defined as

$$u = -\kappa_0 \hat{s} - \hat{\phi}_c^T \phi(\hat{s}) - \hat{W}_c^T(\hat{x}) \quad (5.93)$$

The tunable adaptive law of neural network and fuzzy system are defined as

$$\dot{\hat{W}}_c = -\dot{\tilde{W}}_c = \beta_c \sigma(\hat{x}) \hat{s}^T \quad (5.94)$$

$$\dot{\hat{\phi}}_c = -\dot{\tilde{\phi}}_c = \gamma_c \phi(\hat{s}) \hat{s}^T \quad (5.95)$$

β_c and γ_c the adaptive gain of neural-network and fuzzy system of controls

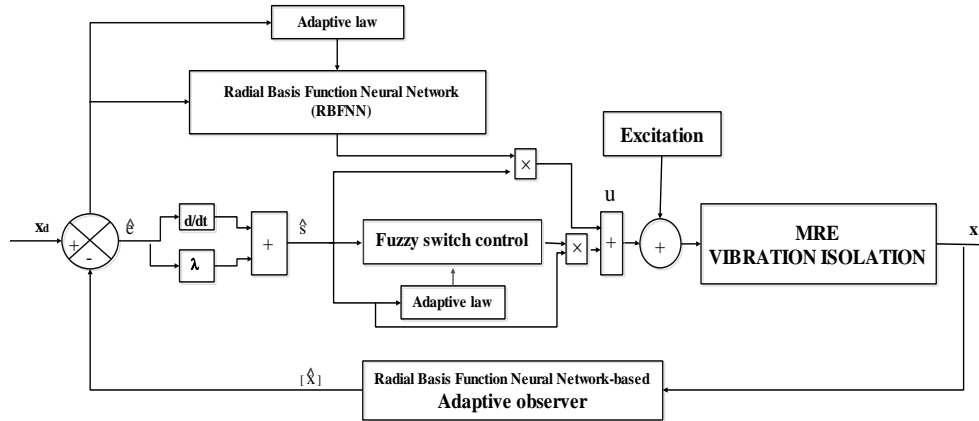


Figure 5.10 Schematic of neural network adaptive observer-based neural network fuzzy sliding mode control.

Lyapunov stability function of NNANFOSMC is defined (Sun et al. 2011) as

$$V = V_o + V_c \quad (5.96)$$

where, V_o and V_c are observer and controller stability candidate, respectively, defined

by

$$V_o = \frac{1}{2} \tilde{x}_2^T \tilde{x}_2 + \frac{1}{2\beta} \tilde{W}_o^T \tilde{W}_o \quad (5.97)$$

$$V_c = \frac{1}{2} m s^T s + \frac{1}{2\beta} \tilde{W}_c^T \tilde{W}_c + \frac{1}{2\gamma} \tilde{\varphi}_c^T \tilde{\varphi}_c \quad (5.98)$$

The derivative of Equation (5.98) is given by

$$\dot{V}_c = \frac{1}{2} s^T \dot{m} s + s^T m \dot{s} + \frac{1}{2\beta} \tilde{W}_c^T \dot{\tilde{W}}_c + \frac{1}{2\gamma} \tilde{\varphi}_c^T \dot{\tilde{\varphi}}_c \quad (5.99)$$

$$\begin{aligned} &= \frac{1}{2} s^T \dot{m} s + s^T \times (-cs - \kappa_0 s - \tilde{\varphi}_c^T \phi(s) + \hat{\varphi}_c^T \phi(s) + \omega^* + \hat{W}_c^T \sigma(x) \\ &\quad + \tilde{W}_c^T \sigma(x) + \epsilon^* + dt) + \frac{1}{2\beta} \tilde{W}_c^T \dot{\tilde{W}}_c + \frac{1}{2\gamma} \tilde{\varphi}_c^T \dot{\tilde{\varphi}}_c \end{aligned} \quad (5.100)$$

$$\begin{aligned} &= \frac{1}{2} s^T (\dot{m} - c) s + s^T \times (-\kappa_0 \hat{s} - \tilde{\varphi}_c^T \phi(s) + \hat{\varphi}_c^T \phi(s) + \omega^* + \hat{W}_c^T \sigma(x) \\ &\quad + \tilde{W}_c^T \sigma(x) + \epsilon^* + dt) + \frac{1}{2\beta_c} \tilde{W}_c^T \dot{\tilde{W}}_c + \frac{1}{2\gamma_c} \tilde{\varphi}_c^T \dot{\tilde{\varphi}}_c \end{aligned} \quad (5.101)$$

Considering, $s = \hat{s} + \tilde{x}_2$ and substituting it into Eq.(5.101), (Vijay and Jena 2016) we get,

$$\begin{aligned} &= \hat{s}^T (\hat{\varphi}_c^T \tilde{\varphi}(\hat{s}) + \omega^* + \hat{W}_c^T \tilde{\sigma}(\hat{x}) + \epsilon^* - dt) \\ &\quad + \tilde{x}_2^T (\hat{W}_c^T \tilde{\sigma}(x) + \tilde{W}_c^T \sigma(x) + \epsilon^* - dt) - \kappa_0 \hat{s} \hat{s}^T - \kappa_0 \hat{s} \tilde{x}_2^T \\ &\quad + \tilde{W}_c^T \left(\frac{1}{\beta_c} \dot{\tilde{W}}_c + \sigma(\hat{x}) \right) \hat{s}^T + \tilde{\varphi}_c^T \left(\frac{1}{\gamma_c} \dot{\tilde{\varphi}}_c + \phi(\hat{s}) \right) \hat{s}^T \end{aligned} \quad (5.102)$$

Consider an upper bound of approximation error of both neural network and fuzzy system of the controller as $\theta_{nn} = \|\hat{W}_c^T \sigma(\hat{x}) + \epsilon^* - dt\|$, $\theta_{fs} = \|\hat{\varphi}_c^T \phi(\hat{s}) + \omega^* - dt\|$ and adaptive observer, $\xi = \|\hat{W}^T \sigma(\hat{x}) + \tilde{W}^T \sigma(\hat{x}) + \epsilon^* - dt\|$.

Equation (5.102) is rewritten as

$$\dot{V}_c \leq \|\hat{s}\|(\theta_{nn} + \theta_{fs}) + \|\tilde{x}_2\|(\xi) - \kappa_0 \hat{s} \hat{s}^T - \kappa_0 \hat{s} \tilde{x}_2^T \quad (5.103)$$

The terms, $\|\hat{s}\|(\theta_{nn} + \theta_{fs})$, $\kappa_0 \hat{s} \tilde{x}_2^T$ and $\|\tilde{x}_2\|(\xi)$ are bounded by

$$\|\hat{s}\|(\theta_{nn} + \theta_{fs}) \leq \frac{1}{2} (\|\hat{s}\|^2 + \alpha(\theta_{nn} + \theta_{fs})^2) \quad (5.104)$$

$$\|\tilde{x}_2\|(\xi) \leq \frac{1}{2} (\|\hat{x}_2\|^2 + \alpha \xi^2) \quad (5.105)$$

$$-\kappa_0 \hat{s} \tilde{x}_2^T \leq \frac{\kappa}{2} (\|\hat{s}\|^2 + \|\hat{x}_2\|^2) \quad (5.106)$$

The above terms are substituted into Equation (5.103), we obtain the stability criteria as

$$\dot{V}_c \leq -\left(\frac{\kappa_0}{2} - \frac{1}{2}\right) \|\hat{s}\|^2 + \left(\frac{\kappa_0}{2} - \frac{1}{2}\right) \|\tilde{x}_2\|^2 + \frac{1}{2}\alpha(\theta_{nn}^2 + \theta_{fs}^2 + \xi^2) \quad (5.107)$$

Lyapunov stability function of the adaptive observer is derived from Equation (5.96) and Equation (5.80), that is,

$$\dot{V}_o = \tilde{x}_2^T (\widehat{W}_o^T \tilde{\sigma}(x) + \widetilde{W}_o^T \sigma(x) + \epsilon^* - dt) - \kappa_0 \tilde{x}_2^T \tilde{x}_2 + \widetilde{W}_o^T \left(\frac{1}{\beta_o} \dot{\widetilde{W}}_o + \sigma(\hat{x}) \right) \tilde{x}_2^T \quad (5.108)$$

$\psi_{nn} = \|(\widehat{W}_o^T \tilde{\sigma}(x) + \widetilde{W}_o^T \sigma(x) + \epsilon^* - dt)\|$ is the upper bound of error and bounded by

$$\|\tilde{x}_2\| \psi_{nn} \leq \frac{1}{2} (\|\tilde{x}_2\|^2 + \alpha \psi_{nn}^2) \quad (5.109)$$

The Equation (5.108) becomes

$$\dot{V}_o \leq -\kappa_0 \tilde{x}_2^T \tilde{x}_2 + \frac{1}{2} (\|\tilde{x}_2\|^2 + \alpha \psi_{nn}^2) \quad (5.110)$$

The derivate of the Equation (5.96) is written as

$$\dot{V} \leq \dot{V}_o + \dot{V}_c \quad (5.111)$$

$$\dot{V} \leq -\frac{1}{2}(\kappa_0 - 1) \|\hat{s}\|^2 - \frac{1}{2}(\kappa_0 - 2) \|\tilde{x}_2\|^2 + \frac{1}{2}\alpha(\theta_{nn}^2 + \theta_{fs}^2 + \xi^2 + \psi_{nn}^2) \quad (5.112)$$

Integrating Equation (5.112) with respect to time, t , on both sides from $t = 0$ to T ,

$$\begin{aligned} V(T) - V(0) &\leq -\frac{1}{2}(\kappa_0 - 1) \int_0^T \|s\|^2 dt - \frac{1}{2}(\kappa_0 - 2) \int_0^T \|\tilde{x}_2\|^2 dt + \frac{1}{2}(\theta_{nn}^2 + \theta_{fs}^2 \\ &\quad + \xi^2 + \psi_{nn}^2) \int_0^T \alpha dt \end{aligned} \quad (5.113)$$

Since $V(T) \geq 0$ and $\int_0^T \alpha dt < \infty$ (Vijay and Jena 2016) we have

$$\begin{aligned} \limsup_{T \rightarrow \infty} \frac{1}{T} \left[(\kappa_0 - 1) \int_0^T \|s\|^2 dt + (\kappa_0 - 2) \int_0^T \|\tilde{x}_2\|^2 dt \right] \\ \leq 2 \left[V(0) \frac{1}{2} (\theta_{nn}^2 + \theta_{fs}^2 + \xi^2 + \psi_{nn}^2) \int_0^T \alpha dt \right] \lim_{T \rightarrow \infty} \frac{1}{T} \end{aligned} \quad (5.114)$$

From the Equations (5.113) and (5.114), it is evident that, $\hat{x} \rightarrow 0$ and $\hat{s} \rightarrow 0$ as $t \rightarrow \infty$. These conditions prove that the proposed NNAONFSMC is asymptotically stable (Vijay and Jena 2016).

5.6 Simulation Analysis of Proposed Controllers

The MRE vibration isolation is simulated with the proposed controllers under single and variable frequency excitation using the MATLAB/Simulink. The parameters of the MRE vibration isolation considered for simulation study are mass, $m = 0.61\text{kg}$, stiffness, $k = 36.63 \text{ kN/m}$ and damping coefficient, $c = 31.68\text{N-s/m}$. The Simulink program of the BSMC and NNAONFSMC in Figure 5.11 and Figure 5.12.

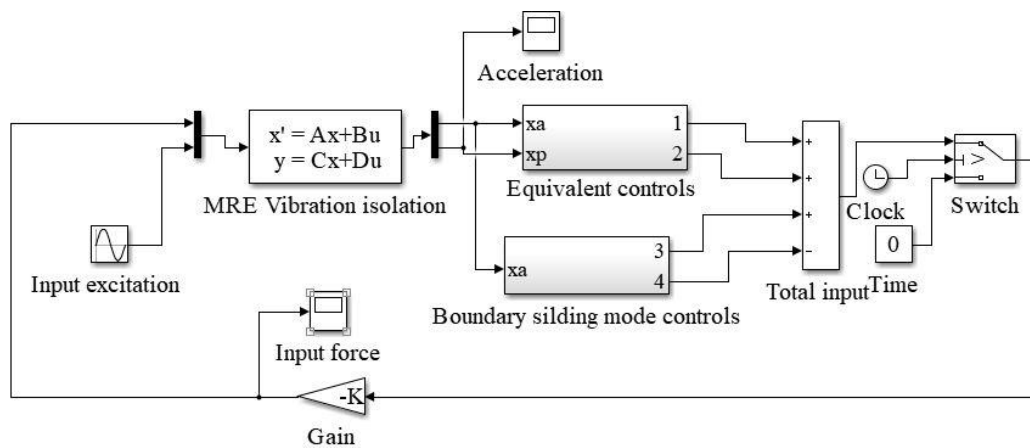


Figure 5.11 Simulink program of BSMC for MRE vibration isolation.

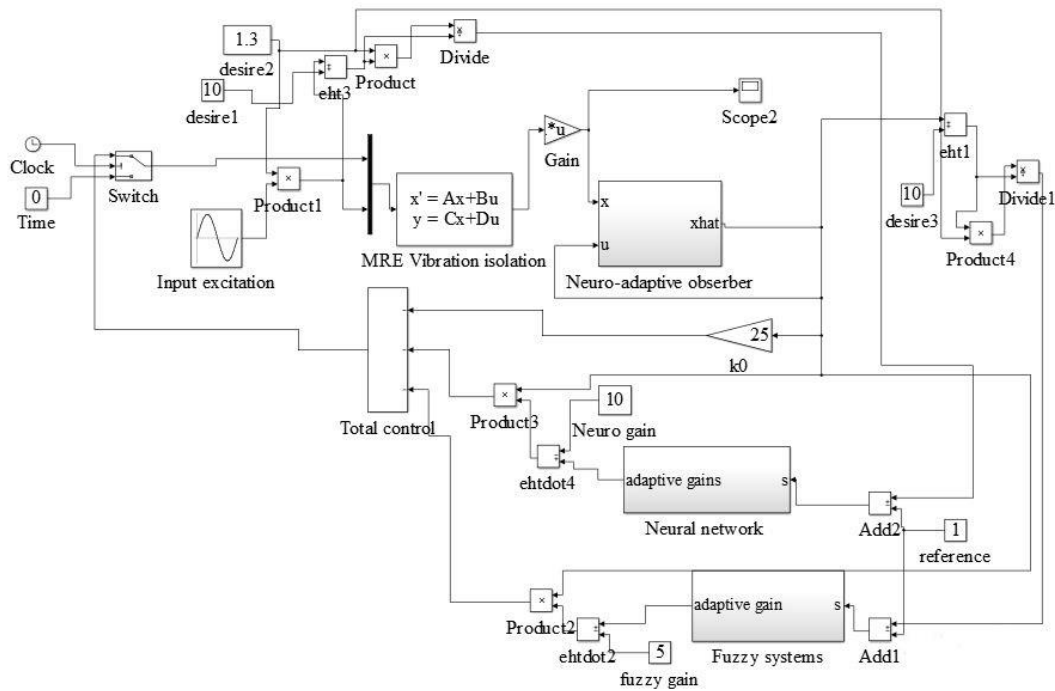


Figure 5.12 Simulink program of NNAONFSMC for MRE vibration isolation.

The controllers are simulated without and with parameter uncertainties for single-frequency excitation. Further, NNAONFSMC is simulated for variable frequency excitation. The gains of the BSMC are presented in Table 5.1.

Table 5.1 Optimal gains of boundary sliding mode control (BSMC).

Frequency (Hz)	λ	η	Φ
34	30	16.8	0.1
36	40	16.8	0.1
38	10	15.2	0.1
40	10	5.72	0.1

The neural network structure of 2-8-1 is used for designing the NNAO and NNAONFSMC. It has displacement and velocity as the two inputs, eight hidden RBF neurons, and one output as adaptive gain. The NNAO estimates the displacement and velocity of the MRE vibration isolation without and with parameter uncertainties. In the case of NNAONFSMC, the proposed neural network structure approximates the

equivalent control. Furthermore, the fuzzy system approximates the switching term with eight gaussian membership functions of the sliding surface, s .

Table 5.2 Parameters of RBF and Gaussian membership function of the neural network and fuzzy system.

Parameters	Number of neurons and membership function							
	1	2	3	4	5	6	7	8
Frequency of excitation (Hz)	38	36	40	34	38	36	40	34
Centers of the neuron for scale displacement, \mathbf{x}_1 and $\hat{\mathbf{x}}_1$	7.76	6.98	6.49	5.94	5.73	4.93	4.67	3.98
Centers of the neuron for scale velocity, \mathbf{x}_1 and $\hat{\mathbf{x}}_2$	1.8	1.5	1.6	1.2	1.3	1.11	1.17	0.85
Width of neurons and membership function, \mathbf{c}_i	0.5	0.35	0.4	0.3	0.3	0.25	0.35	0.5
Centers of input membership function of the sliding surface, s	0.23	0.21	0.213	0.172	0.118	0.15	0.153	0.173

Table 5.3 The adaptive gain and weight of the NNAO and NNAONFSMC.

Parameters	Number of neurons and membership function							
	1	2	3	4	5	6	7	8
Frequency of excitation (Hz)	38	36	40	34	38	36	40	34
Adaptive gains of the observer, β_o	0	200	250	270	285	305	335	330
Weights of the adaptive observer, \mathbf{W}_o	-74.8	-16.83	126.4	-98.84	119.04	22.61	52.79	140.5
Adaptive gains of the controller, β_c	0	-10	20	-45	-20	-50	-5	-35
Weights of the controller, \mathbf{W}_c	-6.80	-2.51	27.31	-49.09	30.72	-65.4	72.35	-19.44
Adaptive gains of the fuzzy system of the controller, γ_c	0	-10	10	-30	-15	-35	-5	-25

The excitation frequencies are varied from 34Hz to 40Hz without and with parameter uncertainties. The parameters for the RBF and membership functions are present in Table 5.2. Simulation is carried out to obtain the optimal gain of the proposed controller. The gains of the NNAO are $k_o = 60$, $\beta_o = 350$ and NNAONFSMC are $\lambda = 150$, $k_o = 50$, $\beta_c = 40$ and $\gamma_c = 70$. The adaptive gain and weight of the NNAO and NNAONFSMC are presented.

5.6.1 Results and Discussion

5.6.1.1 Single-frequency excitation without and with parameter uncertainties

The steady-state frequency of excitation is varied from 34Hz to 40Hz in the step of 2 Hz to simulate the actual frequency shift of MRE vibration isolation in Figure 5.13 to Figure 5.16 depict simulated time response. The simulated time response of the isolation at excitation frequency, 34Hz, is shown in Figure 5.13. The first 10 s are divided into control-off and control-on, where the simulated acceleration values for control-off are 28.91 m/s^2 for BSMC and 28.80 m/s^2 for NNAONFSMC. With control-on, the acceleration reduces to 18.50 m/s^2 for BSMC and 16.81 m/s^2 for NNAONFSMC. The control force of BSMC is 9.92 N, and NNAONFSMC is 10.08 N, as shown in Figure 5.13 (b). The subsequent 10 s of Figure 5.13 (a) portrays the uncertain behavior of MRE vibration isolation. Due to its time-varying properties, the stiffness and damping of the MRE vary, leading to a reduction of acceleration to 19.8 m/s^2 for control-off. For the control-on, the reduction of acceleration is 12.85 m/s^2 for BSMC and 11.94 m/s^2 for NNAONFSMC. The control force for BSMC is 9.18 N, and the NNAONFSMC is 11.06 N, as shown in Figure 5.13 (b). With the time-varying property of the MRE, the control force of BSMC decreases with constant control gains.

On the contrary, in the case of NNAONFSMC, the control force increases owing to its adaptive behavior because the gains vary online as the input parameters changes. This proves that the proposed controller is effective compared to BSMC in the unknown, uncertain behavior of MRE vibration isolation. For example, from Table 5.4 and Table 5.5, it is observed that the maximum reduction of the acceleration is 33.71% for BSMC and 40.15% for NNAONFSMC at the excitation frequency of 34Hz without the parameter uncertainties whereas, with parameter uncertainties, the maximum reduction

of acceleration is 43.64% for BSMC and 52.62% for NNAONFSMC at the excitation frequency of 36Hz.

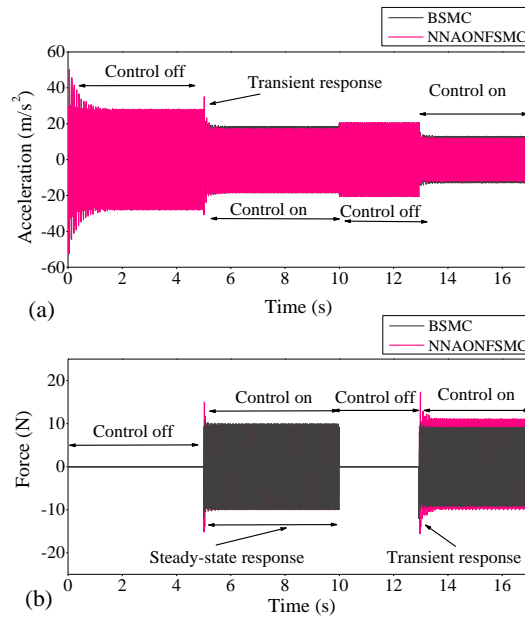


Figure 5.13 Simulated time-responses of excitation frequency at 34 Hz: (a) acceleration and (b) force.

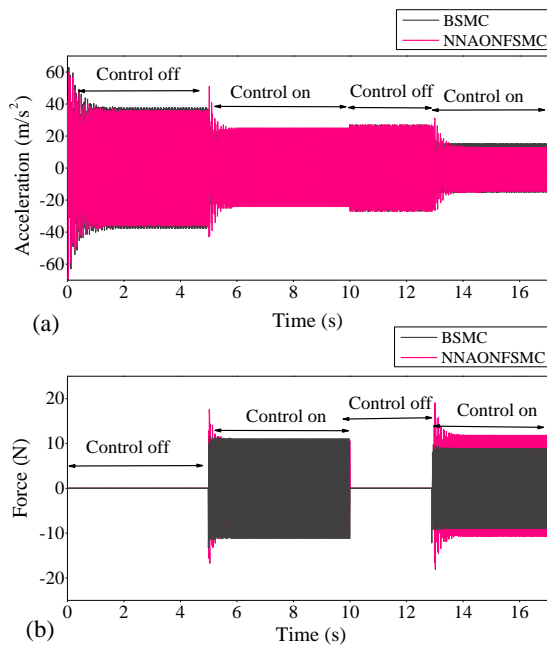


Figure 5.14 Simulated time-responses of excitation frequency at 36 Hz: (a) acceleration and (b) force.

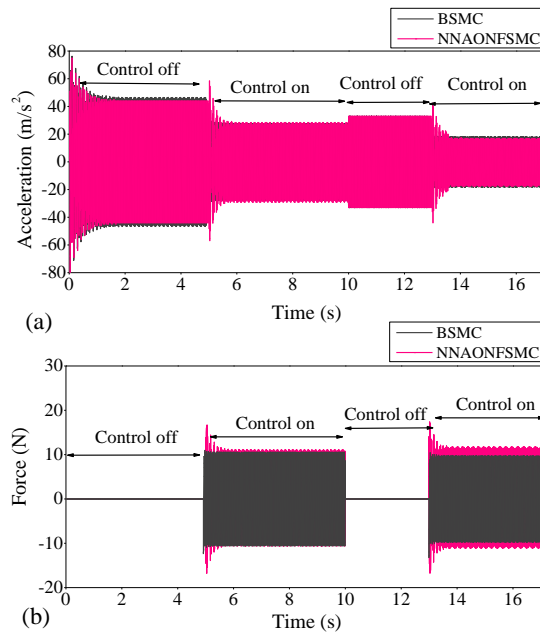


Figure 5.15 Simulated time-responses of excitation frequency at 38 Hz: (a) acceleration and (b) force.

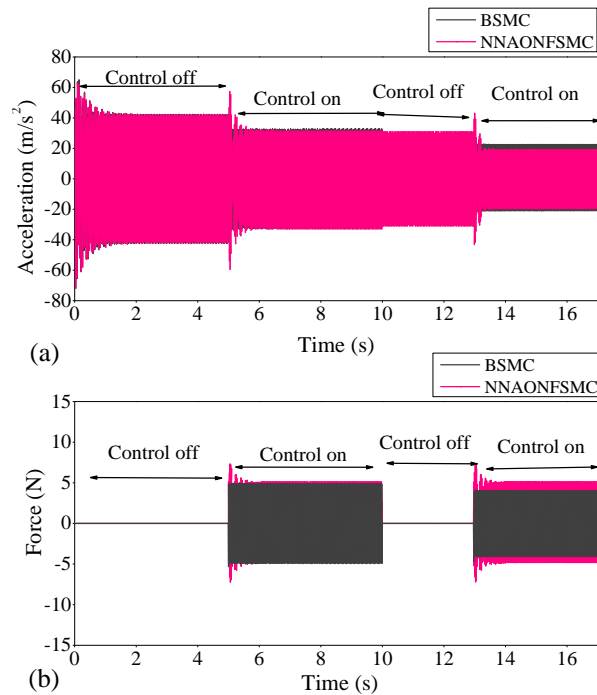


Figure 5.16 Simulated time-responses of excitation frequency at 40 Hz: (a) acceleration and (b) force.

Table 5.4 Simulated results of MRE vibration isolation under different excitation frequencies without parameter uncertainties.

Frequency (Hz)	BSMC				NNAONFSMC			
	$\ddot{x}(m/s^2)$	$\ddot{x}(m/s^2)$	% of	Force	$\ddot{x}(m/s^2)$	$\ddot{x}(m/s^2)$	% of	Force
	Control off	Control on	decrease	(N)	Control off	Control on	decrease	(N)
34	28.91	18.50	33.71	9.92	28.80	16.81	40.15	10.08
36	37.81	24.92	34.09	11.9	37.12	24.91	32.53	11.05
38	46.52	28.13	39.53	10.49	44.12	28.44	35.53	11.09
40	42.21	32.82	21.8	4.84	42.21	32.51	22.25	5.15

Table 5.5 Simulated results of MRE vibration isolation under different excitation frequencies with parameter uncertainties.

Frequency (Hz)	BSMC				NNAONFSMC			
	$\ddot{x}(m/s^2)$	$\ddot{x}(m/s^2)$	%	Force	$\ddot{x}(m/s^2)$	$\ddot{x}(m/s^2)$	%	Force
	Control off	Control on	decrease	(N)	Control off	Control on	decrease	(N)
34	19.8	12.85	35.10	9.18	19.6	11.94	42.22	11.06
36	26.9	15.16	43.64	8.89	27.02	12.8	52.62	11.81
38	33.02	18.28	44.75	10.49	33.02	16.92	48.75	11.72
40	29.92	22.54	24.66	3.80	31.09	17.36	44.16	5.18

5.6.1.2 Simulation of variable frequency excitation

The simulation of the MRE vibration isolation for variable frequency excitation is carried out and time-response is as shown in Figure 5.17.

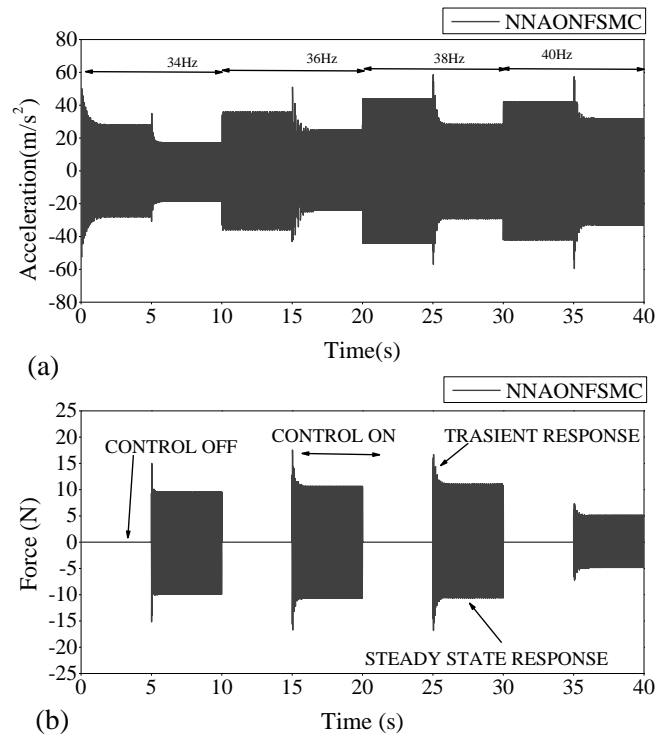


Figure 5.17 Simulated responses at variable frequency excitation: (a) acceleration and (b) force.

As the frequency of excitation varies, the displacement and velocity of MRE vibration isolation also vary. In the proposed NNAONFSMC controller, an adaptive observer-based neural network estimates the displacement and velocity for varying excitation frequency. Further, the adaptive neural network fuzzy sliding mode controller mitigates the amplitudes of vibration. The ability of the observer and the controller to adapt gains online makes the proposed controller useful in variable frequency excitation.

5.7 Experimental Analysis

Experimental setup for the real-time controller of MRE vibration isolation has been discussed in Section 4.8. Optimum gains of the BSMC and NNAONFSMC are computed from the simulation technique as discussed in the preceding section. Furthermore, the computed gains with small manipulation used for the experimental investigation. The LabVIEW programs of BSMC and NNAONFSMC for MRE vibration isolation are shown in Figure 5.18 and Figure 5.19.

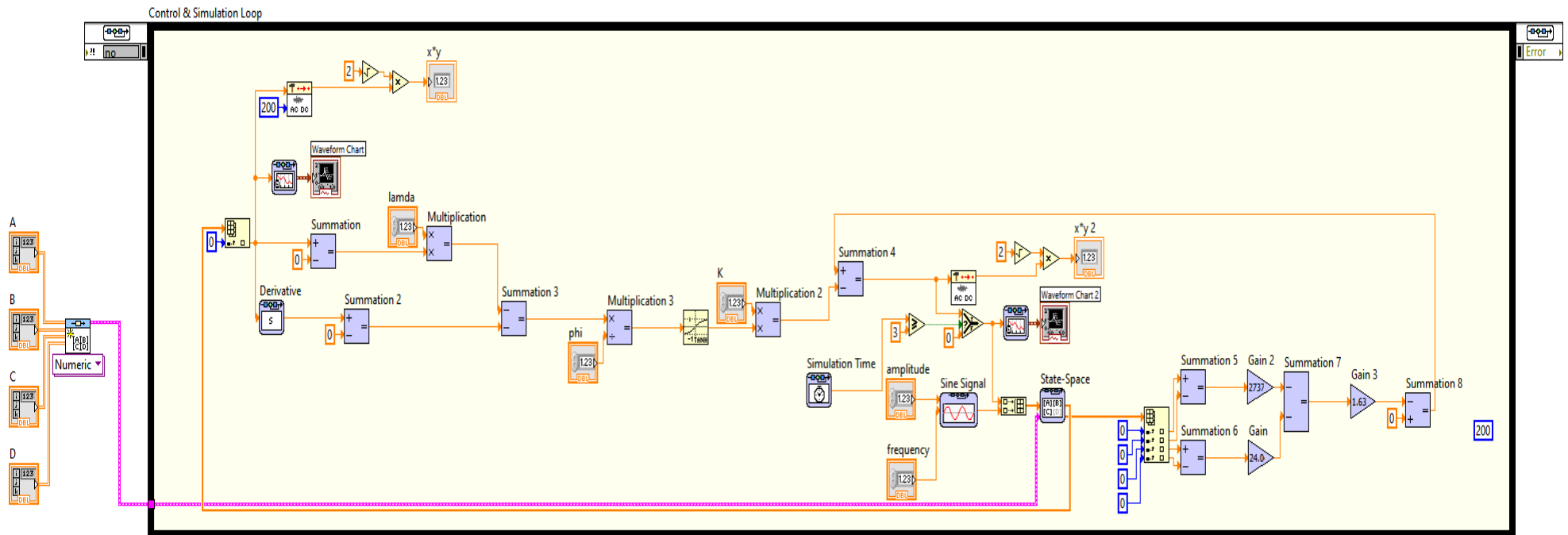


Figure 5.18 LabVIEW program of BSMC for MRE vibration isolation.

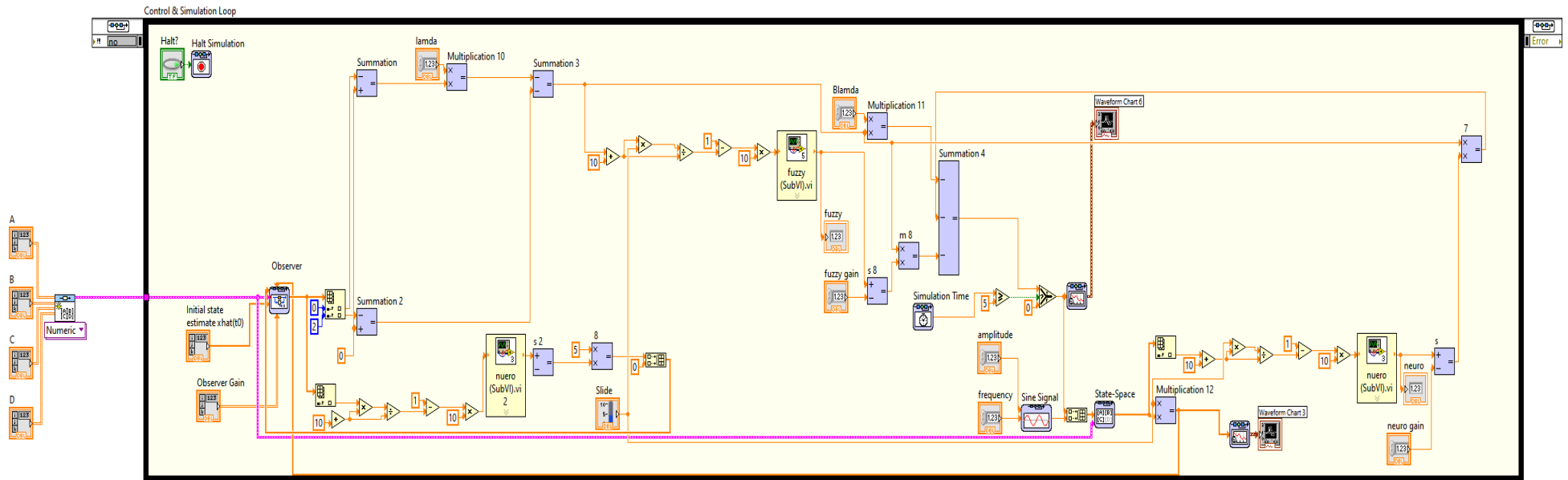


Figure 5.19 LabVIEW program of NNAONFSMC for MRE vibration isolation.

5.7.1 Results and Analysis

5.7.1.1 The experiment of single-frequency excitation without and with parameter uncertainties

The performance of the proposed controllers is investigated experimentally under single frequency excitation, as shown in Figure 5.20 to Figure 5.23. The excitation frequency is varied from 34Hz to 40Hz in the step of 2 Hz. The measured acceleration at a frequency of excitation of 34 Hz is depicted in Figure 5.20 (a). For the first 10 s, the MRE vibration isolation is excited without parameter uncertainties and with parameter uncertainties for the subsequent 10 s, as presented in Figure 5.20 (a). With the control off, the measured acceleration of the MRE vibration isolation is 27.73 m/s^2 and for the controller on, acceleration reduces to 19.9 m/s^2 for BSMC and 18.72 m/s^2 for NNAONFSMC. Also, the corresponding control current is 1.85 A and 2A. Due to the MRE vibration isolation parameter uncertainties, the measured acceleration reduces to 19.25 m/s^2 for control-off. For control-on, the acceleration is 14.91 m/s^2 for BSMC and 13.84 m/s^2 for NNAONFSMC. The current input for BSMC is 1.68 A and 2.08 A for NNAONFSMC. Constant control gains reduce the input current for BSMC. However, in the case of the NNAONFSMC, adaptive gains change online with input variation and increase input current, proving that the effectiveness of NNAONFSMC over BSMC reduces amplitude with parameter uncertainties. The percentage reduction of the acceleration is 13.23 % for BSMC and 20.10 % for NNAONFSMC at the excitation frequency of 40Hz without parameter uncertainties.

Furthermore, with the parameter uncertainties, the percentage reduction is 30.54 % for BSMC and 37.69 % for NNAONFSMC at the excitation frequency, 38Hz. In the absence of parameter uncertainties, the performance of both controllers is comparable. Nevertheless, with parameter uncertainties, the performance of the BSMC deteriorates and is observed in Table 5.6 and Table 5.7.

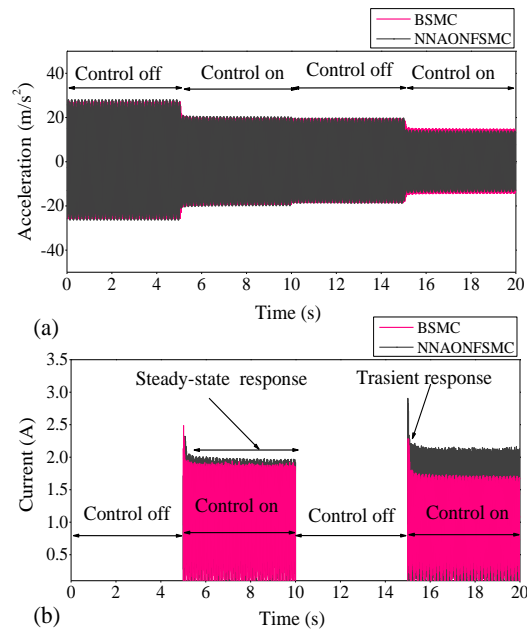


Figure 5.20 Measured time responses at 34 Hz: (a) acceleration and (b) control current.

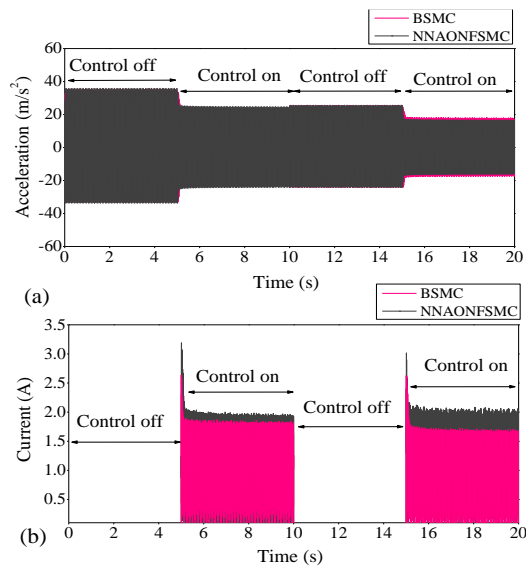


Figure 5.21 Measured time responses at 36 Hz: (a) acceleration and (b) control current.

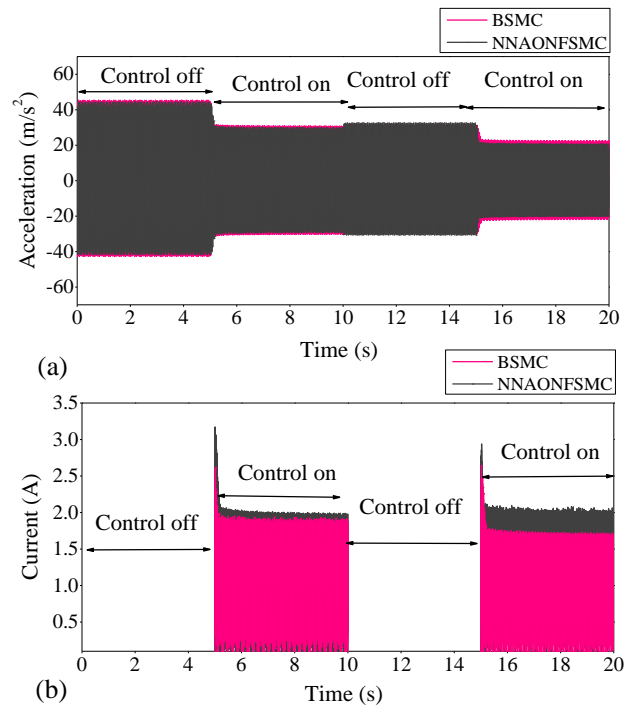


Figure 5.22 Measured time responses at 38 Hz: (a) acceleration and (b) control current.

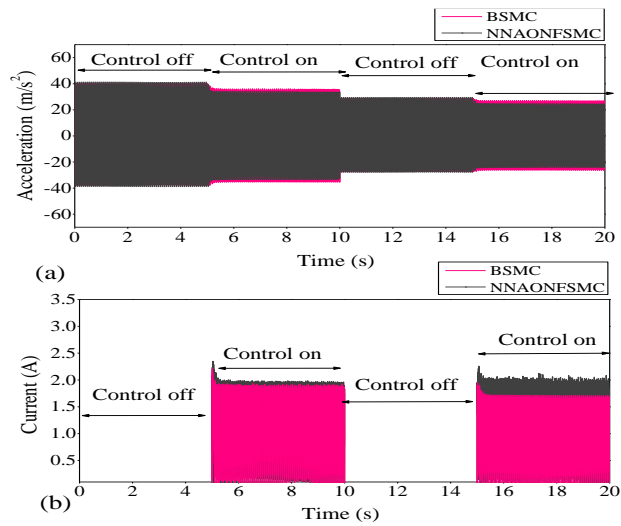


Figure 5.23 Measured time responses at 40 Hz: (a) acceleration and (b) control current.

Table 5.6 Experimental results of MRE vibration isolation under different frequencies without parameter uncertainties.

Frequency (Hz)	BSMC				NNAONFSMC			
	$\ddot{x}(m/s^2)$	$\ddot{x}(m/s^2)$	% of	Control	$\ddot{x}(m/s^2)$	$\ddot{x}(m/s^2)$	% of	Control
	Control off	Control on	decrease	current (A)	Control off	Control on	decreas e	current (A)
34	27.73	18.72	30.99	1.85	27.73	19.09	31.18	2
36	37.75	24.73	34.49	1.84	37.75	24.12	34.54	1.95
38	44.26	30.05	32.10	1.92	43.63	28.99	33.55	1.97
40	41.04	35.61	13.23	1.86	41.94	33.51	20.10	1.98

Table 5.7 Experimental results of MRE vibration isolation under different frequencies with parameter uncertainties.

Frequency (Hz)	BSMC				NNAONFSMC			
	$\ddot{x}(m/s^2)$	$\ddot{x}(m/s^2)$	% of	Control	$\ddot{x}(m/s^2)$	$\ddot{x}(m/s^2)$	% of	Control
	Control off	Control on	decrease	current (A)	Control off	Control on	decrease	current (A)
34	19.26	14.91	22.58	1.68	19.26	13.84	28.14	2.08
36	25.22	18.12	28.15	1.70	25.22	16.71	33.37	2.03
38	32.71	22.72	30.54	1.72	32.71	20.38	37.69	2.06
40	29.53	26.98	8.63	1.70	30.12	23.98	20.38	2.09

5.7.1.2 The experiment of variable frequency excitation

Variation in excitation frequency leads to changes in the acceleration of MRE vibration isolation. Each frequency of excitation needs different controller gains to produce the control current. In those cases, the controllers' gains have to change online to adapt to the variable acceleration. The NNAONFSMC as an adaptive controller was implemented successfully for the variable frequency excitation of MRE vibration isolation. Figure 5.24 shows the measured acceleration and control current of MRE vibration isolation from 34 Hz to 40 Hz for NNAONFSMC. Each frequency is excited for 10 s with control-off and control-on. Due to the adaptive behavior of the controller,

it works for variation of frequency excitation effectively. Table 5.7 present the percentage reduction of individual frequencies.

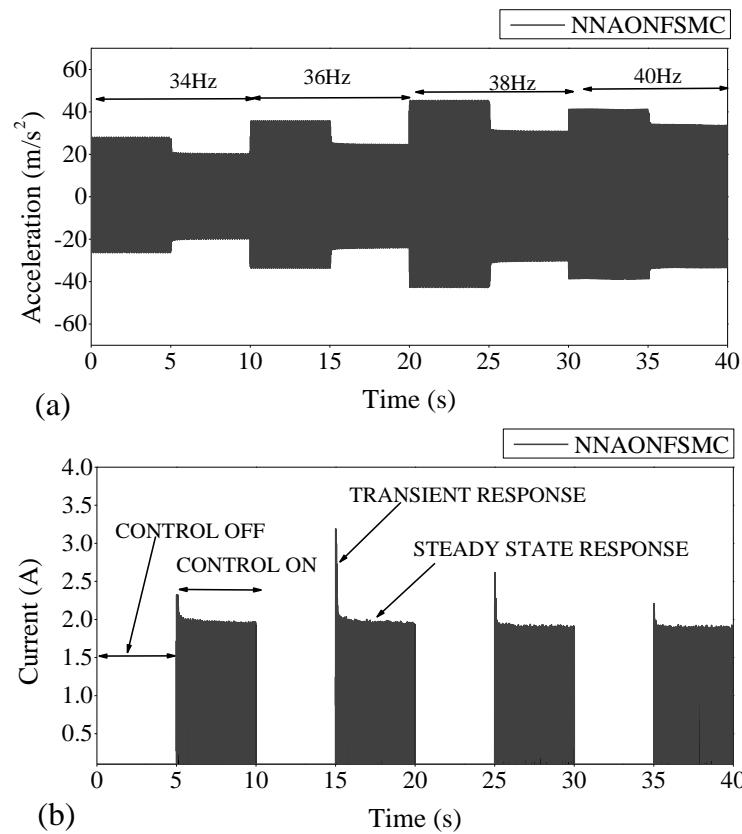


Figure 5.24. Measured responses under variable frequency excitation: (a) acceleration and (b) control current.

5.8 Closure

Numerical and experimental investigation on performance of the neuroadaptive observer-based intelligent nonlinear control MRE vibration isolation have been discussed in this chapter. The boundary sliding mode control (BSMC) and intelligent sliding mode control with nonlinear neural network adaptive observer (NNAONFSMC) have been employed for the MRE vibration isolation having parameter uncertainties and external disturbance. The Lyapunov theory has employed to assess the asymptotical stability of the proposed controllers. The effect of controllers is compared without and with parameter uncertainties of MRE vibration isolation at the single excitation frequency and with parameter uncertainties. The maximum percentage reduction of the measured acceleration is 37%. Further, The NNAONFSMC has been analyzed for

variable excitation frequency, and the maximum percentage reduction of the measured acceleration is 34%. From these outcomes, it is evident that the NNAONFSMC is more effective with time-varying parameter uncertainties of MRE than the BSMC at single and variable frequency excitation. Chapter 6 discuss the investigation on the performance of the model-free adaptive controls for the MRE based Adaptive tuned vibration absorber.

6. Model-Free Adaptive Fuzzy Sliding Mode Control for Magnetorheological Elastomer-based Adaptive Tuned Vibration Absorber

6.1 Introduction

This chapter discusses the performance of the model-free adaptive controls for the Magnetorheological elastomer-based Adaptive tuned vibration absorber (MRE ATVA). The MRE ATVA is fabricated with anisotropic MRE. The dynamic properties of the MRE ATVA are extracted from the frequency shift plot. The performance of proposed controls that is sliding mode control and model-free adaptive fuzzy sliding mode control, are investigated under single frequency and variable frequency excitation.

6.2 Dynamic Vibration Absorber (DVA)

Dynamic vibration absorber is one of the most effective methods of vibration control invented by Frahm (1909)(Xu et al. 2010)(Liao et al. 2014). The vibration absorber is mostly used on the machine, transmission lines, and reciprocating tools to prevent the failure of these systems (Deng and Gong 2007). Unlike the vibration isolator, an absorber includes an auxiliary mass-spring system to protect the primary system. The addition of the auxiliary device to the primary system converts the entire system from a single degree of freedom system to a multi or two degrees of freedom system. The new system possesses two natural frequencies. The auxiliary device is also known as a vibration absorber. The amplitude of the vibrating primary system reduces by keeping the natural frequency of vibration absorber same as of operating frequency. However, traditional dynamic vibration absorbers work for the narrow frequency range due to its constant properties. If the operating frequency varies, the absorber proves to be ineffective (Yang et al. 2014). The problem associated with traditional dynamic vibration absorbers can be overcome using MRE based Adaptive tuned vibration absorber. MRE is smart material changes dynamic properties under the influence of the magnetic field. These properties of MRE are very effective in reducing the vibrating

amplitude of the system by shifting the natural frequency of MRE ATVA to operating frequency in a wide operating frequency range.

6.2.1 Transmissibility Dynamic Vibration Absorber

Figure 6.1. Schematic of dynamic vibration absorber. The dynamic vibration absorber is subjected to a steady-state excitation force, $f(t)=F_0 \sin (\omega t)$.

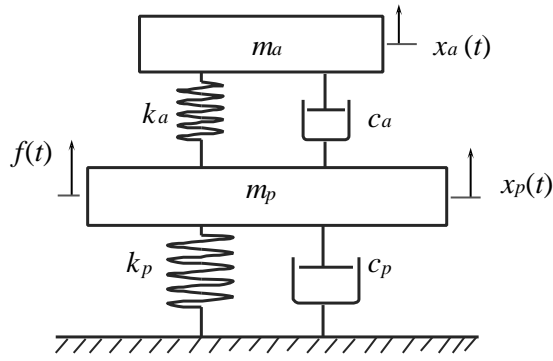


Figure 6.1. Schematic of dynamic vibration absorber.

The governing differential equations of dynamic vibration absorber are given as

$$m_p \ddot{x}_p(t) + k_p x_p(t) + c_p \dot{x}_p + k_p (x_p(t) - x_a(t)) + c_p (\dot{x}_p(t) - \dot{x}_a(t)) = f(t) \quad (6.1)$$

$$m_a \ddot{x}_a(t) + k_a (x_a(t) - x_p(t)) + c_p (\dot{x}_a(t) - \dot{x}_p(t)) = 0 \quad (6.2)$$

where m , k and c are the mass, stiffness and damping coefficient, respectively. $x(t)$ represents the displacement of the mass at a given time, t . The suffixes, p and a correspond to the primary mass and absorber, respectively.

Assuming the general solutions for Equations ((6.1) and (6.2) as (Kumbhar et al. 2018).

$$x_p = X_p e^{i\omega t} \quad (6.3)$$

$$x_a = X_a e^{i\omega t} \quad (6.4)$$

The amplitudes of vibration are given

$$X_p = \frac{[(k_a - m_a \omega^2) + c_a \omega j] F_0}{[(k_p - m_p \omega^2)(k_a - m_a \omega^2) - m_a k_a \omega^2] + [k_p - (m_p + m_a) \omega^2] c_a \omega j} \quad (6.5)$$

$$X_a = \frac{[k_a + c_a \omega j] F_0}{[(k_p - m_p \omega^2)(k_a - m_a \omega^2) - m_a k_a \omega^2] + [k_p - (m_p + m_a) \omega^2] c_a \omega j} \quad (6.6)$$

Where, ω , the excitation frequency and j is the complex variable.

The static displacement of the primary mass is given by

$$X_{st} = \frac{F_0}{k} \quad (6.7)$$

The transmissibility of the primary mass and absorber is obtained by dividing the Equation (6.5),(6.6) and from Equation (6.7), yields.

$$\frac{X_p}{X_{st}} = \sqrt{\frac{(2\zeta r)^2 + (r^2 - \beta^2)^2}{(2\zeta r)^2(r^2 - 1 + \mu r^2) + [\mu r^2 \beta^2 - (r^2 - 1)(r^2 - \beta^2)]^2}} \quad (6.8)$$

$$\frac{X_a}{X_{st}} = \sqrt{\frac{(2\zeta r)^2 + \beta^4}{(2\zeta r)^2(r^2 - 1 + \mu r^2) + [\mu r^2 \beta^2 - (r^2 - 1)(r^2 - \beta^2)]^2}} \quad (6.9)$$

where the natural frequency of absorber, $\omega_a = \sqrt{\frac{k_a}{m_a}}$, the natural frequency of the

primary mass without absorber, $\omega_p = \sqrt{\frac{k_p}{m_p}}$, frequency ratio, $r = \frac{\omega}{\omega_p}$, the ratio of

natural frequencies, $\beta = \frac{\omega_a}{\omega_p}$, mass ratio, $\mu = \frac{m_a}{m_p}$, and ζ is the damping factor.

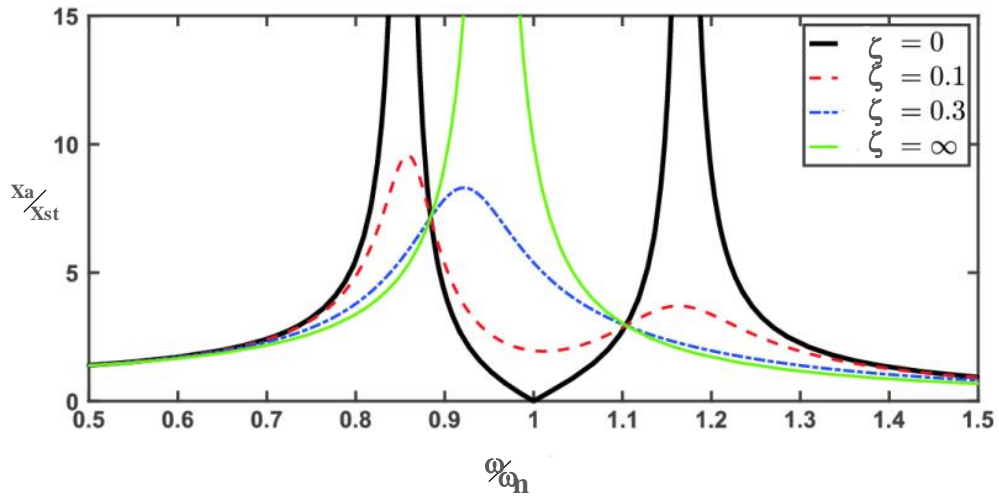


Figure 6.2 Plot: Frequency ratio vs. transmissibility ratio of the primary system.

The natural frequency of the absorber has to be the same as the natural frequency of the primary system for the effective reduction of the amplitude of the primary system. Damping factor of the vibration absorber influence the amplitude reduction of the

primary system. For zero damping, the vibration amplitude of the primary system is zero at a frequency ratio of 1 and infinite at a frequency ratio of 0.85 and 1.8. This shows that small changes in the variation of operating frequency lead to the infinite amplitude of vibration, subsequently the failure of both systems. For the vibration absorber with a damping factor other than 0, the vibration amplitude of the primary system is unexpectable range shown in Figure 6.2. Thus, MRE based vibration absorber overcomes the disadvantages of the traditional dynamic vibration absorbers.

6.3 Magnetorheological Elastomer-based Adaptive Tuned Vibration Absorber (MRE ATVA)

The proposed adaptive tuned vibration absorber device based on MRE has been discussed in the following sections.

6.3.1 Preparation of Magnetorheological Elastomer

The constituents of the anisotropic magnetorheological elastomer include room temperature vulcanization (RTV) based silicone rubber (Performance Polymers, MoldSil 102LL with CAT 9,) with Carbonyl iron particles (BASF, Type CN, Average diameter-5 μ m) as its filler material. The volume fraction of the iron particles is 27 %. The MRE sample is prepared with thorough mixing of silicone rubber and carbonyl iron. Silicone oil is added to the mixture about 10 % of weight to reduce the zero-field stiffness of MRE. The prepared mixture is poured into a mold of size 25 \times 25 \times 3 mm and degassed in a vacuum chamber. Further, the sample is cured 24 hours at room temperature, 24 $^{\circ}$ C with a 0.7 T magnetic field to obtain the anisotropic MRE.

6.3.2 Fabrication of MRE ATVA

Figure 6.3 shows the developed MRE ATVA. It consists of two MRE samples arranged to act in a double lap shear mode with a mass of 1.57 kg. The MRE samples are fixed between the absorber mass and the electromagnet, as shown in Figure 6.3(a). The electromagnet consists of a copper wire of wire gauge AWG18. The number of turns is 2400 with an inductance of 153 mH and a resistance, 10.2 Ω . The magnetic field is controlled with an external DC power supply. For electromagnet, the magnetic field of 0.66 T is achieved with the current of 5 A.

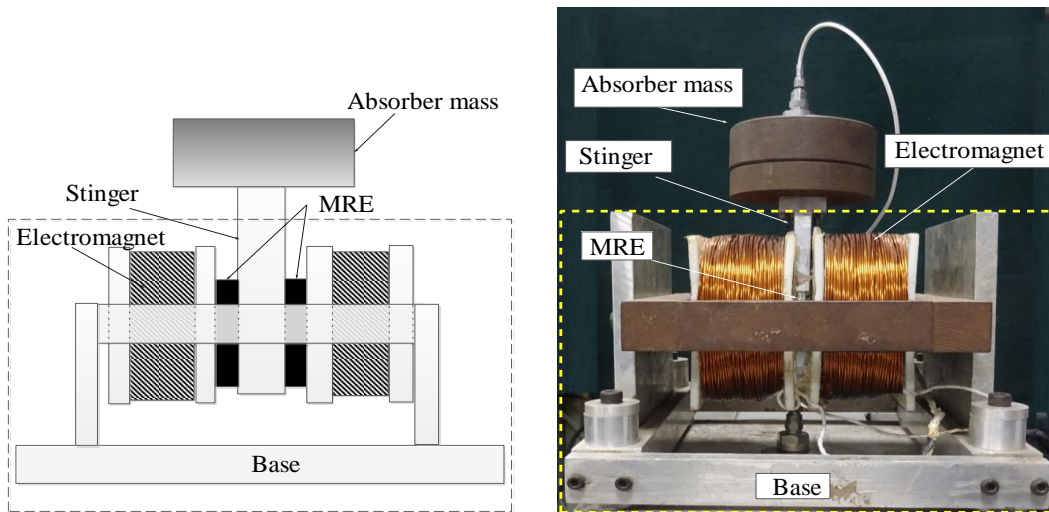


Figure 6.3 MRE ATVA: (a) schematic and (b) photograph.

6.3.3 Frequency Shift of MRE ATVA

To extract the dynamic properties of the MRE ATVA, it is subjected to steady-state excitation from 10 Hz to 80 Hz in the step of 1 Hz at constant input acceleration. The peak amplitude of each frequency is recorded.

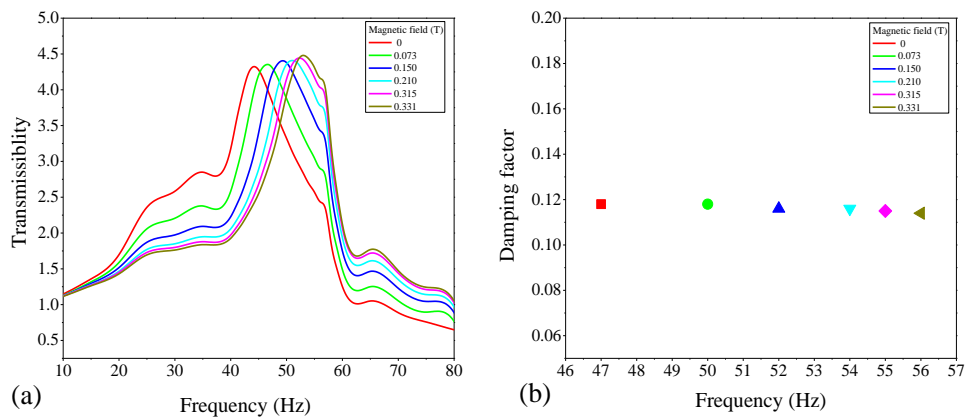


Figure 6.4 Plots of frequency shift of MRE ATVA: (a) transmissibility vs. frequency and (b) damping factor vs. frequency.

The field-dependent variations in the transmissibility and damping factor with varying frequencies are plotted as shown in Figure 6.4. It is observed that the natural frequency of the MRE ATVA increases from 47 Hz to 56 Hz under the magnetic field of 0.315 T.

The increase in the natural frequency, as shown in Figure 6.4 (a), is attributed to the field-dependent increase in the stiffness of the MRE under the influence of the magnetic field. In the presence of a magnetic field, the carbonyl iron particles align themselves in the direction of the applied field. This results in the formation of magnetic dipoles between adjacent carbonyl iron particles, which induces compressive forces on the interlaying matrix, increasing the stiffness of MRE. It is also observed from Figure 6.4 (b) that there is no significant variation in the damping factor with a variable magnetic field. The field-dependent dynamic properties of MRE ATVA are presented in Table 6.1.

Table 6.1 Dynamic properties of MRE ATVA for variable magnetic field.

Current (A)	Voltage (V)	Magnetic Field (T)	Frequency (Hz)	Stiffness (N/m)	Damping Coefficient (N-s/m)	Damping factor
0	0	0	47	136916.2	109.41	0.118
0.5	5.32	0.073	50	154952.7	116.40	0.118
1	10.64	0.150	52	167596.9	119.00	0.116
1.5	15.96	0.210	54	180736.9	123.58	0.116
2	21.23	0.315	55	187492.8	124.48	0.115
2.5	26.6	0.331	56	194372.7	125.95	0.114

The experimental set-up of the combined system is as shown in Figure 6.5. It consists of a primary mass and MRE ATVA. The primary mass of 9.35 kg and MRE-based ATVA is mounted at the center of the massless beam with fixed-fixed end conditions. A mass ratio of 0.18 is maintained between the primary and the absorber mass. An electromagnetic shaker (Make: Vibration Test System; Type VTS-80) is used to excite the combined system through a power amplifier (Make: Techron; Type 5507). Input frequencies are generated through a function generator (Make: Agilent; Type 33220A). Accelerometers (Make: Kistler; Type K-shear) are mounted on the primary and the absorber mass to measure the accelerations signals. The signals are acquired using a data acquisition module (National Instruments, Type NI-9234) which is further processed using LabVIEW-(Version 2016). The magnetic field is induced in the electromagnet via a DC power supply (Make: Ametek; Type XG150-5.6).

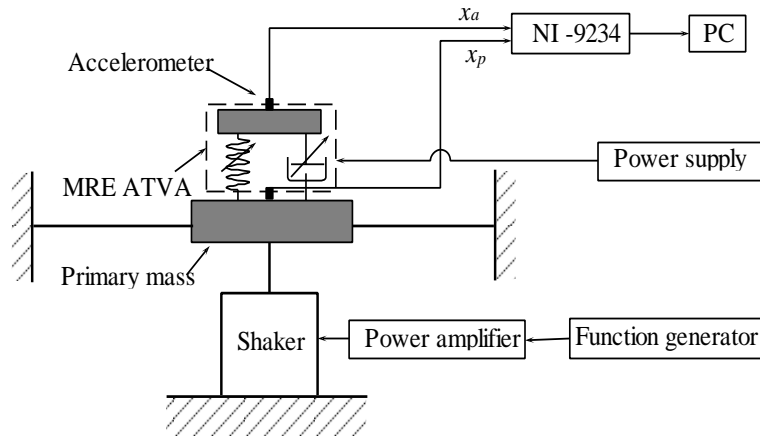


Figure 6.5 Schematic of the combined system (primary mass and MRE ATVA).

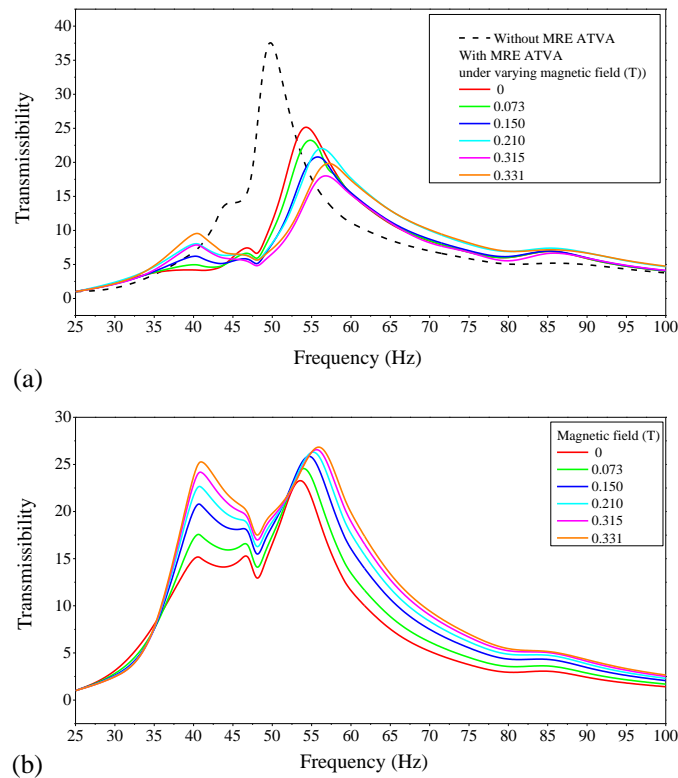


Figure 6.6 Plot of transmissibility vs. frequency: (a) primary mass and (b) MRE ATVA.

Field-dependent variations in the peak accelerations are obtained for the combined system under steady-state sweep from 25 Hz to 100 Hz at constant input acceleration. Figure 6.6 depicts the measured transmissibility of primary mass and MRE ATVA. The natural frequency of primary mass without MRE ATVA is 50 Hz. It is observed that

the natural frequency of primary mass shifts to two new component frequencies with the addition of the MRE ATVA. Further, the maximum amplitudes of the primary mass decrease with an increase in the magnetic field.

6.4 System Dynamics of MRE ATVA

To simulation of the controllers requires a thorough understanding of the system dynamic. The following section discusses the dynamic of the MRE adaptive tuned vibration absorber, the state-space equations and the design of nonlinear and adaptive controllers.

6.4.1 MRE ATVA as Two Degrees of Freedom System

MRE-based adaptive tuned vibration absorber is considered as a two-degree freedom system to derive the state-space equation, as shown in Figure 6.7.

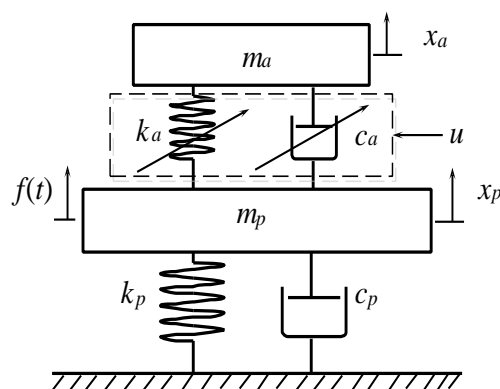


Figure 6.7 Schematic of MRE ATVA with control input.

The governing differential equation of MRE ATVA and primary system is written as,

$$m_a \ddot{x}_a + k_a(x_a - x_p) + c_a(\dot{x}_a - \dot{x}_p) = -u \quad (6.10)$$

$$m_p \ddot{x}_p + k_p x_p + c_p \dot{x}_p + k_p(x_p - x_a) + c_p(\dot{x}_p - \dot{x}_a) = u + f(t) \quad (6.11)$$

where, m_a , k_a and c_a are the mass, stiffness and damping coefficient of the MRE ATVA. m_p , k_p and c_p are the mass, stiffness and damping coefficient of the primary system, respectively. x_a is the displacement of the MRE ATVA, x_p is the displacement of the primary system and both are a function of time, t . u is the control input and $f(t)$ is the excitation.

6.4.2 State-Space Equation of MRE ATVA

Equations (6.10) and (6.11) has been used to derive the state space equation of MRE ATVA. It is expressed (Nise 2011) as

$$\dot{x}(t) = Ax(t) + Bu(t) \quad (6.12)$$

$$y(t) = Cx(t) + Du(t) \quad (6.13)$$

where, x is the state vector, y is the output vector, u is the control input, A is the system matrix, B is the input matrix, C is the output matrix and D is the feedforward matrix. The dot indicates first derivative of time, t . These vectors and matrices are of form;

$$\dot{x}(t) = \begin{bmatrix} \dot{x}_p \\ \dot{x}_a \\ \dot{v}_p \\ \dot{v}_a \end{bmatrix}, x(t) = \begin{bmatrix} x_p \\ x_a \\ v_p \\ v_a \end{bmatrix}, u(t) = \begin{bmatrix} f(t) \\ u \end{bmatrix}$$

$$A = \begin{bmatrix} 0 & 0 & 1 & 0 \\ 0 & 0 & 0 & 1 \\ -\frac{(k_p + k_a)}{m_p} & \frac{k_a}{m_p} & -\frac{(k_p + c_a)}{m_p} & \frac{c_a}{m_p} \\ \frac{k_a}{m_a} & -\frac{k_a}{m_a} & \frac{c_a}{m_a} & -\frac{c_a}{m_a} \end{bmatrix}, B = \begin{bmatrix} 0 & 0 \\ 0 & 0 \\ \frac{1}{m_p} & 0 \\ 0 & -\frac{1}{m_a} \end{bmatrix},$$

$$C = \begin{bmatrix} 1 & 0 & 0 & 0 \\ 0 & 1 & 0 & 0 \end{bmatrix} \text{ and } D = \begin{bmatrix} 0 & 0 \\ 0 & 0 \end{bmatrix}$$

6.5 Design of Controllers

6.5.1 Boundary Layer Sliding Mode Control.

The dynamic governing equation of primary mass with the parameter uncertainties, external disturbance, and control input is given by

$$m_p \ddot{x}_p + k_p x_p + c_p \dot{x}_p + k_p (x_p - x_a) + c_p (\dot{x}_p - \dot{x}_a) = u + dt \quad (6.14)$$

where, u is the control input, and dt is the time-dependent disturbance with known upper bond, D , i.e., $|dt| \leq D$.

By rearranging the equation (6.14), we have the acceleration of the primary mass as

$$\ddot{x}_p = f(x, t) + u + dt \quad (6.15)$$

where, $f(x, t) = -m_p^{-1}(k_p x_p + c_p \dot{x}_p + k_a(x_p - x_a) + c_a(\dot{x}_p - \dot{x}_a))$.

The total control input of the MRE ATVA, u is expressed as

$$u = u_{eq} + u_s \quad (6.16)$$

where u_{eq} is the equivalent control and u_s is the switching control.

The sliding surface s is defined as,

$$s = -\lambda e - \dot{e} \quad (6.17)$$

where error signal, e represents the difference between desired, x_{pd} and actual displacement, x_p of primary mass, i.e., $e = (x_{pd} - x_p)$ and λ is the positive constant.

The objective of the sliding mode control is to ensure the error, $e = 0$. This can be guaranteed by forcing the state trajectory towards the sliding surface (Parameswaran et al., 2015).

Differentiating equation (6.17) with respect to time, t and utilizing the equations (6.15) and e yields,

$$\dot{s} = -\lambda \dot{e} - \ddot{x}_{pd} + f(x, t) + u + dt \quad (6.18)$$

To attain the desired state trajectory without considering uncertainty and disturbance the equivalent control, u_{eq} is determined by equating equation (6.18) to zero. Thus, we have,

$$u_{eq} = \lambda \dot{e} + \ddot{x}_{pd} - f(x, t) - dt \quad (6.19)$$

However, to attain the desired state trajectory with disturbances or uncertainties in the system, the equivalent control effort, u_{eq} do not confirm better performance and leads to instability. Therefore, the auxiliary control must be considered to stabilize system (Vijay and Jena 2017). The total control with auxiliary control is given by

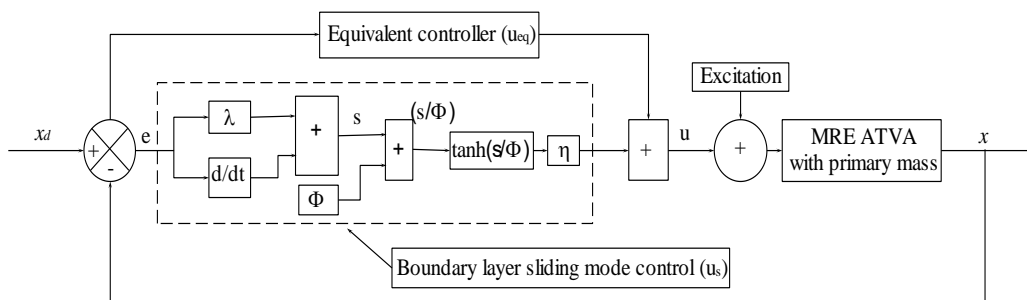


Figure 6.8 Schematic of boundary layer sliding mode control.

$$u = \lambda \dot{e} + \ddot{x}_{pd} - f(x, t) + u_s \quad (6.20)$$

where, $u_s = -\eta \text{sign}(s)$ and η is the positive constant.

The zero error for the state trajectory with disturbances or uncertainties in the system is ensured with the following condition.

$$s \dot{s} = s u_s = s [-\eta \text{sign}(s)] = -\eta |s| \leq 0 \quad (6.21)$$

Sliding mode control is a discontinuous control in which chattering is inherently present and leads to fluctuation in the control output. The boundary layer method is considered to reduce the chattering effect. Further, the discontinuous function changes to smooth saturation function near to a significant region of the switching surface. The relation for the boundary layer is given by [27]

$$B(t) = \{x: |s(x, t)| \leq \Phi\} \quad (6.22)$$

where, Φ is the boundary layer thickness.

With the inclusion of the boundary layer, the total control input as shown in Figure 6.8 can be expressed as,

$$u = \lambda \dot{e} + \ddot{x}_{pd} - f(x, t) - \eta \text{sat}(s/\Phi) \quad (6.23)$$

where the saturation function is given by (Parameswaran et al. 2015)

$$\text{sat}\left(\frac{s}{\Phi}\right) = \begin{cases} \tanh\left(\frac{s}{\Phi}\right), & \text{for } \left|\frac{s}{\Phi}\right| \geq 1 \\ \frac{s}{\Phi}, & \text{for } \left|\frac{s}{\Phi}\right| \leq 1 \end{cases} \quad (6.24)$$

6.5.2 Fuzzy Logic System

In general, the fuzzy system works on the principle of universal approximation theorem (Feng et al., 2017), and any nonlinear function can be approximated by using fuzzy systems. A fuzzy system consists of fuzzy if-then rules and is expressed as

$$R^{(j)}: \text{If } x_1 \text{ is } F_1^j \text{ and } x_n \text{ is } F_n^j \text{ then } y \text{ is } B^j \quad (6.25)$$

where x_1 and y are input and out variables. F_1^j and B^j Fuzzy sets. With center-average defuzzification, product inference and single value fuzzification, the output of the fuzzy is written as (Wang et al. 2001b),

$$y(x) = \frac{\sum_{j=1}^l y^j (\prod_{i=1}^n \mu_{F_i^j}(x_i))}{\sum_{j=1}^l \prod_{i=1}^n \mu_{F_i^j}(x_i)} \quad (6.26)$$

where $\mu_{F_i^j}(x_i)$ is the membership function of the input variable x_i and y^l represents a crisp value at which the membership function μ_{B_j} for fuzzy output, the set reaches its maximum value, which is assumed as $\mu_{B_j}(y^l = 1)$.

By introducing the concept of basic fuzzy function $\xi(x)$, the output of the fuzzy system is given by (Wang et al. 2001a)

$$y(x) = \theta^T \xi(x) \quad (6.27)$$

where, $\theta = (y^1, \dots, y^l)^T, \xi(x) = (\xi^1(x), \dots, \xi^l(x))^T$ and

$$\xi^j(x) = \frac{\prod_{i=1}^n \mu_{F_i^j}(x_i)}{\sum_{j=1}^l \prod_{i=1}^n \mu_{F_i^j}(x_i)} \quad (6.28)$$

The fuzzy membership functions for the equivalent control is given by

$$\mu_{NM}(x_i) = \exp - \left(\frac{x_i + \pi/6}{\pi/24} \right)^2, \mu_{NS}(x_i) = \exp - \left(\frac{x_i + \pi/12}{\pi/24} \right)^2,$$

$$\mu_Z(x_i) = \exp - \left(\frac{x_i}{\pi/12} \right)^2,$$

$$\mu_{PS}(x_i) = \exp - \left(\frac{x_i - \pi/12}{\pi/24} \right)^2 \text{ and } \mu_{PM}(x_i) = \exp - \left(\frac{x_i - \pi/6}{\pi/24} \right)^2$$

and also, the membership functions of switching control is given by

$$\mu_N(s) = \frac{1}{1 + \exp(5(s + 3))}$$

$$\mu_Z(s) = \exp(-s^2) \text{ and}$$

$$\mu_P(s) = \frac{1}{1 + \exp(-5(s - 3))}$$

To approximate the equivalent control $\hat{f}(x|\theta_f)$ and switching control $\hat{h}(s|\theta_h)$ for MRE ATVA with parameter uncertainties and variable frequency excitation, a total of 20 fuzzy rules are considered.

6.5.2.1 Adaptive fuzzy sliding mode control (AFSC)

The developed control in Equation (6.23) does not work if the upper bound of $f(x, t)$ and dt are unknown, for which the fuzzy systems are used to approximate $f(x, t)$ and $\eta \text{sign}(s/\Phi)$ as $\hat{f}(x|\theta_f)$ and $\hat{h}(s|\theta_h)$ as shown in Figure 6.9.

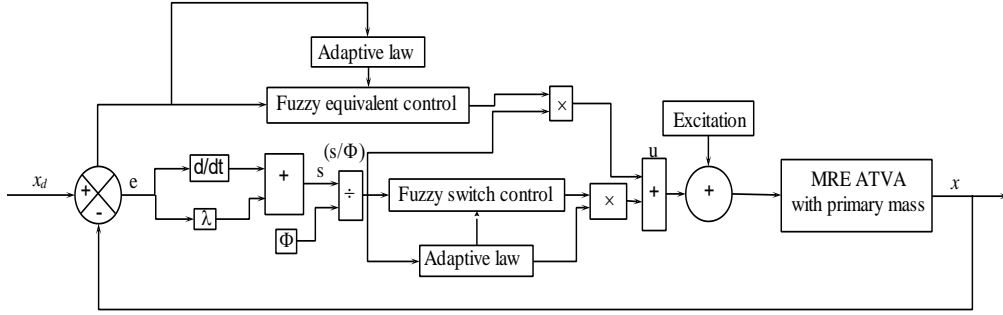


Figure 6.9 Schematic of adaptive fuzzy sliding mode control.

The total control input of the adaptive fuzzy sliding mode control is given by

$$u = \lambda \dot{e} + \ddot{x}_{pd} - \hat{f}(x|\theta_f) - \hat{h}(s|\theta_h) \quad (6.29)$$

where $\hat{f}(x|\theta_f) = \theta_f^T \xi(x)$ and $\hat{h}(s|\theta_h) = \theta_h^T \phi(s)$.

To define the optimal parameters of the fuzzy system, the following conditions should satisfy.

$$\theta_f^* = \arg \min_{\theta_f \in \Omega_f} \left[\sup_{x \in R^n} |\hat{f}(x|\theta_f) - f(x, t)| \right] \quad (6.30)$$

$$\theta_h^* = \arg \min_{\theta_h \in \Omega_h} \left[\sup_{s \in R^n} |\hat{h}(s|\theta_h) - \eta \text{sign}(s/\Phi)| \right] \quad (6.31)$$

where Ω_f and Ω_h are constraint sets for θ_f and θ_h , respectively

The minimum approximation error is given by

$$\omega = f(x, t) - \hat{f}(x|\theta_f) \quad (6.32)$$

Considering the equation (14)

$$\dot{s} = -\lambda \dot{e} - \ddot{x}_{pd} + f(x, t) + u + dt \quad (6.33)$$

$$= f(x, t) - \hat{f}(x|\theta_f) - \hat{h}(s) + dt \quad (6.34)$$

$$= \hat{f}(x|\theta_f^*) - \hat{f}(x|\theta_f) + f(x, t) - \hat{f}(x|\theta_f^*) + \hat{h}(s|\theta_h^*) - \hat{h}(s) - \hat{h}(s|\theta_h^*) + dt \quad (6.35)$$

$$= \hat{f}(x|\theta_f^*) - \hat{f}(x|\theta_f) + \hat{h}(s|\theta_h^*) - \hat{h}(s) + \omega - \hat{h}(s|\theta_h^*) + dt \quad (6.36)$$

$$= \varphi_f^T \xi(x) + \varphi_h^T \phi(s) + dt + \omega - \hat{h}(s|\theta_h^*) \quad (6.37)$$

where, $\varphi_f = \theta_f - \theta_f^*$ and $\varphi_h = \theta_h - \theta_h^*$.

Now consider Lyapunov function candidate of the form

$$V = \frac{1}{2}s^2 + \frac{1}{2\gamma_1}\varphi_f^T\varphi_f + \frac{1}{2\gamma_2}\varphi_h^T\varphi_h \quad (6.38)$$

where γ_1 and γ_2 are positive constants. The time derivative of V is given by

$$\dot{V} = s\dot{s} + \frac{1}{\gamma_1}\varphi_f^T\dot{\varphi}_f + \frac{1}{\gamma_2}\varphi_h^T\dot{\varphi}_h \quad (6.39)$$

$$= s\left(\varphi_f^T\xi(x) + \varphi_h^T\phi(s) + dt + \omega - \hat{h}(s|\theta_h^*)\right) + \frac{1}{\gamma_1}\varphi_f^T\dot{\varphi}_f + \frac{1}{\gamma_2}\varphi_h^T\dot{\varphi}_h \quad (6.40)$$

$$= s\varphi_f^T\xi(x) + \frac{1}{\gamma_1}\varphi_f^T\dot{\varphi}_f + s\varphi_h^T\phi(s) + \frac{1}{\gamma_2}\varphi_h^T\dot{\varphi}_h + s(dt - \hat{h}(s|\theta_h^*) + s\omega) \quad (6.41)$$

$$\dot{V} \leq \varphi_f^T\xi(x) + \frac{1}{\gamma_1}\varphi_f^T\dot{\varphi}_f + s\varphi_h^T\phi(s) + \frac{1}{\gamma_2}\varphi_h^T\dot{\varphi}_h + sdt - s(D + \eta_\Delta \text{sign}(s)) + s\omega \quad (6.42)$$

Finally, the time derivative of the Lyapunov function candidate, we have

$$\dot{V} < \frac{1}{\gamma_1}\varphi_f^T(\gamma_1 s\xi(x) + \dot{\varphi}_f) + \frac{1}{\gamma_2}\varphi_h^T(\gamma_2 s\phi(s) + \dot{\varphi}_h) + s\omega - |s|\eta \quad (6.43)$$

where $\dot{\varphi}_f = -\dot{\theta}_f$, $\dot{\varphi}_h = -\dot{\theta}_h$

Simplification of Equation (6.43) yields

$$\dot{V} \leq s\omega - |s|\eta \leq 0 \quad (6.44)$$

With fuzzy approximation, the minimum approximation error, ω can be achieved with the adaptive fuzzy system. Equation (6.44) implies that \dot{V} is negative semidefinite and all the signals of the control are bounded. The error signal, $e(t)$ is bounded for all values of time t . To prove asymptotic stability of the tracking error, i.e., $e(t) \rightarrow 0$ and the sliding surface, $s(t) \rightarrow 0$ as time, $t \rightarrow \infty$. Defining $|s| \leq \eta_\Delta$, (Fei and Xin 2015)

Equation (6.44) can be written as

$$\dot{V} \leq |s||\omega| - |s|\eta \leq \eta_\Delta|\omega| - |s|\eta \quad (6.45)$$

Integrating equation (6.45) on both sides, we have

$$\int_0^\tau |s| d\tau \leq \frac{1}{\eta}(|V(0)| + |V(\tau)|) + \frac{\eta_\Delta}{\eta} \int_0^\tau |\omega| d\tau \quad (6.46)$$

The sliding surface is thus, $s \in L_1$. From Equation (6.45) it is known that derivative of the sliding surface, $\dot{s}(t)$ bounded and $s(t)$ is uniformly continuous. From the corollary of Barbalat's lemma (Ho et al. 2009), we have, $s(t) \rightarrow 0$ and $e(t) \rightarrow 0$ as $t \rightarrow \infty$.

6.6 Simulation Analysis

The simulation analysis has been carried out to investigate the performance of proposed controllers. The developed controls are simulated in MATLAB Simulink. The Simulink programs for BSMC and AFSC for MRE ATVA are shown in Figure 6.10 and Figure 6.11.

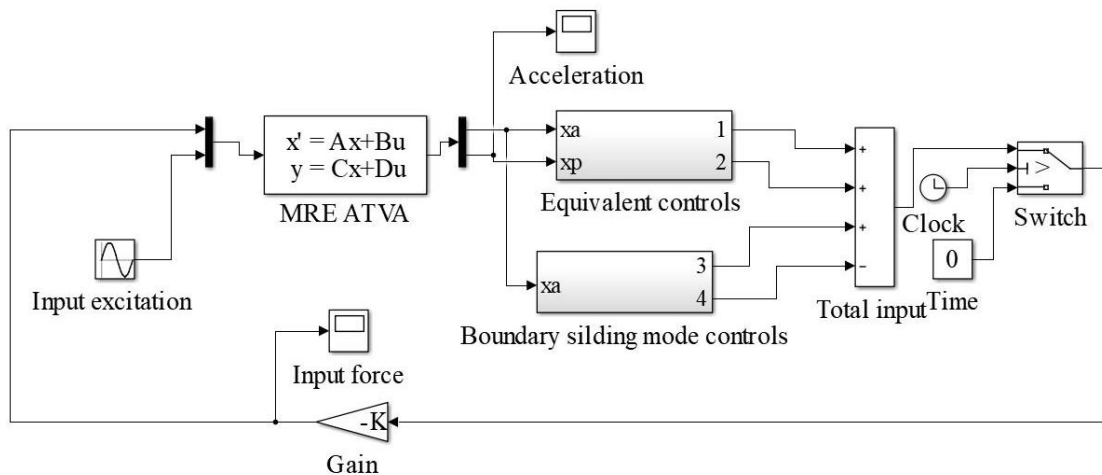


Figure 6.10 Simulink program of BSMC for MRE ATVA.

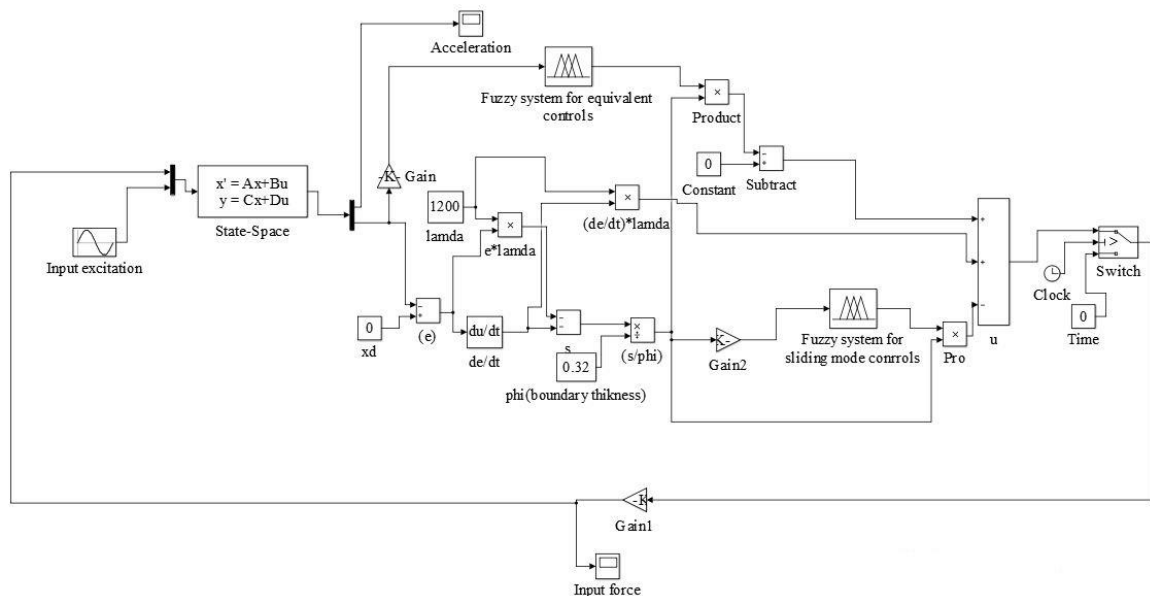


Figure 6.11 Simulink program of AFSC for MRE ATVA.

6.6.1 Position Tracking of MRE ATVA

For the simulation, the parameters considered in the study for the primary system are: mass $m_p = 9.35$ kg, stiffness, $k_p = 922808.011$ N/m, damping coefficient, $c_p = 37.64$ N-s/m, and for MRE ATVA the parameters are: mass, $m_a = 1.57$ kg, stiffness, $k_a = 136916.2$ N/m, damping coefficient, $c_a = 109.41$ N-s/m. Performance of both controls is verified without and with disturbance conditions. The control parameters of BSMC are $\lambda = 1200$, $\Phi=0.3$ and $\eta = 50$ and for the AFSC, the parameters are $\gamma_1 = 1590$ and $\gamma_2 = 1580$. Figure 6.12 depicts the time response of BSMC without and with disturbance. The control tracks the desired signal precisely, as shown in Figure 6.12 (a) without disturbance. However, as the disturbance is introduced in the system, the performance of the BSMC deteriorates, which is observed from the time response as shown in Figure 6.12 (b), with a noticeable difference between the desired signal and the actual response of the system. Figure 6.13 (a) and (b) shows the response of control force and tracking error of MRE ATVA without and with disturbance. As the disturbance is induced in the system, the input control force decreases, whereas the error between the desired signal and the actual response increases.

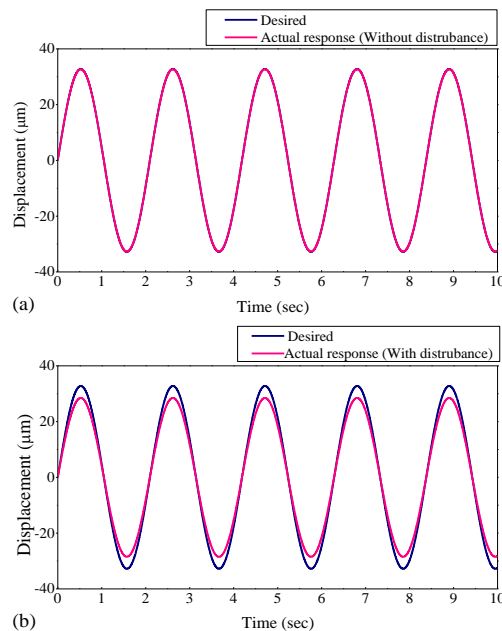


Figure 6.12 Time response of boundary sliding mode control: (a) position tracking without disturbance and (b) position tracking with disturbance.

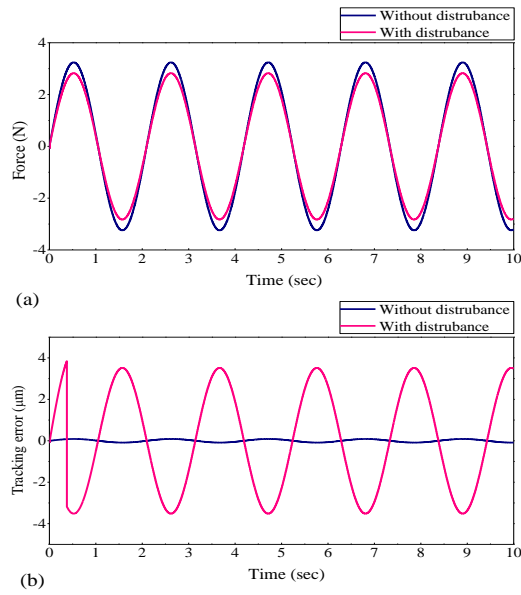


Figure 6.13 Time response of boundary sliding mode control: (a) force and (b) tracking error.

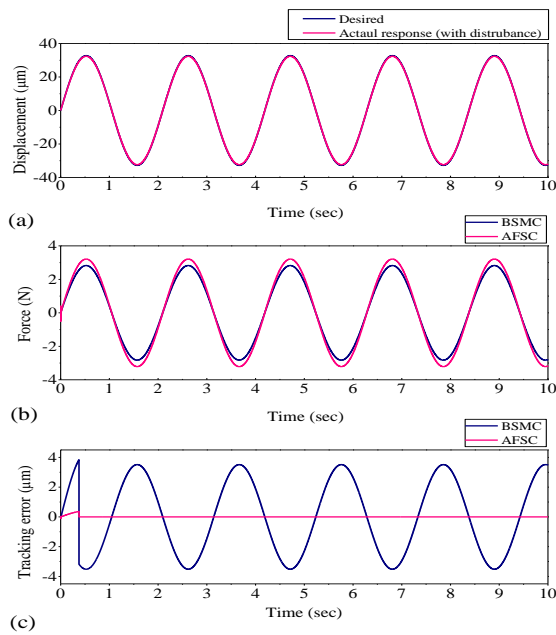


Figure 6.14 Time response of (a) position tracking of adaptive fuzzy sliding mode control with disturbance, (b) force with disturbance and (c) tracking error with disturbance.

Figure 6.14 (a) depicts the performance of AFSC with the external disturbance induced in MREATVA. The actual signal tracks the desired signal with minimal error. This highlights the adaptive nature of the AFSC. Figure 6.14 (a) and (b) show the response of control force and tracking error of BSMC and AFSC of MRE ATVA with disturbance.

6.6.2 Simulation of Single Frequency Excitation

The simulation on both BSMC and AFSC for MRE ATVA with primary mass has been carried out for single frequency excitation from 50 Hz to 56 Hz in steps of 2 Hz, as shown in Figure 6.15 to Figure 6.18. Figure 6.15 depicts the simulated time response of MRE ATVA for frequency excitation at 50 Hz. The time response of primary mass for the controls is as shown in Figure 6.15 (a). For the first 5 s, the system is excited at a constant frequency of 50 Hz, keeping both the controls in OFF condition. Under this condition, the acceleration of the primary mass computed is 5.67 m/s^2 . For the following 5 s, the combined system is excited with the controls in ON condition and the computed accelerations of primary mass for BSMC and AFSC controls are 5.33 m/s^2 and 4.98 m/s^2 , respectively. The percentage reduction of amplitudes of acceleration for BSMC and AFSC compared to control in OFF condition is 5.99 and 12.16, respectively. Figure (b) shows the input control force of MRE ATVA. The amplitudes of BSMC and AFSC were computed as 2.01 N and 2.10 N, respectively. In the ON condition of the control, the control input response is divided into two parts, the transient response and steady-state response. However, the transient response for both controls is less than 0.5 whereas, the steady-state error for both the controls differs significantly with disturbances in MRE ATVA. This confirms that the AFSC is more effective in reducing the amplitude of primary mass acceleration than BSMC. Similar behavior is observed as presented in Figure 6.15 to Figure 6.18 in all the remaining excitation frequencies considered in the present study, summarized in Table 6.2. It is also observed that the percentage reduction of acceleration amplitude of the primary mass is higher at 50 Hz and 56 Hz and lower at 52 Hz and 54 Hz.

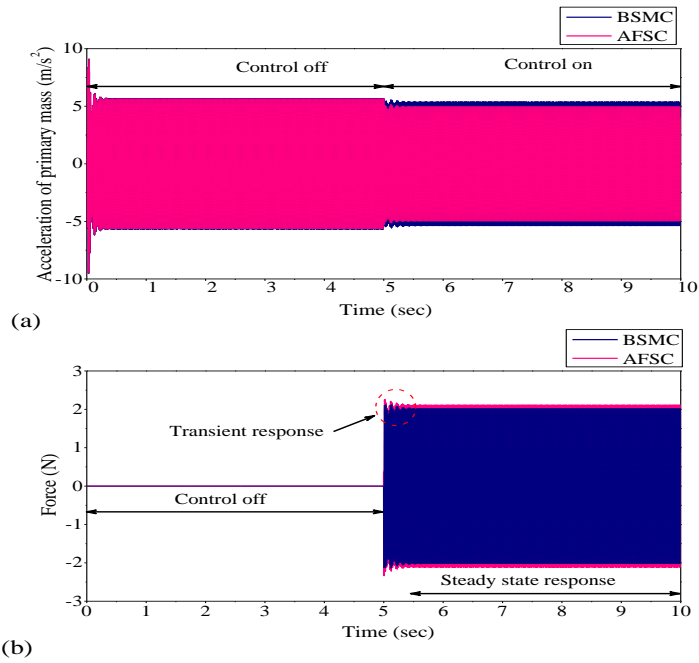


Figure 6.15 Simulated responses at 50 Hz: (a) acceleration of primary mass and (b) force.

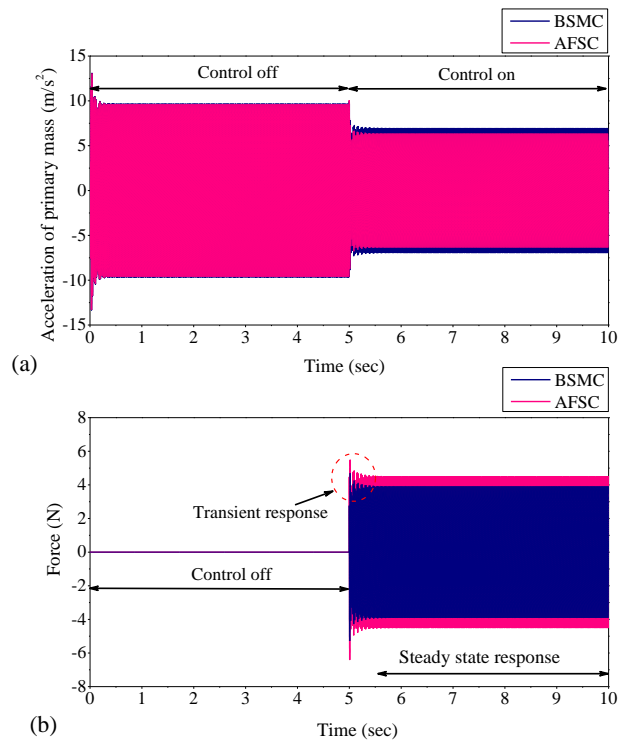


Figure 6.16 Simulated responses at 52 Hz: (a) acceleration of primary mass and (b) force.

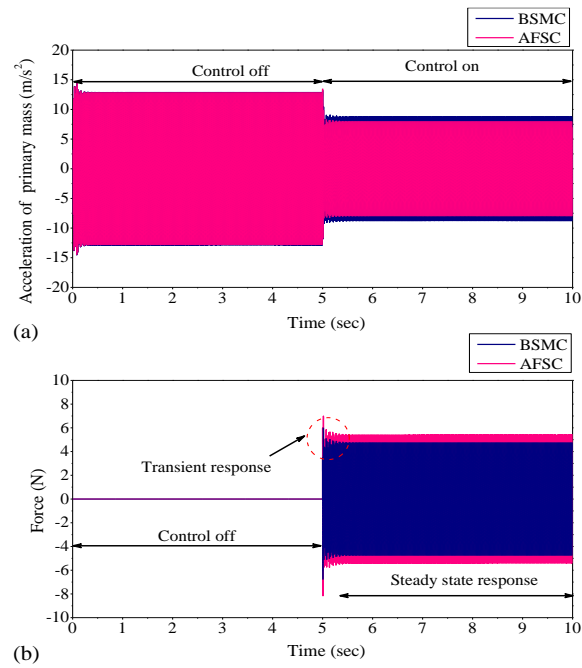


Figure 6.17 Simulated responses at 54 Hz: (a) acceleration of primary mass and (b) force.

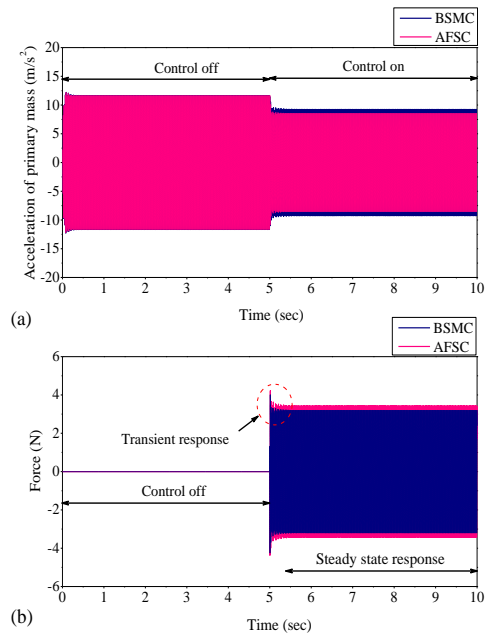


Figure 6.18 Simulated responses at 56 Hz: (a) acceleration of primary mass and (b) force.

Table 6.2 Simulation results of the acceleration of primary mass under different frequencies and controls.

Frequency (Hz)	Without control	With controls								
	\ddot{x}_p (m/s ²)	BSMC				AFSC				
		η	\ddot{x}_p (m/s ²)	% of decrease	Force (N)	γ_1	γ_2	\ddot{x}_p (m/s ²)	% of decrease	Force (N)
50	5.67	38	5.33	5.99	2.01	45	55	4.98	12.16	2.10
52	9.61	153	6.89	28.3	3.88	53	170	6.33	34.13	4.46
54	12.84	152	8.70	32.24	4.74	56	175	7.97	37.92	5.38
56	11.49	35	9.18	14.62	3.02	52	60	8.58	25.53	3.41

η -Gain of the sliding mode control, γ_1 -Adaptive gain of fuzzy equivalent control and γ_2 -Adaptive gain of fuzzy switching control.

6.6.3 Simulation of Variable Frequency Excitation

It is observed from Equation (6.23) that the BSMC works only for a single frequency excitation. With the instantaneous change in the excitation frequency, the developed control needs to tune to the natural frequency of MRE ATVA. This incapability of the conventional BSMC is resolved by incorporating the fuzzy systems into the existing control, forming the adaptive fuzzy sliding mode control as referred to in Equation (6.29). Figure 6.19 depicts the simulated time response of AFSC. Figure 6.19 (a) shows the acceleration response of the primary mass with variable frequency excitation. The combined system is excited from 50 Hz to 56 Hz with an increment of 2 Hz. Each of the frequencies is excited for 4 s with a time period of control ON condition for 2 s and remaining 2 s for OFF condition. Figure 6.19 (b) depicts the tracking of the natural frequencies of the ATVA with the excitation frequencies. The tuning of the ATVA frequencies with the variable frequency excitation occurs with a minimum transient response of less than 0.5 s. As the excitation frequency increases, both the overshoot and the time of transient response decreases significantly. The simulated transmissibility of the primary mass under variable frequency excitation, with and without control, is summarized in Table 6.3.

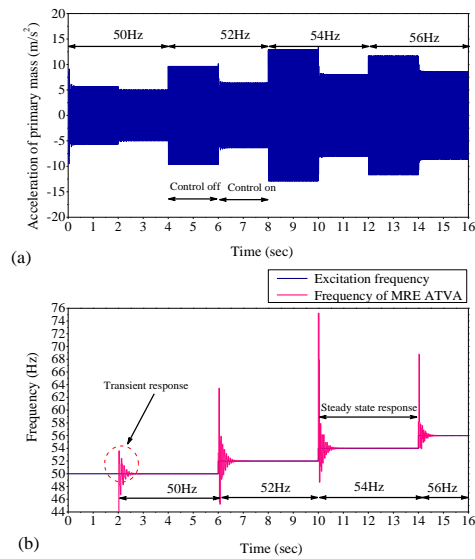


Figure 6.19 Simulated responses at variable frequency excitation: (a) acceleration of primary mass and (b) force.

Table 6.3 Simulation results of transmissibility of primary mass under variable frequency excitation with AFSC.

Frequency (Hz)	Without control	With control	
	Transmissibility	AFSC Transmissibility	% of decrease
50	11.26	9.75	13.41
52	19.08	12.37	35.16
54	25.49	16.18	36.49
56	22.82	17.29	24.23

6.7 Experimental Analysis

The experimental setup of a real-time controller for the combined system is as shown in Figure 6.20. The developed BSMC and AFSC are implemented on Compact RIO Real-time controller (Make National Instruments; Type cRIO-9022). The input module (NI-9234) and output module (NI-9264) are mounted on a real-time controller. The

acceleration signals are acquired using an input module which is further processed using LabVIEW (Version-2017) on a real-time platform. The voltage output module is used to control the magnetic field induced in the electromagnet via a DC power supply (AMETEK, XG150-5.6, Programmable power supply). Figure 6.20 and Figure 6.21 illustrate the schematic and photograph of the real-time controller setup.

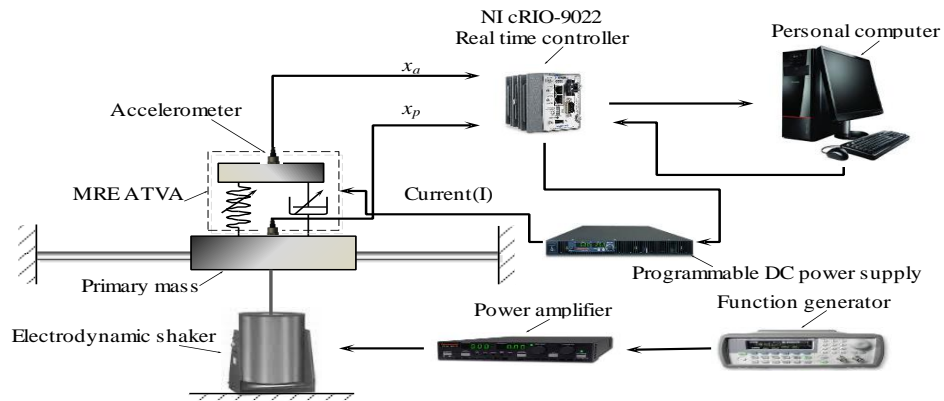


Figure 6.20 Schematic of setup of Real-time controller.

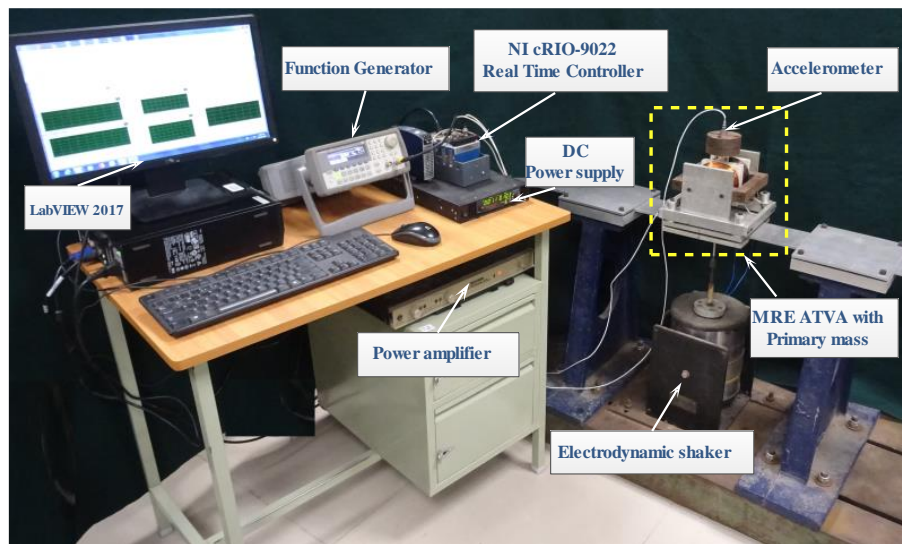


Figure 6.21 Photograph of the experimental setup of Real-time controller.

6.7.1 Experiment of Single Frequency Excitation

The LabVIEW Program BSMC and AFSC for MRE ATVA are shown in Figure 6.22 and Figure 6.23. The experimental response of primary mass for all the frequencies is shown in Figure 6.24 and Figure 6.26. Figure 6.24 (a) presents the measured

acceleration of the primary mass at a frequency of 54 Hz. The system's excitation is carried out for 4 s, and the acceleration of the primary mass is recorded. In the absence of control, the measured amplitude of acceleration is 12.77 m/s^2 . With the implementation of the developed controls, the acceleration amplitudes of the primary mass for BSMC and AFSC reduces to 8.70 m/s^2 and 8.76 m/s^2 , respectively, with an overall percentage reduction of 31.81 % and 34.57 %. Figure 6.24(b) shows the control voltage of the electromagnet. The plot shows a measured input control voltage of 13.58 V and 16.29 V for the BSMC and AFSC, respectively. Transient response for both the controls is observed as 0.5 s after it attains the steady-state response. The results obtained by simulation for both controls follow a similar trend as that of the experimental results and demonstrate that the AFSC is more efficient in reducing acceleration amplitude of primary mass. Similar performance is observed for all frequencies considered in the present investigation as presented in Table 6.4.

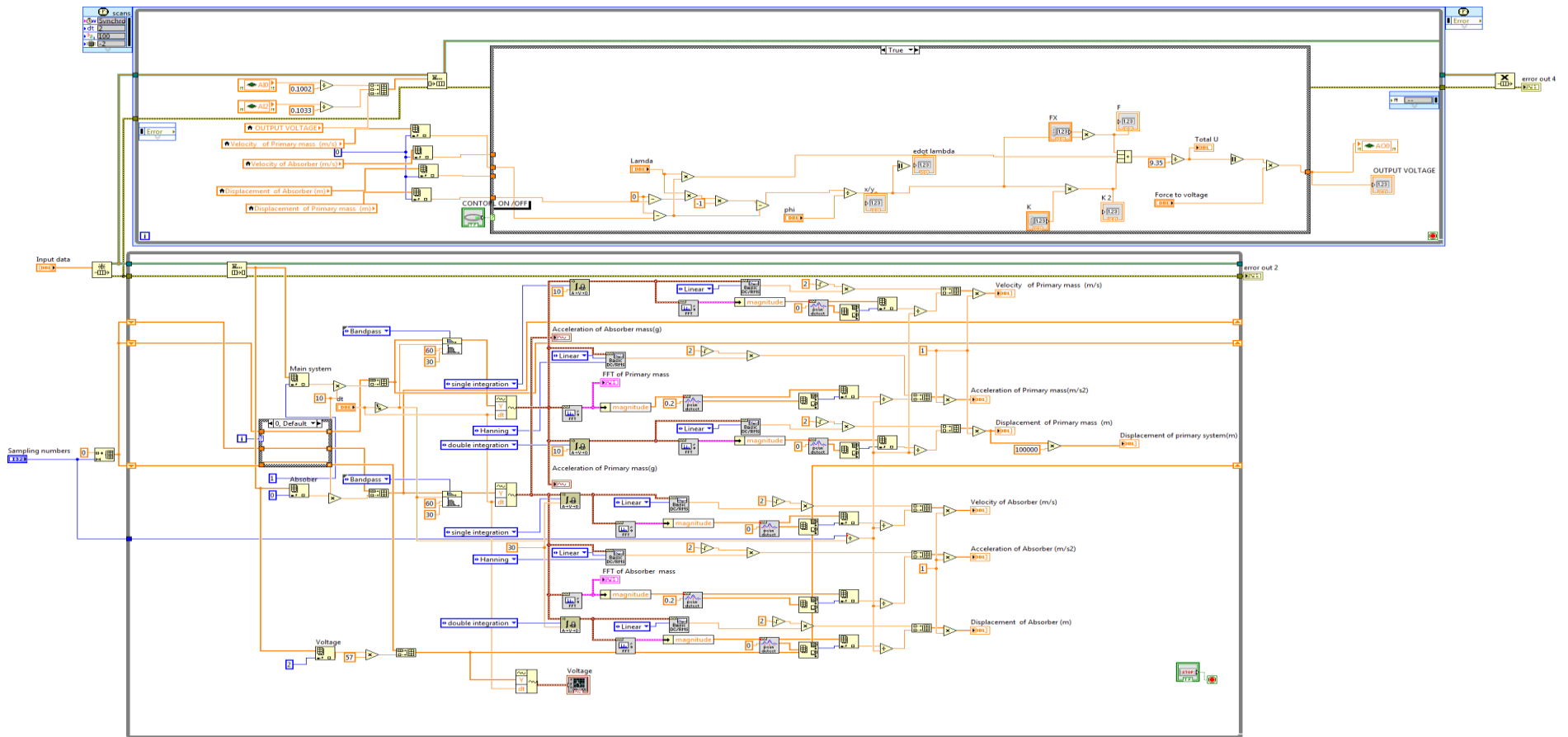


Figure 6.22 LabVIEW program of BSMC for MRE ATVA.

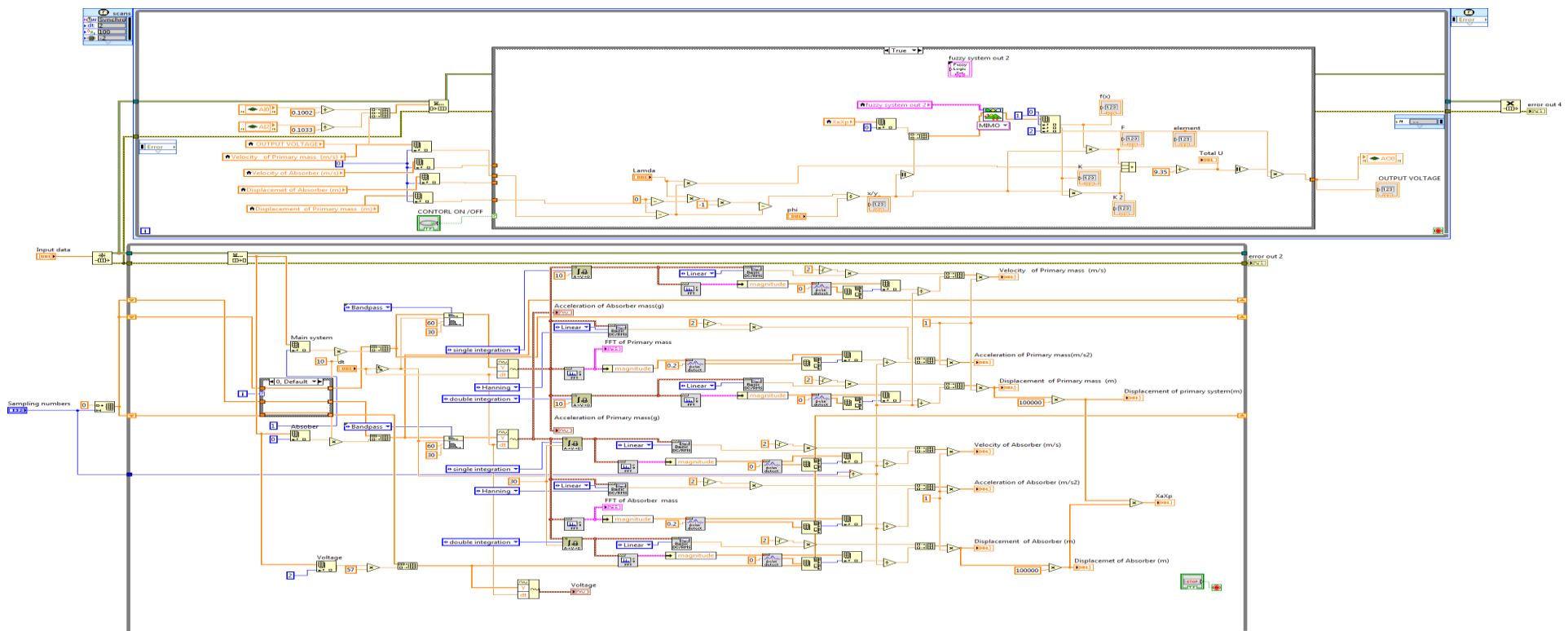


Figure 6.23 LabVIEW program of AFSMC for MRE ATVA.

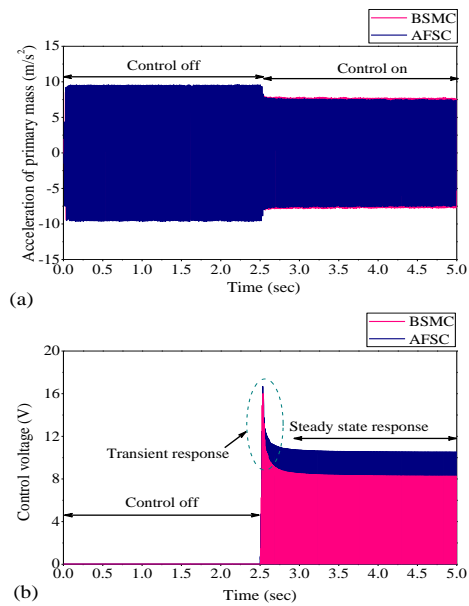


Figure 6.24 Measured responses at 52 Hz: (a) acceleration of primary mass and (b) control voltage.

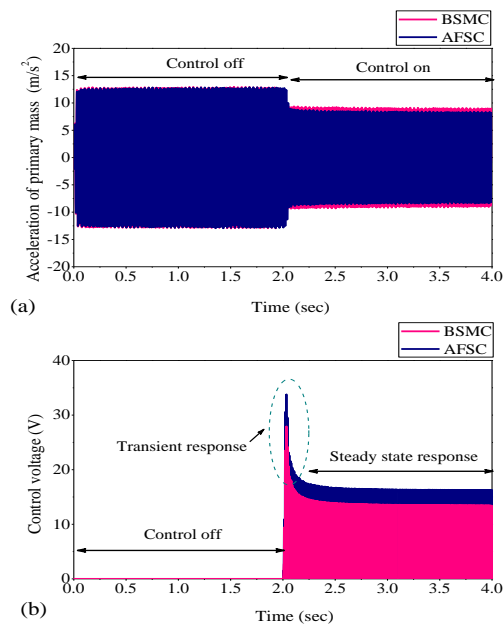


Figure 6.25 Measured responses at 54 Hz: (a) acceleration of primary mass and (b) control voltage.

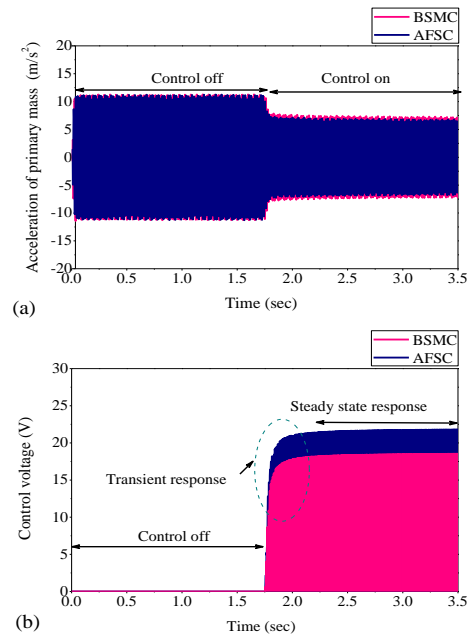


Figure 6.26 Measured responses at 56 Hz frequency: (a) acceleration of primary mass and (b) control voltage.

Table 6.4 The experimental result of the acceleration of primary mass under different frequencies and controls.

Without control		With controls								
Frequency (Hz)	\ddot{x}_p (m/s ²)	BSMC				AFSC				
		η	\ddot{x}_p (m/s ²)	% of decrease	Control voltage (V)	γ_1	γ_2	\ddot{x}_p (m/s ²)	% of decrease	Control voltage (V)
52	9.35	150	7.53	19.40	8.43	55	170	7.35	21.31	10.5
54	12.77	156	8.70	31.81	13.58	52	179	8.36	34.51	16.29
56	11.22	40	7.09	36.82	18.48	56	65	6.73	40.04	21.70

η -Gain of the sliding mode control, γ_1 -Adaptive gain of fuzzy equivalent control and γ_2 -Adaptive gain of fuzzy switching control

6.7.2 Experiment of Variable Frequency Excitation

Figure 6.27 (a) presents the acceleration of primary mass for a variable frequency excitation from 52 Hz to 56 Hz with an increment of 2 Hz. For the excitation period of 5 s with an excitation frequency of 52 Hz, the natural frequency of ATVA under the OFF condition of the control is set for 47 Hz. With the control ON condition, the natural frequency shifts to 52 Hz. Similarly, the combined system is excited for 54 Hz and 56 Hz frequencies with excitation time 4 and 2 s, respectively. The control is ON condition at excitation time of 7.2 and 10.2 s. This influences the shift of the natural frequencies of the MRE ATVA to 54 Hz and 56 Hz. This confirms the effectiveness of AFSC to track the natural frequencies of MRE ATVA with excitation frequencies.

Table 6.5. Experimental results of transmissibility of primary mass under variable frequency excitation with AFSC.

Frequency (Hz)	Without control		With control	
	Transmissibility	AFSC		
		Transmissibility	% of decrease	
52	18.56	14.98	19.25	
54	25.21	17.03	32.43	
56	24.23	14.99	38.14	

Figure 6.27 (b) depicts the control voltage to all excitation frequencies considered here. The natural frequencies of the MRE ATVA depend on the input control voltage of the electromagnet. Figure 6.27 (c) shows the FFT of all excitation frequencies with adaptive fuzzy sliding mode control in OFF and ON conditions. The measured transmissibility of the primary mass under variable frequency excitation, with and without control, is summarized in Table 6.5.

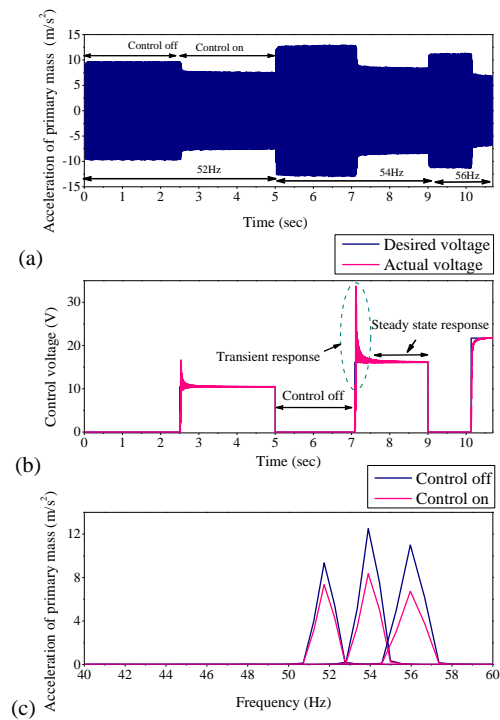


Figure 6.27 Measured responses under variable frequency excitation: (a) acceleration of primary mass, (b) control voltage and (c) FFT.

6.8 Closure

In this chapter, the performance of model-free adaptive fuzzy sliding mode control for the MRE ATVA has been reported. Experiment trials were carried out to extract the dynamic properties of MRE ATVA. The natural frequency of MRE ATVA shifts from 47 Hz to 56 Hz under the magnetic field, 0.315 T. Sliding mode, and model-free adaptive fuzzy sliding mode controls have been developed. The Lyapunov theorem evaluates the asymptotical stability of the developed adaptive control based on fuzzy systems. The performance was compared for both the controls subjected to single frequency excitation. Further, the adaptive fuzzy sliding mode control was investigated for variable frequency excitation. The maximum reduction of transmissibility of primary mass was 38.14%. The model-free adaptive fuzzy sliding mode control is more effective in tuning the natural frequency of MRE ATVA in less than 0.5 s with parameter uncertainties and under variable frequency excitation compared to the boundary layer sliding mode control.

7. Summary, Conclusions and Scopes of Future Work

7.1 Summary

MRE is widely used for the development of semi-active vibration control systems. However, the real-time implementation of the MRE vibration control devices needs controllers to vary the current input to the electromagnet. The present study concentrates on designing and analyzing linear, nonlinear, and intelligent adaptive controllers on MRE-based vibration control systems.

- The MRE changes its dynamic properties under the influence of the magnetic field. To investigate this, the dynamic characterization of MRE is performed for variable current, displacement and frequency. Further, for accurate estimation of the MRE behavior, the Bouc-Wen model is employed. Finally, the characterized MRE is used for the development of the MRE vibration isolator and MRE ATVA.
- The designed MRE vibration isolator is analyzed for its frequency shift under the influence of the field. The simulation of the Bouc-Wen model-based PID and LQR controllers is performed for the MRE vibration isolation for the single frequency excitation. Both the PID and LQR controllers are linear and effective only if the system is linear time-invariant. However, MRE is a viscoelastic material that exhibits nonlinear behavior at higher displacement and uncertain behaviors over a period of time. To resolve this issue, nonlinear and intelligent adaptive controls are developed.
- The boundary sliding mode control (BSMC) and neural network-fuzzy system-based adaptive sliding mode controls (NNAONFSMC) are developed for the MRE vibration isolation having time-varying properties. The Lyapunov theory has been employed to assess the asymptotical stability of the proposed observer and controllers. The simulation and experiment of each control are performed for the single as well as variable frequency excitation.
- Further, the MRE ATVA is developed and analyzed for shift frequency. The boundary sliding mode control (BSMC) and fuzzy system-based adaptive

sliding mode controls (AFSC) are designed for the MRE ATVA. The Lyapunov theorem evaluates the asymptotical stability of the developed adaptive control based on fuzzy systems. The simulation and experiment of each control are conducted for the single and variable frequency excitation.

7.2 Conclusions

The conclusions of the work carried are listed below

- The stiffness and damping of MRE depend on operating frequency, displacement and magnetic field. The dynamic stiffness of the MRE increases, and there is not much variation is observed in damping as current increases. Also, damping and stiffness of the MRE increase and decrease respectively with the input displacement. Furthermore, the operating frequency has little influence on the dynamic properties of MRE. The Bouc-Wen model accurately predicts the behavior of MRE and is used for the simulation of the MRE vibration isolator with a model-based controller.
- The natural frequency of the MRE vibration isolator shifts from 39 Hz to 43 Hz with a current of 2.5A. The simulation and experiment of the PID and LQR controller are performed for the MRE vibration isolation. For the PID controller, the maximum reduction of measured acceleration is 30.27% at a control current of 1.91 A, with an excitation frequency of 38 Hz. Similarly, for the LQR controller, the maximum reduction of the measured acceleration is 35.94 % at a control current of 1.89 A. From the results, it is evident that both the controllers are effective in the mitigation of vibration.
- Further, the effect of BSMC and NNAONFSMC controls is compared without and with parameter uncertainties of MRE vibration isolation at the single excitation frequency. The maximum percentage reduction of the measured acceleration BSMC is 30.53% and for NNAONFSMC is 37.69%. From these outcomes, it is evident that the NNAONFSMC is more effective with time-varying parameter uncertainties of MRE vibration isolation than the BSMC.

- Furthermore, the natural frequency of MRE ATVA shifts from 47 Hz to 56 Hz under the magnetic field, 0.315 T. The performance was compared for both the BSMC and AFSC controls subjected to single frequency excitation. Further, AFSC was investigated for variable frequency excitation. The maximum reduction of transmissibility of primary mass was 38.14%. Thus, the AFSC is more effective in tuning the natural frequency of MRE ATVA in less than 0.5 s with parameter uncertainties and under variable frequency excitation compared to the BSMC.

7.3 Scopes of Future Work

Linear, nonlinear and intelligent adaptive control strategies on the MRE vibration isolation and MRE adaptive tuned vibration absorber have been studied in the present work. Due to the time-varying properties of MRE, intelligent nonlinear adaptive controls were found to be more suitable for the MRE-based smart system. Based on the outcomes, the scope for future works is presented below

- Due to its time-varying properties, the properties of MRE are affected by the surrounding environment and temperature particularly due to electromagnet. This behavior needs to be investigated extensively.
- The MRE-based vibration smart systems need to be implemented on real-time application under translation and torsional loading conditions.
- The vibration and acoustic performance of plates and shells embedded with MRE need to be investigated for high-frequency spectrum.
- The investigation of the MRE can be carried out for impact and high strain rate behavior.

References

- Aggarwal, C. C. (2018). *Neural Networks and Deep Learning*. Springer.
- Behrooz, M., Wang, X., and Gordaninejad, F. (2014a). "Modeling of a new semi-active/passive magnetorheological elastomer isolator." *Smart Mater. Struct.*, 23(4), 045013 (7pp).
- Behrooz, M., Wang, X., and Gordaninejad, F. (2014b). "Performance of a new magnetorheological elastomer isolation system." *Smart Mater. Struct.*, 23(4), 045014 (8pp).
- Blom, P., and Kari, L. (2005). "Amplitude and frequency dependence of magneto-sensitive rubber in a wide frequency range." *Polym. Test.*, 24(5), 656–662.
- Boczkowska, A., Awietjan, S. F., Pietrzko, S., and Kurzydłowski, K. J. (2012). "Mechanical properties of magnetorheological elastomers under shear deformation." *Compos. Part B Eng.*, 43(2), 636–640.
- Böse, H., Rabindranath, R., and Ehrlich, J. (2012). "Soft magnetorheological elastomers as new actuators for valves." *J. Intell. Mater. Syst. Struct.*, 23(9), 989–994.
- Chen, L., Gong, X. L., Jiang, W. Q., Yao, J. J., Deng, H. X., and Li, W. H. (2007). "Investigation on magnetorheological elastomers based on natural rubber." *J. Mater. Sci.*
- Chen, L., Gong, X. L., and Li, W. H. (2008). "Damping of magnetorheological elastomers." *Chinese J. Chem. Phys.*, 21(6).
- Choi, S. B., Li, W., Yu, M., Du, H., Fu, J., and Do, P. X. (2016). "State of the art of control schemes for smart systems featuring magneto-rheological materials." *Smart Mater. Struct.*, 25(4), 043001(24pp).
- Deng, H. X., and Gong, X. L. (2007). "Adaptive tuned vibration absorber based on magnetorheological elastomer." *J. Intell. Mater. Syst. Struct.*, 18(12), 1205–1210.
- Deng, H. xia, and Gong, X. long. (2008). "Application of magnetorheological elastomer to vibration absorber." *Commun. Nonlinear Sci. Numer. Simul.*, 13(9), 1938–1947.

- Dong, X. M., Yu, M., Liao, C. R., and Chen, W. M. (2009). "A new variable stiffness absorber based on magneto-rheological elastomer." *Trans. Nonferrous Met. Soc. China (English Ed.)*, 19(3), 611–615.
- Du, H., Li, W., and Zhang, N. (2011). "Semi-active variable stiffness vibration control of vehicle seat suspension using an {MR} elastomer isolator." *Smart Mater. Struct.*, 20(10), 105003.
- Dyke, S. J. (1996). "Acceleration Feedback Control Strategies for Active and Semi-active Control Systems: Modeling, Algorithm Development, and Experimental Verification." *Univ. Notre Dame*, (July), 255.
- Eem, S. H., Jung, H. J., and Koo, J. H. (2013). "Seismic performance evaluation of an MR elastomer-based smart base isolation system using real-time hybrid simulation." *Smart Mater. Struct.*, 22(5), 055003 (10pp).
- Fei, J., and Xin, M. (2015). "Adaptive fuzzy sliding mode control of MEMS gyroscope sensor using fuzzy switching approach." *J. Dyn. Syst. Meas. Control*, 137(May 2015), 1479–1484.
- Feng, J., Gao, Q., Guan, W., and Huang, X. (2017). "Fuzzy sliding mode control for erection mechanism with unmodelled dynamics." *Automatika*, 58(2), 131–140.
- Fu, J., Li, P., Wang, Y., Liao, G., and Yu, M. (2016). "Model-free fuzzy control of a magnetorheological elastomer vibration isolation system : analysis and experimental evaluation." *Smart Mater. Struct.*, 25(3), 035030 (13pp).
- Fu, J., Yu, M., Dong, X. M., and Zhu, L. X. (2013). "Magnetorheological elastomer and its application on impact buffer." *J. Phys. Conf. Ser.*, 412, 012032 (10pp).
- Graupe, D. (2013). *Principles of Artificial Neural Network. World Sci. Publ.*
- Gu, X., Yu, Y., Li, Y., Li, J., Askari, M., and Samali, B. (2019). "Experimental study of semi-active magnetorheological elastomer base isolation system using optimal neuro fuzzy logic control." *Mech. Syst. Signal Process.*, 119, 380–398.
- Gu, Z. Q., and Oyadiji, S. O. (2008). "Application of MR damper in structural control using ANFIS method." *Comput. Struct.*, 86(3–5), 427–436.

- Hegde, S., Kiran, K., and Gangadharan, K. V. (2015). “A novel approach to investigate effect of magnetic field on dynamic properties of natural rubber based isotropic thick magnetorheological elastomers in shear mode.” *J. Cent. South Univ.*, 22(7), 2612–2619.
- Hegde, S., Poojary, U. R., and Gangadharan, K. V. (2014). “Experimental Investigation of Effect of Ingredient Particle Size on Dynamic Damping of RTV Silicone Base Magnetorheological Elastomers.” *Procedia Mater. Sci.*, 5((2014)), 2301–2309.
- Ho, H. F., Wong, Y. K., and Rad, A. B. (2009). “Adaptive fuzzy sliding mode control with chattering elimination for nonlinear SISO systems.” *Simul. Model. Pract. Theory*, 17(7), 1199–1210.
- J.Inman, D. (2011). *Engineering Vibrations*. Pearson.
- Jin, T., Liu, Z., Sun, S., Ren, Z., Deng, L., Yang, B., Christie, M. D., and Li, W. (2020). “Development and evaluation of a versatile semi-active suspension system for high-speed railway vehicles.” *Mech. Syst. Signal Process.*, 135, 106338.
- Johnson, N., Wang, X., and Gordaninejad, F. (2012). “Dynamic behavior of thick magnetorheological elastomers.” *Act. Passiv. Smart Struct. Integr. Syst. 2012*.
- Jung, H. J., Eem, S. H., Jang, D. D., and Koo, J. H. (2011). “Seismic performance analysis of a smart base-isolation system considering dynamics of MR elastomers.” *J. Intell. Mater. Syst. Struct.*, 22(13), 1439–1450.
- Jung, H. J., Lee, S. J., Jang, D. D., Kim, I. H., Koo, J. H., and Khan, F. (2009). “Dynamic characterization of magneto-rheological elastomers in shear mode.” *IEEE Trans. Magn.*, 45(10), 3930-3933.
- Kaleta, J., Królewicz, M., and Lewandowski, D. (2011). “Magnetomechanical properties of anisotropic and isotropic magnetorheological composites with thermoplastic elastomer matrices.” *Smart Mater. Struct.*, 20(8), 085006 (12pp).
- Khan, I. U., Wagg, D., and Sims, N. D. (2016). “Improving the vibration suppression capabilities of a magneto-rheological damper using hybrid active and semi-active control.” *Smart Mater. Struct.*, 25(8), 1–15.

- Kim, J. S., Yoon, J. H., Jeong, U. C., and Oh, J. E. (2015). “Experimental evaluation of a variable shear modulus characteristic for magnetorheological elastomer due to induced current.” *J. Test. Eval.*, 43(3), 20130282.
- Kim, Y. K., Koo, J. H., Kim, K. S., and Kim, S. (2011). “Developing a real time controlled adaptive MRE-based tunable vibration absorber system for a linear cryogenic cooler.” *IEEE/ASME Int. Conf. Adv. Intell. Mechatronics, AIM*, 287–290.
- Komatsuzaki, T., Inoue, T., and Terashima, O. (2016). “Broadband vibration control of a structure by using a magnetorheological elastomer-based tuned dynamic absorber.” *Mechatronics*, 40, 128–136.
- Kumbhar, S. B., Chavan, S. P., and Gawade, S. S. (2018). “Adaptive tuned vibration absorber based on magnetorheological elastomer-shape memory alloy composite.” *Mech. Syst. Signal Process.*, 100, 208–223.
- Lerner, A. A., and Cunefare, K. A. (2008). “Performance of MRE-based vibration absorbers.” *J. Intell. Mater. Syst. Struct.*, 19(5), 551–563.
- Li, R., and Sun, L. Z. (2013). “Viscoelastic responses of silicone-rubber-based magnetorheological elastomers under compressive and shear loadings.” *J. Eng. Mater. Technol. Trans. ASME*, 135(2), 021008 (7).
- Li, W., Zhang, X., and Du, H. (2012). “Development and simulation evaluation of a magnetorheological elastomer isolator for seat vibration control.” *J. Intell. Mater. Syst. Struct.*, 23(9), 1041–1048.
- Li, Y., and Li, J. (2015). “Finite element design and analysis of adaptive base isolator utilizing laminated multiple magnetorheological elastomer layers.” *J. Intell. Mater. Syst. Struct.*, 26 (14), 1861-1870.
- Li, Y., Li, J., Li, W., and Du, H. (2014a). “A state-of-the-art review on magnetorheological elastomer devices.” *Smart Mater. Struct.*
- Li, Y., Li, J., Li, W., and Du, H. (2014b). “A state-of-the-art review on magnetorheological elastomer devices.” *Smart Mater. Struct.*, 23(12), 123001 (24pp).
- Liao, G., Gong, X., and Xuan, S. (2014). “Phase based stiffness tuning algorithm for a magnetorheological elastomer dynamic vibration absorber.” *Smart Mater. Struct.*,

23(1), 015016(10pp).

Liao, G., Gong, X., Xuan, S., Guo, C., and Zong, L. (2012a). “Magnetic-field-induced normal force of magnetorheological elastomer under compression status.” *Ind. Eng. Chem. Res.*, 51(8), 3322–3328.

Liao, G. J., Gong, X. L., Kang, C. J., and Xuan, S. H. (2011). “The design of an active-adaptive tuned vibration absorber based on magnetorheological elastomer and its vibration attenuation performance.” *Smart Mater. Struct.*, 20(7), 075015 (10pp).

Liao, G. J., Gong, X. L., Xuan, S. H., Kang, C. J., and Zong, L. H. (2012b). “Development of a real-time tunable stiffness and damping vibration isolator based on magnetorheological elastomer.” *J. Intell. Mater. Syst. Struct.*, 23(1), 25–33.

Liu, J., and Wang, X. (2011). *Advanced Sliding Mode Control for Mechanical Systems*. Springer.

Lokander, M., and Stenberg, B. (2003). “Improving the magnetorheological effect in isotropic magnetorheological rubber materials.” *Polym. Test.*, 22(6), 677–680.

Lu, X. (2007). *An Investigation of Adaptive Fuzzy Sliding Mode Control for Robotic Manipulators*.

Luiz, G., Gilberto, C. M. D. A., Melo, P. De, and Jr, V. L. (2013). “Fuzzy Control Embedded in Microcontroller and Applied to an Experimental Apparatus Using Magnetorheological Fluid Damper.” 54–69.

Nguyen, X. B., Komatsuzaki, T., Iwata, Y., and Asanuma, H. (2018). “Modeling and semi-active fuzzy control of magnetorheological elastomer-based isolator for seismic response reduction.” *Mech. Syst. Signal Process.*, 101, 449–466.

Ni, Z. C., Gong, X. L., Li, J. F., and Chen, L. (2009). “Study on a dynamic stiffness-tuning absorber with squeeze-strain enhanced magnetorheological elastomer.” *J. Intell. Mater. Syst. Struct.*, 20(10), 1195–1202.

Nise, N. s. (2011). *Control systems Engineering*. John Wiley and Sons, Inc.

Opie, S., and Yim, W. (2011). “Design and control of a real-time variable modulus vibration isolator.” *J. Intell. Mater. Syst. Struct.*, 22(2), 113–125.

- Parameswaran, A. P., Ananthkrishnan, B., and Gangadharan, K. V. (2015). "Design and development of a model free robust controller for active control of dominant flexural modes of vibrations in a smart system." *J. Sound Vib.*, 355, 1–18.
- Poojary, U. R., and Gangadharan, K. V. (2017). "Magnetic field and frequency dependent LVE limit characterization of magnetorheological elastomer." *J. Brazilian Soc. Mech. Sci. Eng.*, 39(4), 1365–1373.
- Poojary, U. R., Hegde, S., and Gangadharan, K. V. (2016). "Dynamic blocked transfer stiffness method of characterizing the magnetic field and frequency dependent dynamic viscoelastic properties of MRE." *Korea Aust. Rheol. J.*, 28(4), 301–313.
- Poojary, U. R., Hegde, S., and Gangadharan, K. V. (2017). "Dynamic deformation–dependent magnetic field–induced force transmissibility characteristics of magnetorheological elastomer." *J. Intell. Mater. Syst. Struct.*, 28(11), 1491–1500.
- Ramírez-Figueroa, P. P.-C. • F. D. (2010). *Intelligent Control Systems with LabVIEW*.
- Shen, Y., Golnaraghi, M. F., and Heppler, G. R. (2004). "Experimental research and modeling of magnetorheological elastomers." *J. Intell. Mater. Syst. Struct.*, 15(1), 27–35.
- Shenoy, K. P., Poojary, U., and Gangadharan, K. V. (2020). "A novel approach to characterize the magnetic field and frequency dependent dynamic properties of magnetorheological elastomer for torsional loading conditions." *J. Magn. Magn. Mater.*, 498(September 2019), 166169.
- Sinko, R., Karnes, M., Koo, J. H., Kim, Y. K., and Kim, K. S. (2013). "Design and test of an adaptive vibration absorber based on magnetorheological elastomers and a hybrid electromagnet." *J. Intell. Mater. Syst. Struct.*, 24(7), 803–812.
- Slotine, J. J. E. (1991). *Applied Nonlinear Dynamics*. Prentice-Hall.
- Sun, S., Deng, H., Yang, J., Li, W., Du, H., Alici, G., and Nakano, M. (2015). "An adaptive tuned vibration absorber based on multilayered MR elastomers." *Smart Mater. Struct.*, 24(4), 45045.
- Sun, T., Pei, H., Pan, Y., Zhou, H., and Zhang, C. (2011). "Neural network-based

sliding mode adaptive control for robot manipulators.” *Neurocomputing*, 74(14–15), 2377–2384.

Suryawanshi, P. V., Shendge, P. D., and Phadke, S. B. (2016). “A boundary layer sliding mode control design for chatter reduction using uncertainty and disturbance estimator.” *Int. J. Dyn. Control*, 4(4), 456–465.

Tai, N. T., and Ahn, K. K. (2011). “Adaptive proportional-integral-derivative tuning sliding mode control for a shape memory alloy actuator.” *Smart Mater. Struct.*, 20(5), 055010 (13pp).

Tao, Y., Rui, X., Yang, F., and Hao, B. (2019). “Development of a MRE isolation system for strapdown inertial measurement unit.” *Mech. Syst. Signal Process.*, 117, 553–568.

Tayyab., M. (2014). “CONDUCTION OF NERVE.” *SimpleBiology*, 1–25.

Vijay, M., and Jena, D. (2016). “Intelligent adaptive observer-based optimal control of overhead transmission line de-icing robot manipulator.” *Adv. Robot.*, 30(17–18), 1215–1227.

Vijay, M., and Jena, D. (2017). “PSO based neuro fuzzy sliding mode control for a robot manipulator.” *J. Electr. Syst. Inf. Technol.*, 4(1), 243–256.

Vijay, M., and Jena, D. (2018). “Backstepping terminal sliding mode control of robot manipulator using radial basis functional neural networks.” *Comput. Electr. Eng.*, 67, 690–707.

Visakh, P. M., Sabu, T., Arup, K. C., and Mathew, A. P. (2013). *Advances in Elastomers I: Blends and Interpenetrating Networks*. Springer.

Wang, J., Rad, A. B., and Chan, P. T. (2001a). “Indirect adaptive fuzzy sliding mode control: Part II: fuzzy switching.” *Fuzzy Sets Syst.*, 122(1), 21–30.

Wang, J., Rad, A. B., and Chan, P. T. (2001b). “Indirect adaptive fuzzy sliding mode control: Part I: fuzzy switching.” *Fuzzy Sets Syst.*, 122(1), 21–30.

Wang, L.-X. (1997). *A COURSE IN 'FUZZY A Course in Fuzzy Systems and Control. Design*.

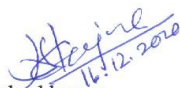
- Wei, S., Wang, Y., and Zuo, Y. (2012). "Wavelet neural networks robust control of farm transmission line deicing robot manipulators." *Comput. Stand. Interfaces*, 34(3), 327–333.
- Xing, Z. W., Yu, M., Fu, J., Wang, Y., and Zhao, L. J. (2015). "A laminated magnetorheological elastomer bearing prototype for seismic mitigation of bridge superstructures." *J. Intell. Mater. Syst. Struct.*, 26(14), 1818–1825.
- Xu, Z., Gong, X., Liao, G., and Chen, X. (2010). "An active-damping-compensated magnetorheological elastomer adaptive tuned vibration absorber." *J. Intell. Mater. Syst. Struct.*, 21(10), 1039–1047.
- Yang, J., Du, H., Li, W., Li, Y., Li, J., Sun, S., and Deng, H. X. (2013). "Experimental study and modeling of a novel magnetorheological elastomer isolator." *Smart Mater. Struct.*, 22(11), 117001O (14pp).
- Yang, J., Gong, X., Deng, H., Qin, L., and Xuan, S. (2012a). "Investigation on the mechanism of damping behavior of magnetorheological elastomers." *Smart Mater. Struct.*, 21(12), 125015 (11pp).
- Yang, J., Gong, X., Deng, H., Qin, L., and Xuan, S. (2012b). "Investigation on the mechanism of damping behavior of magnetorheological elastomers." *Smart Mater. Struct.*, 11.
- Yang, Z., Qin, C., Rao, Z., Ta, N., and Gong, X. (2014). "Design and analyses of axial semi-active dynamic vibration absorbers based on magnetorheological elastomers." *J. Intell. Mater. Syst. Struct.*, 25(17), 2199–2207.
- Ying, Z., Ni, Y., and Sajjadi, M. (2013). "Nonlinear dynamic characteristics of magneto-rheological visco-elastomers." *Sci. China Technol. Sci.*, 56(4), 878–883.
- Yu, Y., Li, Y., and Li, J. (2015). "Nonparametric modeling of magnetorheological elastomer base isolator based on artificial neural network optimized by ant colony algorithm." *J. Intell. Mater. Syst. Struct.*, 26(14), 1789–1798.

List of publications based on PhD Research work


Sl no	Title of paper	Authors (in the same order as in the paper. Underline the research scholar's name)	Journal Name, Year, Volume Number, Issue, Pages)	Month, year of publication	Category*
1	Theoretical and experimental investigation of model-free adaptive fuzzy sliding mode control for MRE based adaptive tuned vibration absorber	<u>G N Susheelkumar</u> , SM Murigendrappa, K V Gangadharan	IOP (Smart Materials and Structures)	March, 2019	1
2	Preparation and Dynamic Characterization of Polymer-based Magnetorheological Elastomer for Vibration Isolator	<u>G N Susheelkumar</u> , SM Murigendrappa, K V Gangadharan	AIP Conference Proceedings International conference on Polymer Composites (ICPC-2018) NIT Karnataka, Surathkal, India	December 15-16,2018	3

Category* 1: Journal paper, full paper reviewed. 2: Journal paper, Abstract reviews. 3: Conference /Symposium paper, full paper reviewed.

4: Conference /Symposium paper, Abstract reviewed. 5: Others (including paper in workshop, NITK Bulletin, short notes etc.).


Sushel Kumar
Research Scholar

Name and Signature, with date


Dr. S M Murigendrappa and Dr. K V Gangadharan,
Research Guide(s)

Name and Signature, with date

CURRICULUM VITAE

1. Name: Susheel kumar
2. Father Name: Naganathrao Gajare
3. Date of Birth: 01-06-1986
4. Permanent Address: House. No-105-33, Bheemnagar,
Basavakalyan, Dist-Bidar,
Karnataka-585327.
5. Mobile Number: 9900806187
6. E-Mail: susheel.ng@gmail.com
7. Educational Qualification:
 - **Diploma** in Mechanical Engineering
Government Polytechnic Bidar, Bidar-585401, Karnataka.
Final year: 60.09%; Graduation Date: June 2005.
 - **Bachelor of Engineering** in Mechanical Engineering
Shirdi Sai Engineering College, Bengaluru-562106, Karnataka.
Aggregate: 64.15%; Graduation Date: November 2008.
 - **Master of Technology** in Machine Design
University of B.D.T College of Engineering, Davangere-
577004, Karnataka.
GPA: 7.53/10.00; Graduation Date: July 2010.
 - **Doctor of Philosophy**
National Institute of Technology Karnataka, Surathkal,
Mangaluru- 575025, Karnataka.
Date: July 2014-July 2021